



POLITECNICO DI MILANO
DEPARTMENT OF PHYSICS
DOCTORAL PROGRAMME IN PHYSICS

TIME-DOMAIN DIFFUSE CORRELATION
SPECTROSCOPY: FROM PHYSICS TO BIOMEDICAL
APPLICATIONS

Doctoral Dissertation of:
Lorenzo Colombo

Supervisor:
Prof. Antonio Pifferi

Tutor:
Prof. Alessandro Torricelli

The Chair of the Doctoral Program:
Prof. Marco Finazzi

Academic year: 2021/2022. PhD Cycle: XXXIV

Index

| | |
|--------------------------------------------------------------------|-----------|
| Index..... | i |
| Acknowledgments..... | v |
| Abstract | vii |
| Sommario | x |
| List of Publications | xii |
| List of Acronyms..... | xiv |
| List of Figures | xvi |
| List of Tables | xxii |
| CHAPTER 1 : DIFFUSE OPTICAL TECHNIQUES AND APPLICATIONS . 1 | |
| 1.1. Light propagation in diffusive media | 2 |
| 1.2. Near infrared spectroscopy | 3 |
| 1.2.1. Time-domain NIRS | 5 |
| 1.3. Dynamic scattering techniques | 8 |
| 1.3.1. Laser speckle | 8 |
| 1.3.2. Laser speckle contrast and Laser Doppler Flowmetry | 9 |
| 1.3.3. Diffuse Correlation Spectroscopy | 10 |
| 1.4. Time resolved dynamic scattering techniques | 11 |
| 1.4.1. Time-domain DCS | 12 |
| 1.5. Comparison with other techniques and applications..... | 15 |
| 1.5.1. DCS validation with blood flow monitoring techniques | 15 |
| 1.5.2. DCS biomedical and clinical applications | 16 |
| CHAPTER 2 : THEORY..... | 19 |

| | | |
|--------------------------------------------------|---------------------------------------------------------------------|-----------|
| 2.1. | The photon diffusion equation | 20 |
| 2.1.1. | Time-resolved diffuse reflectance | 21 |
| 2.2. | Speckle statistics | 22 |
| 2.2.1. | Generalized speckle intensity distribution | 24 |
| 2.3. | Diffuse correlation spectroscopy | 25 |
| 2.3.1. | Single scattering regime (dynamic light scattering) | 25 |
| 2.3.2. | Multiple scattering regime (DCS) | 27 |
| 2.3.3. | Correlation diffusion equation | 29 |
| 2.4. | Time-domain DCS | 31 |
| 2.4.1. | Ideal TD-DCS experiment..... | 31 |
| 2.4.2. | Realistic TD-DCS experiment | 32 |
| CHAPTER 3 : EXPERIMENTAL SETUP | | 39 |
| 3.1. | General scheme..... | 40 |
| 3.2. | Laser sources | 41 |
| 3.2.1. | Ti:Sapphire laser | 43 |
| 3.3. | Single-photon detectors..... | 45 |
| 3.4. | Data acquisition and processing..... | 47 |
| 3.4.1. | Acquisition boards..... | 47 |
| 3.4.2. | Post-processing and fitting..... | 48 |
| 3.5. | Physiological sensors..... | 50 |
| CHAPTER 4 : SYSTEM CHARACTERIZATION | | 53 |
| 4.1. | Characterizing the coherence parameter β | 54 |
| 4.1.1. | Pulse duration effect | 54 |
| 4.1.2. | Optical properties effect | 56 |
| 4.1.3. | Gate width effect..... | 58 |
| 4.2. | Characterizing the BFI accuracy: comparing theoretical models | 59 |
| 4.3. | Laser sources comparison | 62 |
| 4.3.1. | Emission bandwidth and pulse temporal shape (IRF) | 62 |
| 4.3.2. | Coherence parameter (β)..... | 64 |
| 4.4. | Single-photon detectors comparison..... | 66 |
| 4.4.1. | IRF and DTOF curves..... | 66 |
| 4.4.2. | Auto-correlations functions..... | 69 |
| 4.5. | Wavelength comparison | 70 |
| CHAPTER 5 : TEMPORAL SPECKLE EFFECT | | 73 |
| 5.1. | Experimental observations..... | 74 |

| | | |
|-----------------------------------------------------|-------------------------------------------------------------|------------|
| 5.1.1. | Effect of scatterers motion and fiber collection area | 75 |
| 5.2. | Physical interpretation | 77 |
| 5.2.1. | Statistical model | 77 |
| 5.2.2. | Experimental results | 78 |
| 5.3. | Biomedical application | 80 |
| CHAPTER 6 : <i>IN VIVO</i> EXPERIMENTS | | 83 |
| 6.1. | Materials and methods | 84 |
| 6.1.1. | Optical probe and physiological sensors | 84 |
| 6.1.2. | Protocols | 85 |
| 6.1.3. | Data analysis | 87 |
| 6.2. | Cuff occlusion experiments | 88 |
| 6.3. | Brain experiments | 90 |
| 6.3.1. | Resting state: vascular pulsatility | 91 |
| 6.3.2. | Breath hold experiment..... | 94 |
| 6.4. | Experiments beyond the water peak | 96 |
| 6.4.1. | Optical properties at longer wavelengths..... | 96 |
| 6.4.2. | Cuff occlusion experiments..... | 98 |
| Conclusions | | 103 |
| Bibliography..... | | 107 |



Acknowledgments

Foremost, I would like to express my gratitude to my advisor Prof. Antonio Pifferi for his continuous support during my PhD. His patient and insightful guidance helped me in all the time of research, and to successfully overcome any research challenge.

I thank my former colleagues Dr. Sanathana Konugolu, Dr. Pranav Lanka, and all the members of the Biomedical Optics group at Politecnico di Milano.

Also, a great thanks goes to our collaborators at ICFO (Barcelona), in particular Prof. Turgut Durduran, Dr. Marco Pagliuzzi, and Veronika Parfentyeva, which have been an essential support during all our research projects.

I want to thank also prof. Sylvain Gigan, from Laboratoire Kastler-Brossel (Paris), for hosting me for a summer internship in his group. This gave me a new perspective on how to tackle new problems.

Last but not the least, I would like to thank my girlfriend Veronica and my family for their unconditioned support during this years.



Abstract

Diffuse correlation spectroscopy (DCS) is an optical technique which, by measuring the speckle intensity fluctuations of coherent light diffused by a turbid sample, extracts information regarding the scatterers' dynamics. Its main biomedical application is the in vivo non-invasive measurement of fluctuation of red blood cells, and thus micro-vascular blood flow (BF).

Since DCS typically uses a continuous-wave (CW) light source, it generally lacks depth sensitivity. Also, a knowledge of the sample optical properties (scattering and absorption coefficients) is required for a correct BF estimation. Time-domain (TD) DCS tackles these problems by using a pulsed yet coherent light source. This might enable a depth resolved BF measurement, by measuring the speckle fluctuations at different time-of-flights. The aim of this thesis is to lay the foundations of TD-DCS, both on the theoretical and experimental sides.

In the initial part of this work, first I introduce the field of diffuse optics, focusing on near infrared spectroscopy (NIRS) and laser speckle methods. Also, a comparison with other medical techniques is presented. Second, a theoretical model for the interpretation and analysis of the data is developed, by suitably modelling the instrument response function (IRF) and gate width effects. Third, a novel experimental setup is developed and optimized, focusing on the laser source and single-photon detectors.

In the second part of this thesis, I present the experimental results. Initially, a system characterization is performed, by exploiting tissue mimicking phantoms. This helps in defining the figures of merit of the

system, and in optimizing its components (such as laser source and single-photon detectors).

Next, I present an experimental observation of an unexpected effect, a temporal fluctuation in the distribution of time-of-flights curve, which will be termed temporal speckle. I provide a physical interpretation of the phenomena and demonstrate its applicability to the measurement of blood flow.

Finally, I move to *in vivo* experiments on adult volunteers. I focus my attention of muscle (cuff occlusion) and brain (forehead) measurements, observing interesting physiological phenomena (such as vascular pulsatility). Also, I demonstrate the possibility of performing *in vivo* measurements in a novel spectral range, in particular beyond $1 \mu\text{m}$.

Collectively, this work provides a solid theoretical and experimental foundation for the further development of the technique, and its biomedical/clinical application.

Sommario

La spettroscopia di correlazione diffusa (diffuse correlation spectroscopy, DCS) è una tecnica ottica che, misurando le fluttuazioni di intensità dello *speckle* prodotto da luce coerente diffusa da un campione torbido, estrae informazioni sulla dinamica dei centri diffusori. La sua principale applicazione biomedica è la misurazione *in vivo* non invasiva delle fluttuazioni dei globuli rossi, e quindi del flusso sanguigno (blood flow, BF) micro-vascolare.

Poiché la DCS utilizza tipicamente una sorgente di luce in continua (continuous wave, CW), generalmente non ha sensibilità alla profondità. Inoltre, una conoscenza delle proprietà ottiche del campione (coefficienti di scattering e di assorbimento) è necessaria per una stima corretta del BF. La DCS nel dominio del tempo (time domain DCS, TD-DCS) affronta questi problemi utilizzando una sorgente di luce pulsata ma coerente. Questo potrebbe permettere una misura di BF risolta in profondità, misurando le fluttuazioni di *speckle* a diversi tempi di volo. Lo scopo di questa tesi è quello di porre le basi della TD-DCS, sia dal lato teorico che sperimentale.

Nella parte iniziale di questo lavoro, per prima cosa introdurrò il campo dell'ottica diffusa, concentrandomi sulla spettroscopia nel vicino infrarosso (near infrared spectroscopy, NIRS) e sui metodi basati sul laser *speckle*. Inoltre, verrà presentato un confronto con altre tecniche biomediche. In secondo luogo, proporrò un nuovo modello teorico per l'interpretazione e l'analisi dei dati sperimentali, modellando opportunamente l'effetto della funzione di risposta dello strumento (IRF) e gli effetti dell'ampiezza del gate temporale. In terzo luogo, verrà descritto il nuovo sistema sperimentale che è stato sviluppato e ottimizzato, focalizzandomi sulla sorgente laser e sui rivelatori a singolo fotone.

Nella seconda parte di questa tesi, presenterò i risultati sperimentali. Inizialmente, descriverò la caratterizzazione del sistema, eseguita sfruttando “fantocci” che simulano i tessuti. Questo aiuterà a definire le figure di merito del sistema e a ottimizzare i suoi componenti (come la sorgente laser e i rivelatori a singolo fotone). Poi, presenterò un'osservazione sperimentale di un effetto inaspettato, che verrà chiamato *speckle* temporale. Fornirò un'interpretazione statistica del fenomeno e dimostrerò un'applicazione biomedica.

Infine, passerò a descrivere gli esperimenti *in vivo* su volontari adulti. Ho focalizzato la mia attenzione sulle misurazioni muscolari (occlusione vascolare) e cerebrali (fronte), osservando interessanti fenomeni fisiologici (come la pulsatilità vascolare). Inoltre, ho dimostrato la possibilità di eseguire misurazioni *in vivo* in una nuova gamma spettrale, in particolare oltre $1 \mu m$.

Collettivamente, questo lavoro fornisce una solida base teorica e sperimentale per l'ulteriore sviluppo della tecnica, e per la sua applicazione biomedica e clinica.

List of Publications

This thesis work was partially disseminated in the following peer-reviewed articles:

1. L. Colombo, M. Pagliuzzi, S. K.V. Sekar, *et al.*, "Effects of the instrument response function and the gate width in time-domain diffuse correlation spectroscopy: model and validations," *Neurophotonics* **6**(3), 035001 (2019).
2. L. Colombo, M. Pagliuzzi, S. K.V. Sekar, *et al.*, "*In vivo* time-domain diffuse correlation spectroscopy above the water absorption peak," *Optics Letters* **45**, 3377-3380 (2020).
3. L. Colombo, S. Samaei, P. Lanka, *et al.*, "Coherent fluctuations in time-domain diffuse optics," *APL Photonics* **5**(7), 071301 (2020).
4. S. Samaei, L. Colombo, D. Borycki, *et al.*, "Performance assessment of laser sources for time-domain diffuse correlation spectroscopy," *Biomed. Opt. Express* **12**, 5351-5367 (2021).
5. M. Pagliuzzi, L. Colombo, E. E. Vidal-Rosas, *et al.*, "Time resolved speckle contrast optical spectroscopy at quasi-null source-detector separation for non-invasive measurement of microvascular blood flow," *Biomed. Opt. Express* **12**, 1499-1511 (2021).
6. L. Colombo, V. Parfentyeva, P. Lanka, *et al.*, "*In vivo* time-domain diffuse correlation spectroscopy with a superconducting nanowire single photon detector", in preparation.

List of Acronyms

AO: Acousto-optic
ASL-MRI: Arterial-Spin-Labelled Magnetic Resonance Imaging
BF(I): Blood flow (Index)
BR: Breath Rate
BS: Beam Splitter
BVP: Blood volume pulse
CDE: Correlation Diffusion Equation
CTE: Correlation Transfer Equation
CW: Continuous Wave
DCS: Diffuse Correlation spectroscopy
DLS: Dynamic Light Scattering
(D)TOF: (Distribution) of time-of-flights
DWS: Diffusing Wave Spectroscopy
EEG: Electro-Encephalogram
EGF: Effective Gate Function
EKG: Electrocardiogram
FEM: Finite Elements Method
FFT: Fast Fourier Transform
FWHM: Full width at half-maximum
IRF: Instrument Response Function
LDF: Laser Doppler Flowmetry
LSCI/LSCA: laser speckle contrast imaging/analysis
MMF: Multi Mode Fiber
MSD: Mean Square Displacement
NIR(S): Near Infrared (Spectroscopy)
PAD: Periphery artery disease
PD: Photodiode
PDE: Photon Diffusion Equation
PDL: Pulsed Diode Laser
PDT: Photo-Dynamic Therapy
PMT: Photomultiplier
PSD: Power Spectral Density

RBC: Red blood Cells
rBFI: Relative Blood Flow Index
RTE: Radiative Transfer Equation
SD(S): Source-Detector (Separation)
SMF: Single Mode Fiber
SNR: Signal-to-noise ratio
SPAD: Single-photon avalanche diode
SPSND: Single-photon superconducting nanowire detector
TCSPC: Time-correlated single-photon counting
TD: Time Domain
TDU: Transcranial Doppler ultrasound
Ti:Sa: Ti:Sapphire
TR: Time Resolved
VA: Variable Attenuator
Xe-CT: Xenon Computed Tomography

List of Figures

- Figure 1-1: Specific absorption coefficient (absorption per unitary concentration) of the four main tissue chromophores: oxy- and deoxy-haemoglobin (O_2Hb/HHb , respectively), water and lipide. It might be noted that, in the range between 600 nm and 900 nm, light absorption is significantly lower compared to the other wavelengths. That spectral range is conventionally referred as “physiological window”. Figure from Ref. [9]..... 3
- Figure 1-2: Three different approaches to NIRS: 1) Continuous wave, 2) Frequency-domain, 3) Time-domain. Spatial frequency domain (not shown) modulates the light source over the spatial, instead of the temporal, dimension. Adapted from Ref. [1]..... 5
- Figure 1-3: Principle of TD-NIRS. A short (few hundred picoseconds) laser pulse is injected in the sample, and the distribution of time-of-flights (DTOF) of the diffused photons is recorded. The DTOF carries useful information regarding the sample optical properties. 6
- Figure 1-4: Comparison of the sensitivity maps for three different time-of-flights ($t = 0.5$ ns, 1 ns and 1.5 ns: top, middle, and lower plots). Light is injected and collected on the top surface of the medium, in reflectance geometry. The source-detector (SD) separation (ρ) is 0 mm and 30 mm for the left and right plots, respectively. While the penetration depth increases with the time-of-flight, it does not depend significantly on the SD separation. Figure adapted from Ref. [15]..... 7
- Figure 1-5: Image of a laser speckle pattern on a screen. 8
- Figure 1-6: Principle of diffuse correlation spectroscopy (DCS). When photons undergo dynamic scattering events, the diffused light intensity (on a single speckle) fluctuates over time. Faster particles correspond to faster intensity fluctuations. This is typically quantified calculating the intensity autocorrelation function g_2 as a function of delay time τ 10

| | |
|------------------------------------------------------------------------------------------------------------------------------------------------------------------------------------------------------------------------------------------------------------------------------------------------------------------------------------------------------------------------------------------------------------------------------------------------------------------------------------------------------------------------------------------------------------------------|----|
| Figure 2-1: Time-resolved diffuse reflectance for a semi-infinite medium. Dependence on a) the absorption coefficient (in mm^{-1}) and b) the reduced scattering coefficient (in mm^{-1}). Figure adapted from Ref. [8]. | 22 |
| Figure 2-2: Dynamic light scattering (DLS) experiment. A diluted sample is illuminated by a coherent laser and light scattered at a fixed angle θ is collected. The light intensity auto-correlation function is then computed and analysed. | 25 |
| Figure 2-3: Photon trajectories in a typical DCS experiment. Photons are multiply scattered between the source and injection points. When the scatterers move, the photon trajectories undergo slight changes which modify their phases (and thus the resulting intensity). From Ref. [141]. | 27 |
| Figure 2-4: Example of effective gate function (EGF). The black line is the instrument response function (IRF). The shaded blue and red regions denote the (ideal) gate regions (an early and a late gate). The blue and red lines are the corresponding EGF, which measure which path lengths are actually measured, contributing to the measurement. Figure adapted from Ref. [144]. | 35 |
| Figure 3-1: Experimental setup scheme. The scheme was conceptually divided in three parts: “source” (red box), “detection” (blue dash-dotted box), and “data acquisition” (green dashed box). The thick red lines denote free-space optical propagation, the black curved lines denote optical fibers, and the black straight lines denote electrical connection. In the figure BS: beam splitter; PD: photodiode; VA: variable attenuator; MMF: multi-mode fiber; ρ : source-detector separation; SMF: single-mode fiber; PC: computer with software correlator. | 40 |
| Figure 3-2: Scheme of the Ti:Sapphire laser used in this work. Light from a Nd:YAG CW laser is delivered to a Ti:Sapphire crystal, in a Z-shaped optical resonator. A tuneable filter is used for wavelength selection. An acousto-optic (AO) modulator (100 MHz modulating frequency) is used for the active mode-locking. The wavelength range is 700-850 nm for typical mirror set, 900-1050 nm for the IR mirror set. The average power is above 100 mW, while the pulse duration is tuneable between 50 ps and 1 ns. | 43 |
| Figure 3-3: Laser power as a function of wavelength, for the typical mirror set (700-850 nm), CW regime. In the pulsed regime the average power is roughly halved (but it depends strongly on the laser configuration). | 45 |
| Figure 3-4: Integration of the physiological sensors in the experimental setup. The three sensors (electrocardiogram, respiration monitor, peripheral blood volume) were placed on the subject, and the data acquired with their acquisition board. In order to synchronize the optical data with the | |

| | |
|-------------------------------------------------------------------------------------------------------------------------------------------------------------------------------------------------------------------------------------------------------------------------------------------------------------------------------------------------------------------------------------------------------------------------------------------------------------------------------------------------------------------------------------------------------------------------------------------------------------------------------------------------------------------------------------------------|----|
| physiological sensors, an electronic TTL signal was generated by a PC and delivered to the two acquisition boards..... | 51 |
| Figure 4-1: Liquid phantom results for ungated acquisition, for different IRF FWHM. The laser pulse duration was tuned by acting on the acousto-optic modulation power. Panels (a) and (b) show the intensity and electric-field auto-correlations [$g_2(\tau)$ and $g_1\tau$]. At very short lag times τ ($< 10 - 6s$) the spurious effect of the detector after-pulsing is visible, while the behaviour at longer τ is mainly determined by the dynamics of the sample. Panels (c) and (d) show the corresponding coherence parameter and brownian diffusion coefficient [β and DB]. The error-bars denote standard deviations. Figure adapted from Ref. [144]. | 55 |
| Figure 4-2: Dependence of the measured coherence parameter β (y axis) on the absorption coefficient. The experiments were performed for different pulse durations (IRF FWHM, x axis), in ungated acquisition. The samples are liquid phantoms with fixed reduced scattering ($\mu_s' = 10 \text{ cm}^{-1}$), and different absorptions (see legend)..... | 56 |
| Figure 4-3: Dependence of the measured coherence parameter β (y axis) on the reduced scattering coefficient. The experiments were performed for different pulse durations (IRF FWHM, x axis), in ungated acquisition. The samples are liquid phantoms with fixed absorption ($\mu_a = 0.1 \text{ cm}^{-1}$), and different values of reduced scattering (see legend). | 57 |
| Figure 4-4: Measured β parameter as a function of gate duration (250, 500, 1000, 2000, 4000, 7000 ps), always starting at the DTOF peak. The measurements were performed for five different pulse durations (IRF FWHM, see legend). The x axis is in log scale for better readability. | 58 |
| Figure 4-5: (a) IRF and DTOF from the phantom experiment. (b) Measured autocorrelations (g_i) for an early gate (E, blue diamonds) and a late gate (L, red squares). The gates were centred at $t = 0 \text{ ns}$ and $t = 1.5 \text{ ns}$ respectively. Dashed lines denote their best-fits with uncorrected model (UNC), while continuous lines the best-fits with the IRF-corrected model (COR). | 60 |
| Figure 4-6: (a) comparison of the retrieved BFI for the uncorrected (uncorr, blue points) and IRF-corrected (corr, brown points) fits, together with the reference BFI obtained with ungated analysis (CW, dashed line). (b) Measured β parameter (from the amplitude of the autocorrelations), for the 5 considered temporal gates. For both the panels, the error bars report the measured mean and standard deviation across all the repetitions..... | 61 |

| | |
|------------------------------------------------------------------------------------------------------------------------------------------------------------------------------------------------------------------------------------------------------------------------------------------------------------------------------------------------------------------------------------------------------------------------------------------------------------------------------------------------------------------------------------------------------------------------------|----|
| Figure 4-7: (a-c) Measured emission spectra for each laser module, normalized to amplitude. (d) Comparison of the IRF for each laser, normalized to amplitude and with $t = 0$ ns defined as the peak of the IRF. Figure adapted from Ref. [166]. | 63 |
| Figure 4-8: Measured coherence parameter (β) for the three different lasers (columns), and two source-detector separations (SDS, rows). Different colours map different gate widths (see legend). Average and standard deviation were computed along 5 different repetitions, each having a fixed number of photons (5 M). Figure adapted from Ref. [166]. | 65 |
| Figure 4-9: Comparison of the IRF (left columns) and DTOF (right columns) for the SNSPD (top row, in red) and SPAD (bottom rows, in blue) detectors. The time $t = 0$ ps was set to the peak of the IRF. Integration time was 0.1 s, no background subtraction. Note the different shape of the IRF, and dynamic range of the IRF and DTOF. | 67 |
| Figure 4-10: Comparison of the intensity auto-correlation function (ungated), for a parallel measurement with the SNSPD (blue) and SPAD (red) detectors. Note the highly different behaviour at short lag times (i.e., for $\tau < 10 - 6s$). | 69 |
| Figure 4-11: Comparison of the intensity (a) and electric field (b) auto-correlation functions [$g_{2\tau}$ and $g_{1\tau}$], measured at 785 nm (red curves) and 1000 nm (blue curves). The curves are shows for ungated acquisition (U, symbols), early gate (E, continuous lines), and late gate (L, dashed lines). Figure from Ref. [170]. | 71 |
| Figure 5-1: (a) Setup scheme: Ti:Sapphire (Ti:Sa) laser, the SPAD detector, and the TCSPC board. The source-detector separation is $\rho = 1.5$ cm. The bottom part shows, from a Monte Carlo simulation, the distribution of the re-collected photons as a function of their time-of-flight (colour-map in the inset) (b) Experimental results: instrument response function (IRF), measured distribution of times-of-flights (DTOF) from a solid resin phantom, and for comparison the theoretical curve (diffuse reflectance convolved with IRF). Figure from Ref. [133]. | 74 |
| Figure 5-2: DTOF contrast (see Eq. 5-1) as a function of the elapsed time T (x-axis, in seconds) and the time-of-flight t (y-axis, in ns). Top rows (a-c): phantoms with different scatters motions (liquid, silicone, and resin), single mode collection fiber ($5 \mu m$). Bottom rows (d-f): resin phantom, different collection fibers core diameters ($\emptyset = 25, 10, 5 \mu m$). Figure from Ref. [133]. | 76 |
| Figure 5-3: Comparison of the measured βt from the amplitude of the autocorrelations $g_2(t, \tau)$ (blue points with shaded standard deviation), with | |

| | |
|---------------------------------------------------------------------------------------------------------------------------------------------------------------------------------------------------------------------------------------------------------------------------------------------------------------------------------------------------------------------------------------------------------------------------------------------|----|
| the βt retrieved with Eq. (5.2) using the measured intensity fluctuations $\sigma I 2t$ and average intensity $\langle I t \rangle$. The three subplots correspond to three different pulse durations (IRF FWHM): a) 450 ps, b) 225 ps, and c) 175 ps. Figure adapted from Ref. [133]. | 79 |
| Figure 5-4: Arterial occlusion experiment a) DTOF total counts (cps), with 100 ms temporal resolution. The black dashed lines enclose the occlusion period (from minute 2 to 5). b) Reciprocal of the speckle contrast (normalized to the initial baseline) temporal evolution, where the occlusion and hyperaemic peak (after minute 5) are clearly visible. | 81 |
| Figure 6-1: Photo of the custom optical probe, with the source and collection fibers (orange and yellow, respectively). The blue band is used for attaching the probe to the tissue. | 84 |
| Figure 6-2: Schematics of the cuff occlusion experiments, where the positions of the inflatable tourniquet (blue band) and the optical probe (red circle) are highlighted. | 86 |
| Figure 6-3: Results of the cuff occlusion experiments. Each row corresponds to a different subject, while each column to a different laser source (LDH, Ti:Sapphire and VisIR). The occlusion (220 mmHg pressure) was performed from minute 2 to minute 5. The rBFI time trace is shown for an early gate (red), an intermediate gate (blue), and a late gate (red points). Figure from Ref. [166]. | 89 |
| Figure 6-4: a) Measured IRF and DTOF curve on the forehead. The IRF show a gaussian-like shape, while both the curves have >4 decades dynamic range. The vertical lines denote the central time of the considered gates (200 ps width, 100 ps overlap). b) Intensity autocorrelation curves, for 7 different gate positions (see legend). The data suggests that the signal quality is sufficient for gates centred up to $t = 500-600$ ps. | 91 |
| Figure 6-5: Measured rBFI (BFI normalized to average) for ungated acquisition, early and late gate (upper, middle, and lower panels). The sampling rate is 10 Hz in all cases, without smoothing. In all three cases, vascular pulsatility is clearly visible. | 92 |
| Figure 6-6: Comparison of the power spectral density (PSD) of the rBFI (ungated, early gate, and late gate) and the electrocardiograph (ECG) trace. Interestingly, the two spectra show a very similar shape around the 1 Hz region (corresponding to the heart-beat periodicity). The second harmonic (around 2 Hz) is also visible in both the modalities. | 93 |
| Figure 6-7: Breath hold experiment a) rBFI time trace for ungated (purple), early gate (green), and late gate (light blue) acquisition. All the data is | |

normalized to the initial baseline condition. The three cyan rectangles denote the breath hold window (20 second duration each). b) Respiration time trace (from the BR sensor). The sensor returns a value proportional to the chest/lung volume. From this, it is possible to verify that the subject is actually holding the breath when requested by the examiner.95

Figure 6-8: Absorption (μa) and reduced scattering ($\mu s'$) spectra (upper and lower plot respectively) for each subject, measured with a TD-DOS system.97

Figure 6-9: Comparison of the baseline intensity (g_2 , left plot) and electric-field (g_1 , right plot) autocorrelations, measured at 785 nm (red curves) and 1000 nm (blue curves), for Early and Late gate (continuous and dashed lines, respectively). The two main effects observed are: i) an increase of the late gate β and ii) an approximately 5-fold decrease of the de-correlation time (i.e., g_1 decay rate). All curves refer to subject #1.99

Figure 6-10: Cuff occlusion experiments BFI time traces, measured at 1000 nm, for all the 4 subjects (1 Hz sampling rate). Blue circles and red crosses refer to the Early and Late gate, respectively. Figure from Ref. [170].100

List of Tables

| | |
|----------------------------------------------------------------------------------------------------------------------------------------------------------------------------------------------------------------------------------------------------------------------------------------|----|
| Table 1: Comparison of the three lasers modules. The quantities were extracted from the spectral (first three columns) and IRF (last two columns) measurements..... | 64 |
| Table 2: Comparison of the two single-photon detectors (SPAD and SNSPD) | 68 |
| Table 3: Values of the rBFI at the hyperaemic peak (10-20 s after the occlusion release), averaged across the three subjects, for the three considered laser sources (columns) and gate positions (rows)..... | 90 |
| Table 4: Superficial thickness and measured absorption and reduced scattering coefficients at 785 nm and 1000 nm. | 98 |
| Table 5: Results of the cuff occlusion experiment (averaged over the baseline period). The first 4 columns report the count rate and BFI (early gate, late gate, and ungated acquisition) measured at 1000 nm. As comparison, the ungated BFI measured at 785 nm is also reported..... | 99 |



Chapter 1: Diffuse optical techniques and applications

In this chapter, I will review the techniques and applications of diffuse optics. After a general introduction, I will introduce the two building blocks of this thesis work: near infrared spectroscopy (in particular the time-domain approach) and diffuse correlation spectroscopy. Then, I will introduce the subject of this thesis, namely time-domain diffuse correlation spectroscopy. Finally, I will summarize the state-of-the-art and the experimental challenges of the technique.

1.1. Light propagation in diffusive media

In thick biological tissues, light propagation is a combination of two effects: absorption and scattering. Here I will define the key parameters that describe light propagation in these materials, often referred to as turbid media [1–4].

Light absorption depends on the relative concentration of the different tissue constituents, or chromophores. It can be described by the absorption mean free path l_a , which is the average distance that a photon travels before it is absorbed by the medium. The absorption coefficient is defined as $\mu_a = 1/l_a$ (cm^{-1}), and can be interpreted as the probability of absorption per unit length of propagation.

A second parameter is the scattering mean free path l_s , which is the average distance that a photon travels before it is scattered (i.e., deflected). The scattering coefficient is defined accordingly as $\mu_s = 1/l_s$ (cm^{-1}). The scattering of light is due to the microscopic heterogeneities of the sample, on a scale comparable with the wavelength of light. This is due to the peculiar structure of biological tissues, which presents discontinuities of the local refractive index at the sub-cell level. Many biological tissues do not scatter light in an isotropic way. The angular properties of light scattering are enclosed in the anisotropy coefficient $g = \langle \cos(\theta) \rangle$, where θ is the scattering angle and $\langle \rangle$ denotes an ensemble average. The typical value for biological tissues is 0.7-0.9.

The last parameter I will introduce is the transport mean free path l_s^* , which is defined as the average distance which a photon travels before its direction is randomized. Its reciprocal, the reduced scattering coefficient, can be computed as $\mu_s' = \mu_s(1 - g)$ (cm^{-1}). In specific wavelength ranges, light absorption can be significantly lower than scattering, mathematically $\mu_a \ll \mu_s'$. In this regime, the propagation of light can be described as *diffusive*, or equivalently as a *random walk*.

In Figure 1-1, I show the specific absorption spectrum of the main biological tissue's constituents, so called chromophores. It might be noted that each chromophore has a peculiar spectral shape, but all of them has a relatively lower absorption in the range between 600 nm

and 900 nm. For this reason, that spectral region is often referred as *physiological window*. Due to the relatively low absorption, as compared to the (reduced) scattering, light can penetrate deep into biological tissues. For this reason, many diffuse optical techniques exploited this spectral windows, for probing biological tissues in normal or pathological conditions [5–8].

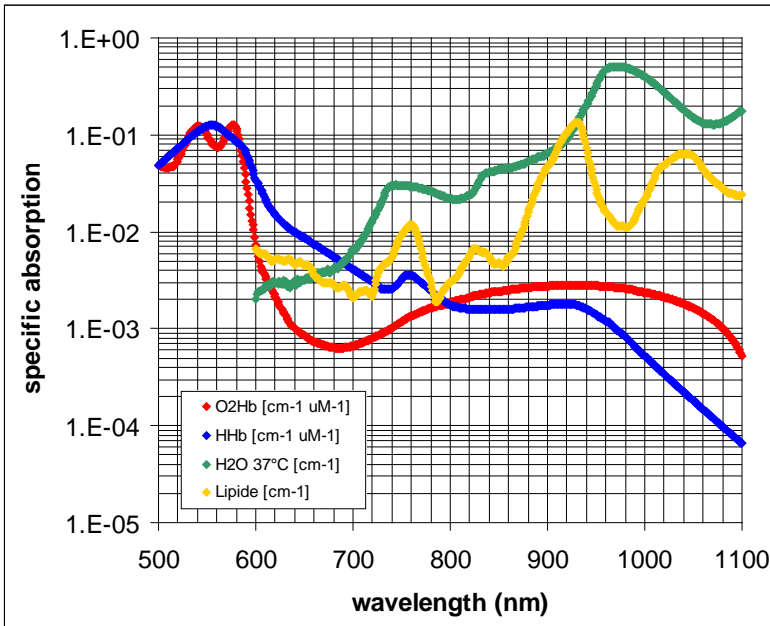


Figure 1-1: Specific absorption coefficient (absorption per unitary concentration) of the four main tissue chromophores: oxy- and deoxy-haemoglobin (O₂Hb/HHb, respectively), water and lipide. It might be noted that, in the range between 600 nm and 900 nm, light absorption is significantly lower compared to the other wavelengths. That spectral range is conventionally referred as “physiological window”. Figure from Ref. [9].

In the next sections I will describe the two diffuse optical techniques from which I developed this thesis: near infrared spectroscopy (NIRS) and diffuse correlation spectroscopy (DCS).

1.2. Near infrared spectroscopy

In this section, I will introduce the principles of Near infrared spectroscopy (NIRS), focusing on its biomedical applications. NIRS is

a non-invasive technique which aims to measure the tissue chromophores concentration, by using near infrared light at different wavelengths (λ) [1,8,10–12].

Jöbsis, in a pioneering work from 1977, showed that it is possible to measure the concentration of oxy and deoxy-haemoglobin (O_2Hb and HHb) in biological tissues [13]. From this, it is possible to retrieve two physiologically important quantities: the total haemoglobin concentration, $tHb = O_2Hb + HHb$, and the tissue oxygen saturation, $StO_2 = O_2Hb / tHb$.

In general, if the tissue is composed of N chromophores, the absorption coefficient can be written as:

$$\mu_a(\lambda) = \sum_{i=1}^N C_i \epsilon_i(\lambda), \quad (1-1)$$

In which C_i is the concentration of the i -th chromophore, and $\epsilon_i(\lambda)$ is the specific absorption. Thus, if the absorption coefficient is measured at M different wavelengths (with $M \geq N$), by inverting Equation (1-1) one can extract the concentration of each chromophore.

Regarding the geometry, the measurements can be performed either in reflectance or transmission, depending on the application and the sample size. In reflectance, the light source and detector are placed on the tissue at few cm distance. In transmission, used for instance for optical mammography, the source and detector are on the two sides of the sample [1].

The four main approaches to NIRS are: continuous wave [10], frequency-domain [11], spatial frequency domain [12], and time-domain [8] (see Figure 1-2).

- In the **continuous wave** (CW) approach, a steady-state light source is injected in the tissue, and a detector measures the intensity of the diffused photons. In certain cases, light is modulated at kHz frequencies to improve the sensitivity.
- The **frequency-domain** approach uses a sinusoidally modulated (~ 100 MHz) light source, and the amplitude and phase shift of the diffused light is recorded.

- **Spatial-frequency domain** uses spatial modulation of the excitation light and measures the corresponding spatial shift.
- The **time-domain** (TD) approach exploits a pulsed laser (~ 100 ps duration) for measuring the temporal distribution of the re-emitted photons, so-called distribution of time-of-flights (DTOF).

The CW approach is the simplest but cannot easily disentangle the effect of scattering from absorption, since it measures the overall attenuation which is a combination of the two parameters. Thus, unless a multi-distance approach with calibrated detectors is used [14], it can measure only relative (absorption) changes. The frequency-domain, spatial frequency-domain, and time-domain approaches, on the other hand, can retrieve simultaneously the absorption and reduced scattering coefficient of the sample.

In the next section, I will focus on the time-domain approach, which has been used extensively in this thesis work.

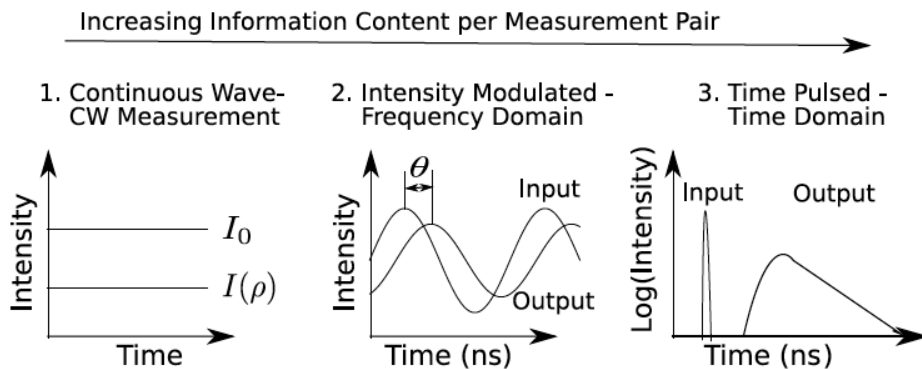


Figure 1-2: Three different approaches to NIRS: 1) Continuous wave, 2) Frequency-domain, 3) Time-domain. Spatial frequency domain (not shown) modulates the light source over the spatial, instead of the temporal, dimension. Adapted from Ref. [1].

1.2.1. Time-domain NIRS

In this section I will discuss more in detail time-domain near infrared spectroscopy (TD-NIRS) [8,15–17]. As introduced in the previous section, in TD-NIRS a short (~ 100 ps) laser pulse is injected in the

tissue. Then, the diffused photons are collected, either in reflectance or transmittance geometry, by means of an optical fiber and a single-photon photodetector, and the photon time-of-flight distribution (DTOF) is recorded, see Figure 1-3. The absorption and scattering events modify the temporal shape of the injected pulse in different ways. In particular, the scattering broadens and delays the pulse, while the absorption affects the DTOF tail at later times. Thus, using the TD approach, it is possible to *disentangle absorption from scattering*, retrieving μ_a and μ'_s simultaneously.

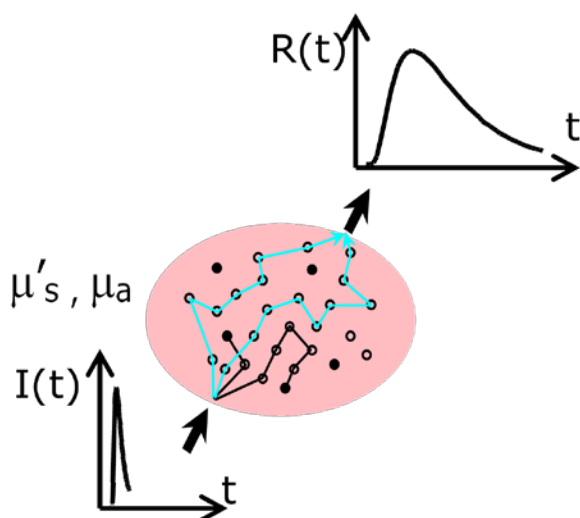


Figure 1-3: Principle of TD-NIRS. A short (few hundred picoseconds) laser pulse is injected in the sample, and the distribution of time-of-flights (DTOF) of the diffused photons is recorded. The DTOF carries useful information regarding the sample optical properties.

Now I will discuss the second property of TD-NIRS: the *depth discrimination*. In reflectance geometry, the diffusive properties of the tissues enable to detect photons which reach depths up to few centimetres. Since light diffusion is essentially a random walk, the depth penetration of each photon is a random quantity. However, for longer time-of-flights, the diffused photons statistically visited deeper regions of the tissue. This physical property has been demonstrated both theoretically and experimentally [8,15,18,19]. In Figure 1-4, the

photon visiting probability, so called sensitivity maps, are shown for different time-of-flights and source-detector separations (ρ).

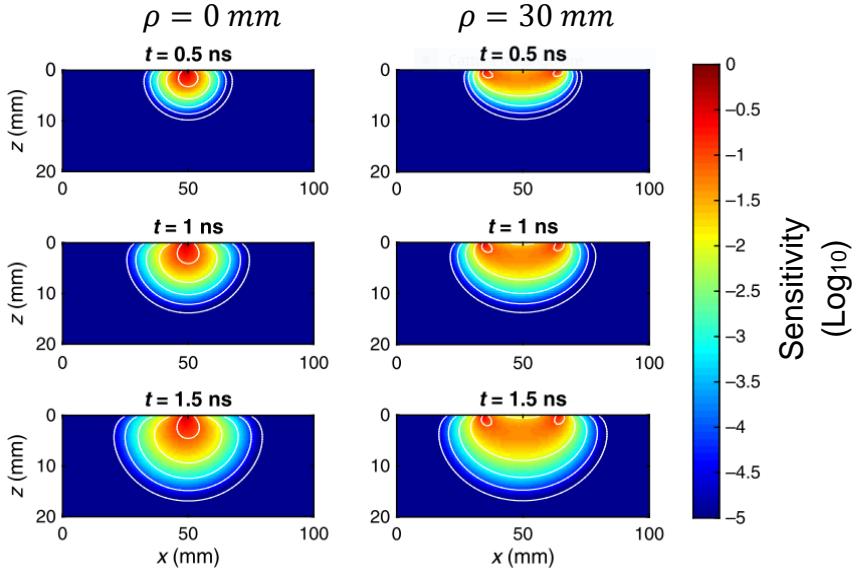


Figure 1-4: Comparison of the sensitivity maps for three different time-of-flights ($t = 0.5 \text{ ns}$, 1 ns and 1.5 ns : top, middle, and lower plots). Light is injected and collected on the top surface of the medium, in reflectance geometry. The source-detector (SD) separation (ρ) is 0 mm and 30 mm for the left and right plots, respectively. While the penetration depth increases with the time-of-flight, it does not depend significantly on the SD separation. Figure adapted from Ref. [15].

As opposite to the CW approach, where the depth discrimination can be obtained only by changing ρ , in the time-domain approach it is possible to retrieve depth discrimination by selecting (i.e., gating) the photons based on their time-of-flight. This “time/depth” relationship was showed to be independent on the source-detector (SD) separation, as can be seen from Figure 1-4.

In this section, I discussed the general principle of NIRS, then focusing on the time-domain approach, which will be one of the building blocks of this thesis work. In the next sections, I will introduce the second building block: diffuse correlation spectroscopy (DCS). Then, I will

discuss what are the possible synergies between the two techniques, and the main challenges of the resulting technique, time-domain DCS.

1.3. Dynamic scattering techniques

In this section, I will introduce the principal methods that have been developed for *particle motion* measurements with laser light. First, I will introduce the concept of laser speckle, which is fundamental for the following, then I will present the main techniques.

1.3.1. Laser speckle

Even if light propagation in turbid media seems a random process, light scattering is actually deterministic. In fact, every scattering event is due to the microscopic inhomogeneities of the sample's refractive index, which are very difficult to model, but create reproducible effects. An important example of this is laser *speckle* [20]. When light propagates through a random medium, and then is projected to a screen, every photon accumulates a phase shift given by its actual path length. For this reason, after several scattering events, their phase becomes uncorrelated and uniformly distributed. Thus, we can interpret the field of each photon as a random (complex) phasor. When many independent phasors are added, due to the central limit theorem the total field follows a zero-mean gaussian distribution on the complex plane, which corresponds to a Rayleigh (i.e., negative exponential) intensity distribution [21], see Figure 1-5.

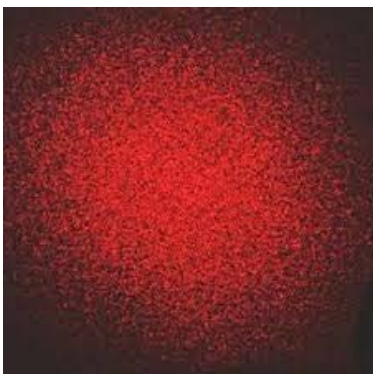


Figure 1-5: Image of a laser speckle pattern on a screen.

Physically, we can interpret laser speckle as an interference effect between all the photons that reach the detection screen. Thus, in order to measure it, a temporally coherent light source is needed. For obtaining a speckle pattern, the coherence length of the light source needs to be comparable with the average path length difference. Or equivalently, the source bandwidth should be smaller than the spectral dispersion of the medium [22,23].

1.3.2. Laser speckle contrast and Laser Doppler Flowmetry

Now I will discuss the two main methods that have been developed for measuring *particles motion*. The two main methods are i) laser speckle contrast [24–26] and ii) laser doppler flowmetry [27,28].

If we suppose that all the particles of the medium are fixed, the resulting speckle pattern will be constant over time, due to the deterministic nature of light scattering. However, if the particles move, the photons will undergo slight phase shifts which will modify the resulting speckle pattern. Thus, monitoring the speckle pattern over time it is possible to infer information about the particles speed. If we imagine using a camera with a fixed integration time, we will see that the particle motion will smear the speckle pattern, thus reducing its contrast for integration times slower than motion itself. Thus, the contrast of the resulting speckle pattern carries useful information regarding the dynamics of the medium. This is the principle of the technique referred laser speckle contrast imaging/analysis (LSCI/LSCA) [24,25,29–33].

Instead of looking at the temporal effects of the dynamic scattering, it is possible also to look at the spectral effects. In particular, when light is scattered by a dynamic object, the photons will undergo slight frequency shifts due to the Doppler effect. This Doppler shifts will accumulate when the photons undergo multiple dynamic scattering. Thus, the spectrum of the detected light will be broadened by the motion of the scatterers. If the light source is sufficiently narrow band, the spectral changes can be measured quantitatively. This is the principle of the technique named laser doppler flowmetry (LDF) [27,34–37].

Let me note that laser speckle contrast and laser doppler flowmetry, even though technically different, are based on two similar physical

concepts. The first focuses on the temporal dispersion due to dynamic scattering, the second on the corresponding spectral dispersion. Mathematically, their correspondence is assured by the Wiener–Khinchin theorem [28,38–42].

1.3.3. Diffuse Correlation Spectroscopy

As we have seen in the previous section, laser speckle carries useful information regarding dynamic scattering. Laser speckle contrast (LSC) is a relatively simple, possibly wide-field, technique. However, since LSC samples the speckle (temporal) fluctuations with a single integration time, it has limited accuracy [31]. In fact, one needs to assume the type of particle motion (e.g. Brownian/directional) and scattering regime (e.g. single/multiple events) for a quantitative analysis [24,25].

A different approach is given by Diffusing wave spectroscopy (DWS), often called Diffuse correlation spectroscopy (DCS) in the biomedical field [1,43–51]. In DCS, the diffused light intensity is measured with $\mu\text{s} - \text{ns}$ resolution, by means of a single-photon detector. Then, the autocorrelation function is computed on a wide span of lag times ($\tau = 1 \mu\text{s} \div 1 \text{s}$), see Figure 1-6.

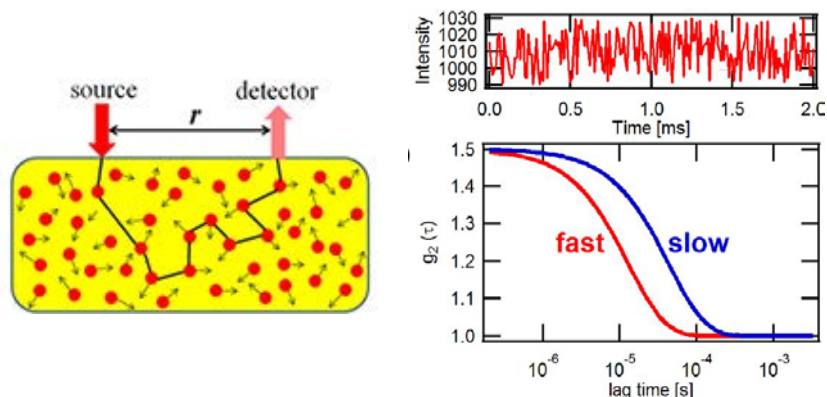


Figure 1-6: Principle of diffuse correlation spectroscopy (DCS). When photons undergo dynamic scattering events, the diffused light intensity (on a single speckle) fluctuates over time. Faster particles correspond to faster intensity fluctuations. This is typically quantified calculating the intensity autocorrelation function g_2 as a function of delay time τ .

As shown in Figure 1-6, photons undergo many scattering events during their travel from the source to the detector. As a result, the detected intensity will fluctuate over time. Faster particles motion will then correspond to faster intensity fluctuations. Typically, this is quantified by computing the diffused intensity auto-correlation function $g_2(\tau)$. It can be showed that its decay rate is directly related to the particle motion, in particular the mean squared displacement $\langle \Delta r^2(\tau) \rangle$ [52–54].

Compared to laser speckle contrast methods, unless multiple integration times are used [31,34,55–59], DCS can quantify particles motion is a more accurate way, due to the fact that the intensity is measured with faster detectors ($\mu s - ns$ resolution), thus measuring the full intensity autocorrelation [$g_2(\tau)$] decay.

1.4. Time resolved dynamic scattering techniques

In this section, I will introduce time-resolved dynamic scattering techniques, then I will focus on time domain (TD) DCS, which is the subject of this thesis work.

As discussed in the previous section, DCS has the possibility to measure the motion of scattering particles in the multiple scattering regime. However, it has two main limitations. The first is that, for an accurate estimation, it requires precise knowledge of the optical properties (scattering and absorption) and geometry of the sample [60–63]. The second is that it has a limited depth resolution, unless multiple source-detector (SD) distances [64–66], or complex reconstruction algorithms [67–69], are used. This is related to the fact that photons with any possible path length contribute to the measured autocorrelation.

In order to overcome these challenges, researchers have investigated path length resolved dynamic scattering methods [70–73]. The aim of

this methods is to discriminate the speckle fluctuations with respect to the photon path length, or equivalently its time-of-flight.

The first pioneering work, by Yodh *et al.* [70] in 1990, used a mode-locked laser and a delay-scanned interferometer, to measure intensity fluctuations at different delay times. The detection side was based on second-harmonic generation, thus a high light power (~ 1 W) was required. Later, a method based on a coherence-gated interferometer coupled with a spectrum analyser was proposed [71,74], enabling the study of both the few-scattering (quasi-elastic scattering) and the multiple scattering (DWS) regimes.

A different approach is the use of a wavelength-swept (i.e., frequency modulated) source, with interferometric detection, to retrieve by Fourier transform the path length resolved speckle fluctuations. The method was originally envisioned for the measurement of the distribution of time-of-flights (DToF) [75,76], then adapted for measuring also the auto-correlation [72,73,77]. In the next section I will introduce a more direct approach, time-domain (TD) DCS, which is the subject of this thesis work.

1.4.1. Time-domain DCS

Very recently, Sutin *et al.* demonstrated a new approach for path length resolved dynamics measurements, termed time-domain (TD) DCS, with measurements on tissue-mimicking phantoms and small animals [78]. a pulsed near infrared laser, with temporal duration < 100 ps and high temporal coherence, a fast single-photon detector, and a time-correlated single photon counting (TCSPC) board. In their work, the researchers used a semiconductor-based laser with non-ideal temporal coherence, which is required for an accurate measurement of the speckle fluctuations, and thus the BFI. In order to overcome this challenge, Pagliazzi *et al.* exploited a highly coherent Ti:Sapphire laser (in mode-locking regime), which strongly improved the signal-to-noise ratio (SNR). This enabled to perform the first *in vivo* experiments on human subjects, with measurements on muscle and brain [79,80].

The principle of TD-DCS is to measure, for every detected photon, two key quantities:

- i) The **absolute arrival time** (with respect to the beginning of the experiment) with ns resolution, sometimes named macro-time.
- ii) The **time-of-flight**, with ps resolution, sometimes termed micro-time.

The time-of-flight information can be used for binning the measured photons in several temporal windows, named time-gates, thus for discriminating different photon path lengths. Then, for every time-gate, the corresponding intensity time trace, and thus its auto-correlation function, can be measured using the macro-times of the selected photons. From the autocorrelation of every time-gate, it is then possible to retrieve a dynamics parameter (e.g., mean square displacement).

The measured time-of-flight can also be used for computing the distribution of time-of-flights (DTOF), which carries useful information about the sample optical properties (absorption and reduced scattering).

Potential advantages of TD-DCS

With respect to classical (i.e. CW) DCS, the time-domain approach has two potential advantages [78]:

1. Firstly, due to the possibility to discriminate the dynamics with respect to the photon path length, it might be possible to obtain depth resolved dynamics measurements. This could be done by exploiting the physical relationship between photon time-of-flight and depth, already exploited extensively in time-domain NIRS [19,81–84] (see Section 1.2.1).
2. Secondly, thanks to the parallel measurement of the DTOF, it is possible to retrieve information regarding the sample optical properties [70,72,76–78]. This information would be useful for characterizing the sample with a single technique. In addition, the knowledge of the optical properties, especially the reduced

scattering coefficient, enables a quantitative analysis of the DCS data. Otherwise, a separate NIRS system would be needed [7,85–87].

Let me highlight that both the points were demonstrated only partially in the previous works, and thus will be studied in detail in this thesis.

Challenges of TD DCS

I will now briefly discuss the challenges of TD DCS:

1. First of all, as I discussed in section 1.3, to detect the speckle (which is actually an interference effect) the light source needs to have a sufficient *temporal coherence* or equivalently a narrow spectrum. However, in the case of TD-DCS, the light source needs to be pulsed to retrieve the path length resolution. Thus, there is a very strict trade-off between the temporal vs spectral widths of the light source being used, essentially set by the Fourier limit [23,88–92]. In a following chapter, I will study in detail the effect of laser coherence on the amplitude of the auto-correlation function (which is typically called coherence parameter β).
2. In addition, a *single-mode detection* channel (typically a single mode fiber) needs to be used for light collection. This is due to the fact that the contrast in the speckle fluctuations is inversely proportional to the number of detected modes [21,93]. Thus, even if more photons are collected, detecting more modes would not increase the signal-to-noise ratio (SNR) significantly [34,94,95]. Thus, strategies need to be studied to keep the SNR at a reasonable level. Let me note that, for classical (CW) DCS, some interferometric approaches have been recently proposed to add the individual modes in a coherent way [96,97].

1.5. Comparison with other techniques and applications

The key biomedical application of DCS is the measurement of *microvascular* blood flow (BF) [1,6,98]. In fact, in the case of biological tissues, the main moving scatterers are the red blood cells (RBC). It has been demonstrated that the speckle fluctuations are related to the specific type of motion (shear motion) of the RCB within the micro-circulation [51]. In the next chapter, I will describe the principle for extracting the BF index from the intensity autocorrelation, which indeed is proportional to the BF in the tissue.

In the next Section, I will discuss several validations of the technique and its main biomedical applications.

1.5.1. DCS validation with blood flow monitoring techniques

Several validation studies have been carried out to compare and validate DCS with techniques typically used in the clinics. Few examples are:

- *Transcranial Doppler ultrasound (TCD)*. TCD is an ultrasound technique which exploits the doppler shift to measure macro-vascular blood flow, as opposite of DCS which measures the micro-circulation. For transcranial measurements, TCD typically measures the flow in the middle cerebral artery. It was shown that the BF index from DCS was statistically correlated with the TCD counterpart (systolic, diastolic and mean BF), even if the two techniques measure different types of vasculature [99,100]. The two techniques were also validated on muscle measurements [101], and on tumoral tissues [49,102].
- *Arterial-Spin-Labelled Magnetic Resonance Imaging (ASL-MRI)*. ASL-MRI is one of the gold standards to image the tissue blood flow with high spatial resolution. However, due to its bulkiness it is not usable at the bedside and its very costly. DCS was extensively validated with ASL-MRI, both for muscle and brain measurements, and showed an high degree of correlation [1,6,47,103,104].

- *Xenon Computed Tomography (Xe-CT)*. It is a CT scanning technique where the subject inhales Xenon as contrast agent. It is typically used to image blood flow in the case of traumatic brain injuries or stroke. As in the case of ASL-MRI, relies on bulky equipment thus is not applicable at the bedside. DCS was validated against Xe-CT in the case of critically-ill subjects [6,7,105].

After having discussed the different validations of DCS, now I will summarize the main biomedical applications of DCS.

1.5.2. DCS biomedical and clinical applications

DCS has been used for a variety of biomedical and clinical applications, in particular to measure tissue hemodynamic in *brain, muscles and tumours*. The main applications studied so far are:

- *Brain hemodynamics*. For almost two decades, DCS has been applied to the study of brain hemodynamics, both for physiology and pathology studies [106,107]. It was first applied to rats for disease monitoring and imaging [94,108]. Then, it was applied to study cerebral injuries in piglets and humans [7,109]. Shortly after, functional DCS, i.e. measuring the cerebral response to external stimuli, was demonstrated on several cerebral regions (e.g. motor, cognitive) [86,106]. In this regard, DCS was compared with ASL-MRI and functional MRI and showed comparable results [1]. DCS was also used in the clinic to monitor premature babies [99], infants with congenital defects [103], traumatic brain injuries [7], stroke [110], and deep hypothermia surgery [111].
- *Muscle hemodynamics*. DCS was also used to study muscle hemodynamics [47,87,101,112–114]. For instance, the auto-regulatory response of periphery artery disease (PAD) patients was compared with healthy subject. PAD is a circulation disease which is caused by the narrowing of arteries in muscular tissues, typically on the limbs. Between the two groups, a different auto-

regulatory response was found [87]. Also, efforts to use DCS with dynamically exercising muscles are ongoing [115].

- *Tumour diagnosis and therapy monitoring.* The technique was extensively used to studying tumoral diseases, both for diagnosis and therapy monitoring purposes [49,102]. For instance, DCS (and NIRS) have been used for breast cancer imaging and chemotherapy monitoring [116,117]. It was also used to study the effects of photodynamic therapy (PDT) e.g., in prostate cancer [102,118]. The technique was exploited because the efficacy of PDT is correlated with the oxygen content of the tumours (hypoxic tumours are more difficult to treat) [119]. Also, the treatment itself can change the tumour metabolic status, which needs to be monitored for keeping effective the treatment. Finally, monitoring the tumour early response to the treatment may enable to predict its long-term healing probability [49].

In this section, I have briefly described other (non-optical) blood flow monitoring techniques, which were used to validate DCS. Then, I discussed the main biomedical and clinical applications of the technique. Let me stress that those applications might be possible as well for TD-DCS.

In the next chapter, I will describe the theoretical framework of DCS, and then focus on the theory of TD-DCS (which was partially developed during this thesis work).

Chapter 2: Theory

In this chapter, first I will briefly review the theory of photon propagation in diffusive media. Then, I will present the theory of dynamic scattering, in the single and multiple scattering (DCS) regimes. Finally, as a result of this thesis work, I will present the theory of time-domain DCS, focusing on the effects of the system temporal response.

2.1. The photon diffusion equation

As we have seen in the previous chapter, light propagation in turbid media can be interpreted as a *diffusive* process. Let me note that diffusive processes are encountered often in natural phenomena such as heat propagation, acoustic/seismic waves, chemistry etc.

The most rigorous description of light propagation in a diffusive medium is given by the radiative transfer equation (RTE), a theory initially developed for describing the neutron propagation (in astrophysics and nuclear physics), [2,120–122]. Its main ingredients are: i) absorption events (μ_a), ii) scattering events (μ_s), iii) scattering angle θ , described statistically by the scattering phase function $p(\cos(\theta))$. The phase function characterizes the sample's distribution of scattering angles. The RTE describes the spatial and temporal behaviour of the radiance $L(\mathbf{r}, t, \boldsymbol{\Omega}) [\frac{W}{sr\ cm^2}]$, which is defined as the optical power per unit area travelling in the $\boldsymbol{\Omega}$ direction, at position \mathbf{r} and time t . It is possible to solve the RTE analytically only for very simple configurations. On the other hand, it is possible to solve numerically the equation, for instance with Monte Carlo simulations [122–124].

In order to obtain a more treatable version of the RTE, few assumptions are needed. Most importantly, the reduced scattering coefficient $\mu'_s = (1 - g)\mu_s$, needs to be much bigger than the absorption coefficient μ_a . In addition, the radiance is assumed to be almost isotropic (the so-called P1 approximation), and it also needs to not vary significantly in the time-scale in which a photon travels a transport mean free path l^* [2,3]. With these approximations, the RTE reduces to a simpler equation, namely the photon diffusion equation (PDE). The PDE describes the spatial and temporal distribution of the photon intensity, so-called fluence $\phi(\mathbf{r}, t) [W/cm^2]$:

$$\nabla \cdot (D(\mathbf{r})\nabla\phi(\mathbf{r}, t)) - v\mu_a(\mathbf{r})\phi(\mathbf{r}, t) - \frac{\partial\phi}{\partial t} = -vS(\mathbf{r}, t). \quad (2-1)$$

In Eq. (2-1), $D(\mathbf{r})$ is the diffusion coefficient, defined as $1/(3\mu'_s)$. The speed of light in the medium is v , and $S(\mathbf{r}, t)$ is the light source term (assumed to be isotropic). Once the source term and the optical properties are defined, it is possible to solve the PDE, and thus retrieving the fluence $\phi(\mathbf{r}, t)$, either analytically or numerically, e.g. with the finite elements method (FEM) [2,3].

It is important to note that the fluence $\phi(\mathbf{r}, t)$ represents the light power distribution *inside* the medium. The *re-emitted* power per unit area and time, either in transmission or in reflectance geometry, can be computed by exploiting the boundary conditions as follows [125]:

$$R(\mathbf{r}, t) \text{ or } T(\mathbf{r}, t) = -D(\mathbf{r})|\nabla\phi(\mathbf{r}, t)|_{\mathbf{r} \in \text{surface}} \quad (2-2)$$

2.1.1. Time-resolved diffuse reflectance

The solution of the PDE depends on the geometry and the type of source used. For the case of a Dirac δ pulsed light source, assuming a semi-infinite homogeneous medium, the reflectance can be expressed as [126]:

$$R(t) = kt^{-\frac{5}{2}} \exp(-\mu_a vt) \exp\left(-\frac{\rho^2}{4Dvt}\right) S(D, t), \quad (2-3)$$

in which ρ is the source-detector separation, k is a proportionality coefficient, and $S(D, t)$ is a dipole term (boundary conditions dependant).

In Figure 2-1, the theoretical time-resolved reflectance, calculated using Eq. (2-3), is reported for different values of absorption and reduced scattering. As can be seen, the absorption coefficient mostly influences the amplitude and the slope of the tail. On the other hand, the reduced scattering coefficient mainly influences the curve broadening and the peak position [8].

In the following, I will show that $R(t)$ plays an important role in the theory of TD-DCS, since it can be used to compute the distribution of time-of-flights, or equivalently the path length distribution $P(s = vt)$.

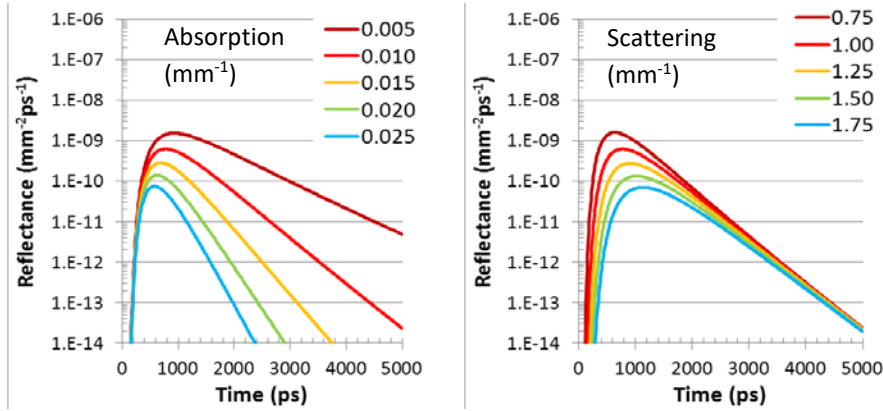


Figure 2-1: Time-resolved diffuse reflectance for a semi-infinite medium. Dependence on a) the absorption coefficient (in mm^{-1}) and b) the reduced scattering coefficient (in mm^{-1}). Figure adapted from Ref. [8].

It is important to note that the RTE in general, and the PDE in particular, completely neglect wave interference effects. In fact, they assume that the different light fields add up incoherently [3]. As a consequence, their solutions are not accurate in the presence of coherent effects, such as laser speckle [127–129]. However, they can be used to compute *ensemble-averaged* quantities. In the last chapter, I will show experimental evidence of this in the case of time-domain diffuse optics.

2.2. Speckle statistics

In this section I will discuss the main statistical properties of speckle patterns. As introduced in Section 1.3.1, laser speckle can arise from the light interference of multiply scattered light. In this conditions, the overall field amplitude $A(\mathbf{r})$ can be interpreted as a phasor sum in the complex plane [20,130,131]:

$$A(\mathbf{r}) = \sum_{i=1}^{N_{\text{paths}}} a_i \exp(i\Phi_i) \quad (2-4)$$

In order to carry out the sum in Eq. (2-4), we need to make two assumptions:

- The amplitude a_i and phase Φ_i of the individual field contributions are random quantities and uncorrelated to each other. Also, the different field components are considered to be independent.
- The phase Φ_i is assumed to be uniformly distributed between 0 and 2π . This corresponds to assume that the photon path lengths differences are much larger than a wavelength.

With these two assumptions, the problem becomes equivalent to a random walk in a 2D plane. Thus, we can interpret the speckle formation as a random walk in the complex plane (since the individual field contributions are complex). Assuming finally that a large number of field contributions are present, the resulting intensity can be shown to follow a negative exponential distribution [20,21]:

$$p(I) = \left(\frac{1}{\bar{I}}\right) \exp(-I/\bar{I}) \quad (2-5)$$

where \bar{I} is the mean intensity. From Eq. (2-4), it is possible to understand why in a speckle pattern the black points (i.e., low intensity) are much more probable than the bright ones (i.e., high intensity). A simple parameter for characterizing a speckle pattern is the so-called speckle contrast C , defined as [130]:

$$C = \frac{\sigma(I)}{\langle I \rangle} (\leq 1) \quad (2-6)$$

where $\sigma(I)$ is the standard deviation of the intensity and $\langle I \rangle$ is the ensemble average of the intensity. In the ideal case of a single-polarization, monochromatic speckle pattern (thus following Eq. (2-4)) the speckle contrast C is equal to one. On the other hand, when M different speckle patterns are added incoherently, the corresponding speckle contrast C is reduced by a factor \sqrt{M} [20]. For instance, in the case of unpolarized light the ideal value of the speckle contrast is $1/\sqrt{2}$. The speckle contrast may degrade also when large bandwidth sources are used. Following this concept, it is possible to define the *sample bandwidth* as the wavelength/frequency difference which corresponds to two uncorrelated speckle patterns [22,92].

2.2.1. Generalized speckle intensity distribution

As described in the previous sub-section, when multiple speckles are spatially (or temporally) averaged their relative variations are reduced, proportionally to the number of averaged modes M . It was demonstrated that, in these conditions, the overall intensity distribution is given by a Gamma distribution [20,21]:

$$p(I) = \frac{a^M I^{M-1} \exp(-aI)}{\Gamma(M)} \quad (2-7)$$

In which a is a normalization factor, defined as $M/a = \langle I \rangle$, and Γ denote the Gamma function. It is possible to show that the above distribution satisfies the speckle contrast condition $\sigma(I)/\langle I \rangle = 1/\sqrt{M}$. Thus, for higher number of modes M the distribution narrows around the average intensity $\langle I \rangle$.

Goodman studied in detail the limits of validity of Eq. (2-7), and in particular showed how it generalizes in the presence of Poisson noise. Without entering in detail, the general distribution can be computed by statistically mixing the Gamma and the Poisson distributions, obtaining a distribution called negative binomial [21]. Interestingly, the standard deviation of the overall distribution can be written as [132]:

$$\sigma_I^2 = \langle I \rangle + \frac{1}{M} \langle I \rangle^2 \quad (2-8)$$

Thus, we can see from Eq. (2-8) that the overall variance is simply the sum of the variances of Poisson noise and speckle fluctuations, respectively. I will show the utility of the previous equation in the last chapter, where I studied the effects of speckle fluctuations in time-domain diffuse optical measurements [133].

In this section, I discussed the theory of speckle patterns, focusing on their statistical features. In the next section, I will summarize the properties of dynamic speckles, moving from the single to the multiple scattering regime. Afterwards, I will move to the theory of DCS and time-domain DCS.

2.3. Diffuse correlation spectroscopy

In this section, I will present the theory of dynamic scattering techniques, starting from the single-scattering regime and then moving to the multiple-scattering case.

2.3.1. Single scattering regime (dynamic light scattering)

Here I will start by considering a single-scattering experiment, as it is done in dynamic light scattering (DLS) [134–136]. In DLS, a long coherence length laser is delivered to a sample (sufficiently diluted to assure single-scattering), and light is collected with a single-photon detector at a fixed scattering angle θ , as depicted in Figure 2-2.

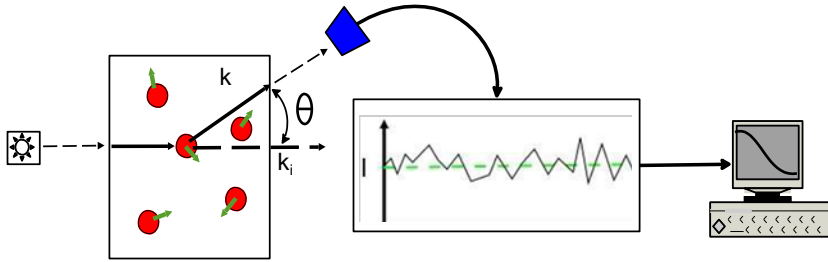


Figure 2-2: Dynamic light scattering (DLS) experiment. A diluted sample is illuminated by a coherent laser and light scattered at a fixed angle θ is collected. The light intensity auto-correlation function is then computed and analysed.

The total scattered electric field can be written as a sum over the N_{part} different scattering particles present in the illuminated volume [134]:

$$E_{tot} \propto \mathbf{E}_o F(\theta) e^{-i\omega t} \sum_{i=1}^{N_{part}} \exp(-i\mathbf{q} \cdot \mathbf{r}_i(t)), \quad (2-9)$$

where \mathbf{E}_o is the incident field, $F(\theta)$ is the scattering form factor, ω is the light angular frequency, $\mathbf{q} = \mathbf{k}_{out} - \mathbf{k}_{in}$ is the wavevector difference, and $\mathbf{r}_i(t)$ is the position of each scattering particle. By computing the normalized electric-field auto-correlation function $g_1(\tau)$, one obtains:

$$\begin{aligned}
g_1(\tau) &\equiv \frac{\langle \mathbf{E}_{tot}(t) \cdot \mathbf{E}_{tot}(t + \tau)^* \rangle}{\langle \mathbf{E}_{tot}(t) \cdot \mathbf{E}_{tot}(t)^* \rangle} = \\
&= e^{i\omega t} \langle \exp(i\mathbf{q} \cdot \Delta\mathbf{r}(\tau)) \rangle,
\end{aligned} \tag{2-10}$$

In which $\Delta\mathbf{r}(\tau)$ is the particle displacement between time t and time $t + \tau$, and $\langle \dots \rangle$ denotes an *ensemble average* i.e., an average over all the possible sample realizations. Eq. (2-10) holds for randomly positioned particles, having uncorrelated displacements. In the case of random Gaussian motion, for instance Brownian, it is possible to compute explicitly the ensemble average, obtaining [134]:

$$g_1(\tau) = e^{i\omega t} \exp\left(-\frac{1}{6}q^2 \langle \Delta r^2(\tau) \rangle\right), \tag{2-11}$$

where $\langle \Delta r^2(\tau) \rangle$ is the mean-squared displacement (MSD) of the scattering particles, at delay time τ .

It is important to note that, in most experiments, the scattered intensity is measured instead of the electric field. Nevertheless, when the scattered field is Gaussian and the sample is ergodic (i.e., temporal and ensemble averages are equivalent), the so-called Siegert relationship can be used [137,138]:

$$g_2(\tau) \equiv \frac{\langle I(t)I(t + \tau) \rangle}{\langle I(t) \rangle^2} = 1 + \beta |g_1(\tau)|^2. \tag{2-12}$$

In Eq. (2-11), $g_2(\tau)$ is the scattered intensity auto-correlation function, and β is the so-called coherence parameter. The β parameter is strictly related to the speckle contrast C , introduced in Sec 2.2, as it depends on the degree of coherence of the light source. Also, it is inversely proportional to the number of collected speckles/coherence areas. It is defined as the value of the intensity autocorrelation g_2 in the origin (i.e., at $\tau = 0$). For this reason, as opposite of the speckle contrast C , the coherence parameter β does not depend on the dynamics of the medium. However, β might depend on the optical properties of the sample (see Chapter 4).

Thus, we can see from Eq. (2-11) that from a measurement of the intensity auto-correlation function, it is possible to retrieve the electric-

field auto-correlation function, which enables to obtain the particles dynamics (specifically their MSD). In the next subsection, I will present the theory for the multiple-scattering regime, which will be particularly useful for DCS.

2.3.2. Multiple scattering regime (DCS)

In this section, I will describe the theory of dynamic scattering in the multiple-scattering regime [70,139,140]. When light is diffused through a turbid medium, photons undergo several scattering events. When the scatterers move, the photon paths change slightly, see Figure 2-3.

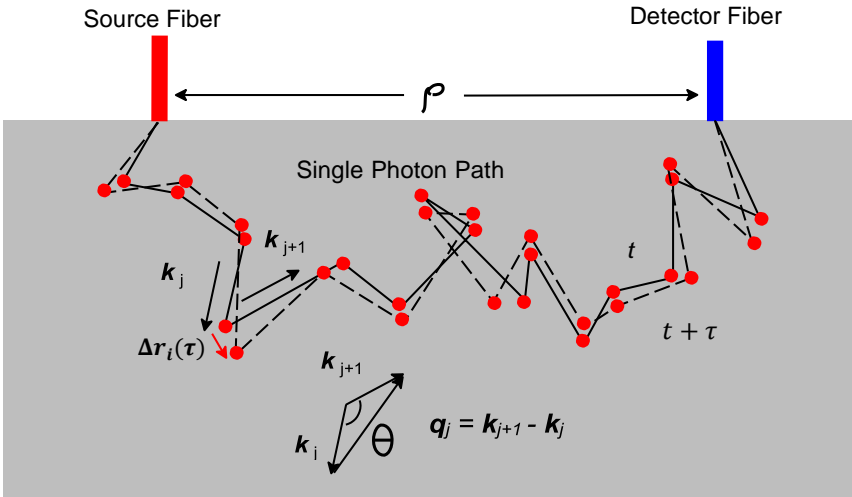


Figure 2-3: Photon trajectories in a typical DCS experiment. Photons are multiply scattered between the source and injection points. When the scatterers move, the photon trajectories undergo slight changes which modify their phases (and thus the resulting intensity). From Ref. [141].

Similarly to Eq. (2-9), the detected electric field of a single path E_{single} can be written as [139,142]:

$$E_{single} \propto E_o e^{-i\omega t} \prod_{j=1}^{N_s} F(\theta_j) \exp(-i\mathbf{q}_j \cdot \mathbf{r}_j(t)). \quad (2-13)$$

In the two products, we include all the N_s scattering events of the given path (the index j denote the individual scattering event, see Figure 2-3). The single path electric-field auto-correlation $g_{1,single}(\tau)$ might then be written as [138,141]:

$$g_{1,single}(\tau) \equiv \frac{\langle \mathbf{E}_{single}(t) \cdot \mathbf{E}_{single}(t + \tau)^* \rangle}{\langle \mathbf{E}_{single}(t) \cdot \mathbf{E}_{single}(t)^* \rangle} =$$

$$= e^{i\omega\tau} \left\langle \prod_{j=1}^{N_s} \exp(i\mathbf{q}_j \cdot \Delta\mathbf{r}_j(t)) \right\rangle. \quad (2-14)$$

As for DLS, assuming that each scattering event is independent, and the scatterers motion is Gaussian, one obtains for the single path autocorrelation:

$$g_{1,single}(\tau) = e^{i\omega\tau} \exp\left(-\frac{1}{3}k_0^2 Y \langle \Delta r^2(\tau) \rangle\right), \quad (2-15)$$

where Y is the so-called adimensional momentum transfer, defined as $Y = \sum_{j=1}^{N_s} [1 - \cos(\theta_j)]$. For a high number of scattering events (N_s), the momentum transfer can be approximated as $Y \cong N_s \langle 1 - \cos(\theta) \rangle = N_s(1 - g)$, where g is the anisotropy factor. Finally, noting that $N_s = \frac{s}{l_s}$, where s is the photon path length l_s is the mean scattering length, we obtain:

$$g_{1,single}(\tau) = e^{i\omega\tau} \exp\left(-\frac{1}{3}k_0^2 \mu'_s s \langle \Delta r^2(\tau) \rangle\right), \quad (2-16)$$

In Eq. (2-16), the definition of reduced scattering coefficient $\mu'_s = \frac{1}{l_s}(1 - g)$ was used. Thus, we see that the auto-correlation envelope is an exponential, with a decay rate determined the photon path length s and the scatterers motion $\langle \Delta r^2(\tau) \rangle$.

The overall auto-correlation, assuming that the fields of the individual path lengths are uncorrelated, might be written as a weighted sum over the path length distribution $P(s)$ [139–142]:

$$g_1(\tau) = \int_0^{+\infty} P(s) \exp\left(-\frac{1}{3}k_0^2\mu'_s s \langle \Delta r^2(\tau) \rangle\right) ds. \quad (2-17)$$

The path length distribution $P(s)$ can be estimated using the theoretical time-resolved diffuse reflectance/transmittance (normalized to unitary area). Thus, in the multiple-scattering regime the auto-correlation function can be expressed by an average of the single-path auto-correlation, weighted over the path length distribution $P(s)$. For this reason, as opposite to the single-scattering regime, the overall autocorrelation function will not be a single exponential function.

The previous expression, together with an assumption about the type of dynamics encoded in the mean square displacement $\langle \Delta r^2(\tau) \rangle$, permits to quantify the scatterers dynamics. For the case of biological tissues, the dynamic particles are typically the red blood cells (RBC). In this case, it was showed with experiments and simulations that the mean squared displacement is well described by Brownian motion, for which $\langle \Delta r^2(\tau) \rangle = 6D_B\tau$, where D_B [cm^2/s] is the Brownian diffusion coefficient of the scatterers. In this case, the product αD_B is typically called blood flow index (BFI) [1,51].

2.3.3. Correlation diffusion equation

In the previous section, I have outlined a direct derivation of the electric-field auto-correlation function in the multiple scattering regime, see Eq. (2-17). By comparison with the experimental data, this enables the estimation of the sample dynamics. However, the reader might note that the formula contains an integral operation, which might not be simple to evaluate for complex geometries or heterogeneous samples. To overcome this difficulty, Ackermann *et al.* proposed a different theoretical approach, namely the correlation transport equation (CTE) [143]. In the framework of correlation transport, the electric-field auto-correlation can be treated similarly to the radiance (introduced in Section 2.1) [46,142,143]. In particular, we might interpret the field auto-correlation as a wave that propagates in the turbid medium. With respect to the “classical” light transport, in addition to the absorption and scattering events, one needs also to include the *dynamic scattering* events. As for the case of the RTE, with few assumptions it

is possible to derive from the CTE a correlation diffusion equation (CDE), which I report here [1,46,142]:

$$\begin{aligned} \left(\nabla \cdot (D(\mathbf{r})\nabla) - v\mu_a(\mathbf{r}) - \frac{1}{3}v\mu'_s k_0^2 \alpha < \Delta r^2(\tau) > \right) G_1(\mathbf{r}, \tau) \\ = -vS(\mathbf{r}), \end{aligned} \quad (2-18)$$

In which $D(\mathbf{r})$ is the photon diffusion coefficient, k_0 is the wavenumber in the medium, α is the fraction of moving scatterers, and $S(\mathbf{r})$ is the light source term. In Eq. (2-18), compared to the classical PDE, one might note that there is a third term which accounts for the *dynamic scattering* events. Let me note that the CDE has been derived assuming a CW light source, for this reason there is no temporal derivative term. Looking at the equation, we might see that the second and third term are very similar. For this reason, it is possible to interpret the term $\mu_a(\mathbf{r}) - \frac{1}{3}\mu'_s k_0^2 \alpha < \Delta r^2(\tau) >$ as an *effective absorption coefficient*. Thus, since also the boundary conditions are equivalent, it is possible to exploit the solutions of the PDE for solving the CDE [1,46,142].

Solution for a semi-infinite homogeneous medium

Here, as an example, I will report the CDE solution for the case of a semi-infinite homogeneous medium (with respect to optical and dynamical properties). By using the corresponding solution of the PDE, replacing μ_a with the effective absorption coefficient, one obtains [1,141]:

$$G_1(z, \tau) = \frac{v}{4\pi D} \left(\frac{e^{-K(\tau)r_1}}{r_1} - \frac{e^{-K(\tau)r_b}}{r_b} \right), \quad (2-19)$$

In which z is the depth coordinate, and the three parameters $K(\tau)$, r_1 and r_b are defined as following:

$$\begin{cases} K(\tau) = \sqrt{\frac{v}{D} \left(\mu_a + \frac{1}{3}k_0^2 \mu'_s \alpha < \Delta r^2(\tau) > \right)} \\ r_1 = \sqrt{(z - l^*)^2 + \rho^2} \\ r_b = \sqrt{(z + 2z_b + l^*)^2 + \rho^2} \end{cases}. \quad (2-20)$$

In Eq. (2-20), ρ is the source-detector separation and z_b is a boundary term (tabulated in Ref. [1]). Thus, for this geometry the electric-field auto-correlation has a simple analytical expression which depends only on the dynamical and optical properties of the sample.

In conclusion, in this section I showed two alternative theoretical approaches (direct method and CDE) for computing the electric-field auto-correlation function. Let me note that both methods can be useful for interpreting and/or analysing DCS data. In the next section, I will focus on the theory of TD-DCS, which was partially developed in this thesis work.

2.4. Time-domain DCS

In this section I will present the theory of TD-DCS. First, I will consider the case of an ideal system (i.e., perfect temporal resolution). Then, I will propose how to include in the model the effect of the instrument response function (IRF) [144]¹.

2.4.1. Ideal TD-DCS experiment

As seen in section 1.4.1, TD-DCS makes use of a pulsed laser to measure the path length resolved speckle intensity autocorrelation. Here, I will start by presenting the theory of an ideal TD-DCS experiment (i.e., perfect temporal resolution and temporal coherence).

In an ideal TD-DCS experiment, the photon path length s (or equivalently its time-of-flight $t = s/v$) can be measured with infinite accuracy. This corresponds to the case of a δ -like instrument response function (IRF). As we have seen in Section 2.3.2, the electric-field auto-correlation for a single path length, denoted as $g_1(\tau, s)$, can be expressed as an exponential function [70,78,79]:

$$g_1(\tau, s) = \exp(-2k_0^2 \mu'_s s \alpha D_B \tau), \quad (2-21)$$

¹ Article #1 in the list of Publications.

in which I considered the case of scatterers having Brownian dynamics (for which $\langle \Delta r^2(\tau) \rangle = 6D_b\tau$). This expression holds only when the photons within a very narrow path-length/temporal window are measured. I will refer to this case as the *narrow gate* regime, which was reported in Refs. [70,78,90,145].

In order to increase the signal-to-noise ratio (SNR), Pagliazzi *et al.* [79] proposed to measure the speckle fluctuations of photons over a certain temporal/path-length window $s \in [s_{in}, s_{fin}]$, where s_{in} and s_{fin} denote the limits of the considered time gate. I will refer to this acquisition method as the *broad gate* regime. In this regime, photons having a certain distribution of path lengths, thus having different decay rates, contribute to the auto-correlation decay rate. In this regime, Eq. (2-21) has a limited accuracy. A more accurate expression can be obtained by averaging the single path auto-correlation $g_1(\tau, s)$ over the considered path length interval $[s_{in}, s_{fin}]$, as proposed in Refs. [79,80]:

$$g_1(\tau) = \int_{s_{in}}^{s_{fin}} P(s) g_1(\tau, s) ds. \quad (2-22)$$

Eq. (2-21) shows that when photons having different path lengths are measured together, the overall field auto-correlation will not have a single exponential decay. Let me highlight that this regime is intermediate between the narrow gate regime, where photons having a single path length are measured, and an *ungated acquisition* scheme, where all the possible photon path lengths are measured (similarly to classical DCS) [79].

Up to now, I considered the case of an ideal system, thus having a δ -like IRF. In this case, the photon time-of-flight can be measured with perfect temporal resolution. In the next section, I will extend this theory to the case of *non-ideal* temporal resolution, by suitably modelling the effect of the IRF on the time-gated auto-correlation function.

2.4.2. Realistic TD-DCS experiment

Here I will develop the theory of TD-DCS for the case of a realistic experimental system [144]. Let me note that another research group

has proposed independently a similar model. However, it considers only the case of narrow temporal gates [89].

In a realistic TD-DCS system, the excitation pulses have a non-zero temporal duration, and also the photodetector has a certain temporal response. Also, the optical fibers and the acquisition electronics might degrade the system temporal response. These effects can be described synthetically by the IRF, which describes the overall temporal resolution of the system. To include the IRF in the model, we can interpret the IRF as a *probability distribution*. In the ideal case, the photon path lengths s can be measured with perfect accuracy. However, in a system with non-ideal temporal response, a photon having travelled an *ideal* path length s might be assigned due to the IRF to different path length s' , which I will call *real* path length. For this reason, we can interpret the IRF as a measure of the statistical discrepancy between the ideal and the real photon path lengths (s and s' respectively), or equivalently time-of-flights.

Formally, I will interpret the IRF as the *conditional probability* that a photon having an ideal path length s is assigned to a real path length between $s' \div s' + ds'$:

$$P(s' | s) = IRF(s' - s)ds' \quad (2-23)$$

In Eq. (2-23), I assumed the system to be linear and time-invariant. In this case, the conditional probability depends only on the path lengths *difference*, and not on their absolute values. A method for characterizing time-variant diffuse optical systems has been proposed recently [146]. Following this approach, I can express the elementary contribution $dg_1(\tau)$ to the overall autocorrelation as:

$$\begin{aligned} dg_1(\tau) &= P(s' \cap s)g_1(s, \tau)ds ds' = \\ &= P(s)IRF(s' - s)g_1(s, \tau)ds ds', \end{aligned} \quad (2-24)$$

where $P(s' \cap s)$ is the (joint) probability of measuring a photon with an ideal path length between $s \div s + ds$ and a real path length between $s' \div s' + ds'$. In Eq. (2-23), I exploited the definition of conditional probability $P(A \cap B) = P(A|B)P(B)$, and used Eq. (2-23) for $P(s' | s)$.

To obtain the overall auto-correlation function $g_1(\tau)$, we need to integrate the elementary contributions $dg_1(\tau)$ over the range of possible path lengths s and s' . In the general case, we measure the autocorrelation over a certain path length/temporal interval $[s_{in}, s_{fin}]$. It is important to note that, in practice, the photons are selected (i.e., gated) according to their real path length s' . For this reason, we have to impose that the real path length belongs to the given gate, thus $s' \in [s_{in}, s_{fin}]$. On the other hand, in principle there are no constraints on the real path length s , since it cannot be measured directly, thus $s \in [0, +\infty]$. Based on these considerations, the final expression of the auto-correlation function becomes:

$$\begin{aligned} g_1(\tau) &= \int_0^{+\infty} ds \int_{s_{in}}^{s_{fin}} ds' dg_1(\tau) \\ &= \int_0^{+\infty} ds \int_{s_{in}}^{s_{fin}} ds' P(s)IRF(s' - s)g_1(s, \tau). \end{aligned} \quad (2-25)$$

We might see that the final $g_1(\tau)$ is a complex combination of $P(s)$, IRF, and the single path length autocorrelation $g_1(s, \tau)$, not easily interpretable. In order to gain physical insight, let me recast Eq. (2-23) as follows:

$$g_1(\tau) = \int_0^{+\infty} EGF(s)P(s)g_1(s, \tau) ds, \quad (2-26)$$

Where the function $EGF(s)$, which I called *effective gate function* (EGF), is defined as:

$$EGF(s) = \int_{s_{in}}^{s_{fin}} IRF(s' - s) ds'. \quad (2-27)$$

Thus, the EGF is readily obtainable from the IRF by a simple integration over the considered gate interval. Comparing Eq. (2-23) with Eq. (2-23), we might see that in the ideal case only the (ideal) path lengths which belong to the chosen gate $[s_{in}, s_{fin}]$ contribute to the auto-correlation function. On the other hand, in the real case where the IRF is present, also path lengths outside the chosen gate contribute to $g_1(\tau)$. Thus, the EGF can be seen as a metric of the overall system

performance, in particular regarding the path length/temporal selectivity, for the given IRF and gate configuration.

In Figure 2-4, I report as an example the EGF of two temporal gates (for a typical IRF shape). As can be seen, the EGF have tails outside the ideal gate region, which indicate that path lengths outside the desired range are collected and contribute to the measured autocorrelation.

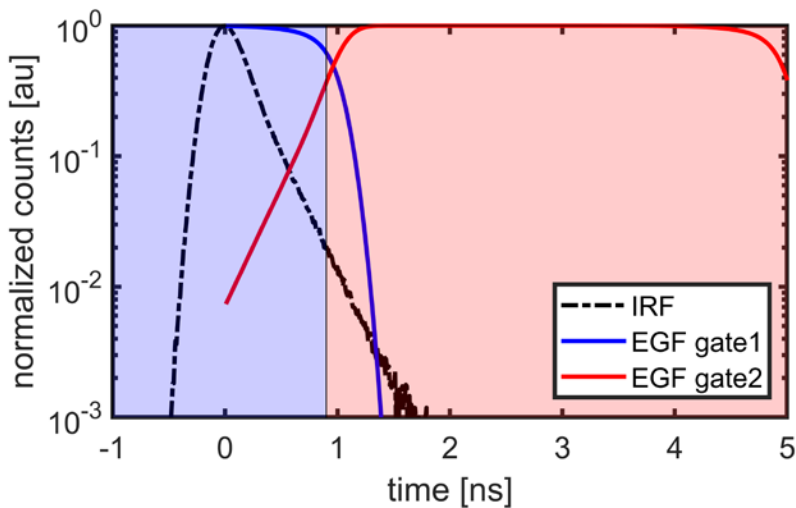


Figure 2-4: Example of effective gate function (EGF). The black line is the instrument response function (IRF). The shaded blue and red regions denote the (ideal) gate regions (an early and a late gate). The blue and red lines are the corresponding EGF, which measure which path lengths are actually measured, contributing to the measurement. Figure adapted from Ref. [144].

After having introduced the general model, I will discuss three particular cases: ideal system (δ -like IRF), narrow gates, and ungated acquisition.

Ideal system

For the case of an *ideal system*, the IRF is a Dirac δ : $IRF(s' - s) = \delta(s' - s)$. If we insert this expression in Eq. (2-23), we obtain:

$$\begin{aligned}
 EGF_{ideal}(s) &= \int_{s_{in}}^{s_{fin}} \delta(s' - s) ds' = \\
 &= 1 \text{ for } s \in [s_{in}, s_{fin}], 0 \text{ otherwise.}
 \end{aligned} \tag{2-28}$$

By inserting this result in Eq. (2-23), we obtain that the autocorrelation becomes identical to the ideal system case [see Eq. (2-23)].

Narrow gates

In the *narrow gate* regime, the temporal gate is a very narrow rectangular function centred around a certain path length s_0 . Thus, we might write $s' \in [s_0, s_0 + \delta s]$. In this case we obtain:

$$EGF^{narrow}(s) = \int_{s_0}^{s_0 + \delta s} IRF(s' - s) ds' \cong IRF(s_0 - s) \delta s \tag{2-29}$$

Where I used the mean value theorem and took the limit $\delta s \rightarrow 0$, which corresponds to an infinitely narrow gate. Thus, in this case the EGF is a time-reversed and shifted version of the IRF. By inserting Eq. (2-23) in Eq. (2-23), and neglecting the constant term δs , I obtain:

$$g_1^{narrow}(\tau) = \int_0^{+\infty} IRF(s_0 - s) P(s) g_1(s, \tau) ds, \tag{2-30}$$

Which is equivalent to the expression reported in Ref. [89]. It is interesting to note that, even for the case of very narrow gates, the IRF distorts the shape of the auto-correlation function.

Ungated acquisition

As a final case, I will consider the limit of ungated acquisition. In this case, the time gate is infinitely wide, thus $s' \in [-\infty, +\infty]$. By considering this integration extremes, by exploiting the fact that the IRF is normalized to area, we obtain:

$$EGF^{ungated}(s) = \int_{-\infty}^{+\infty} IRF(s' - s) ds' = 1 \tag{2-31}$$

Thus, by inserting this expression in (2-23), we obtain the same expression of Eq. (2-32). Thus, in this regime the IRF does not significantly distort the auto-correlation function, provided that the gate widely encloses all the signals involved ($P(s)$ and IRF).

In summary, in this section I proposed a novel model for predicting the effects of the IRF in TD-DCS experiments. The model was based on the EGF, a function, derived from the IRF and the considered temporal gate. Also, I provided a physical interpretation of the model and I discussed three particular cases. The model was effectively applied to interpret phantom and *in vivo* data, leading to better quantification, as described in the following Chapters.

Chapter 3: Experimental setup

In this chapter, I will introduce the experimental setup which I developed during this thesis work. First, I will summarize the general scheme of the experimental system. Then, I will move to the individual building blocks (e.g., laser sources, detectors, acquisition modules), which I compared and selected with the aim of optimizing the performance of the overall system.

3.1. General scheme

One large part of this thesis work was devoted to the development and characterization of the experimental setup for TD-DCS (introduced in Section 1.4.1). In this section, I will summarize the general scheme of the setup, with its main building blocks. The system has been designed in a *modular* way, which enabled to choose the individual components (laser sources, detectors, acquisition modules) according to the desired specifications (e.g., spectral range, temporal coherence, optical power, temporal resolution, number of channels etc) and application. Figure 3-1 shows the general scheme of the developed setup.

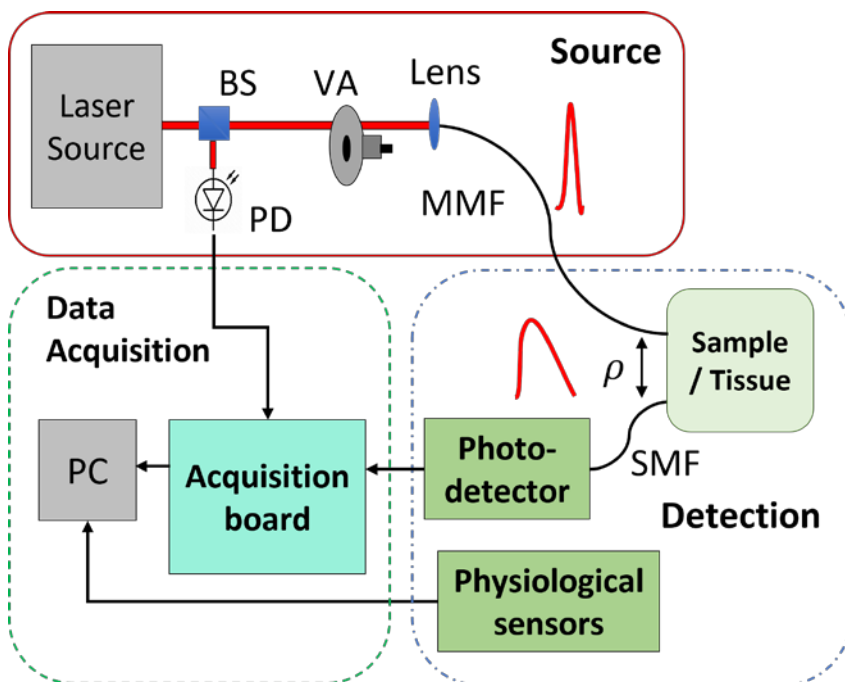


Figure 3-1: Experimental setup scheme. The scheme was conceptually divided in three parts: “source” (red box), “detection” (blue dash-dotted box), and “data acquisition” (green dashed box). The thick red lines denote free-space optical propagation, the black curved lines denote optical fibers, and the black straight lines denote electrical connection. In the figure BS: beam splitter; PD: photodiode; VA: variable attenuator; MMF: multi-mode fiber; ρ : source-detector separation; SMF: single-mode fiber; PC: computer with software correlator.

As shown in Figure 3-1, a laser source emits light pulses, at a certain wavelength λ , which are attenuated and coupled to a graded index multi-mode fiber. By using a beam splitter, a small part ($\sim 5\%$) of the excitation light is taken from the beam and delivered to a fast photodiode (OCF-401, Becker & Hickl, Berlin, Germany), for generating a synchronization (sync) signal for the acquisition electronics. The light from the multi-mode fiber ($100 \mu\text{m}$ core) is then delivered to the sample/tissue under study. In the case of *in vivo* measurements, the optical power was set below the ANSI safety levels ($< 2 \text{ mW}/\text{mm}^2$). The diffusely reflected light is collected, at a certain source-detector separation ρ ($\sim 1 \text{ cm}$), with a single-mode fiber (780 HP, Nufern, Connecticut USA). The re-collected light is then coupled to a single-photon detector, and the corresponding photon arrival times are stored in a PC by means of an acquisition board. The PC is equipped with a custom software for computing the (time-gated) autocorrelations [$g_2(\tau)$] and DTOF curves with a post-processing software. For the case of *in vivo* measurements, in certain cases I used additional physiological sensors (e.g., electrocardiogram, breath monitor, blood pulsation), which were synchronized with the optical data.

In the following sections, I will present in detail the individual building blocks, in particular:

- Laser sources (Section 3.2)
- Single-photon detectors (Section 3.3)
- Data acquisition and post-processing (Section 3.4)
- Physiological sensors (Section 3.5)

As mentioned before, each building block was assessed in terms of performance characteristics and other “practical” considerations, such as complexity, physical dimensions, ease of integration etc.

3.2. Laser sources

As we have seen in the previous Chapters, the laser source for a TD-DCS experiment needs to be pulsed yet temporally coherent. Regarding the temporal duration, the light pulse needs to be much

shorter than the DTOF duration (which is few hundreds of picoseconds). About the coherence properties, as mentioned in Chapter 1, the emission bandwidth needs to be much shorter than the medium bandwidth (which is a fraction of nm for typical samples). For this reason, one needs to carefully choose the “*pulsing*” method to exploit. For instance, a femtosecond laser might not have the sufficient coherence length to obtain the desired speckle contrast.

During this thesis work, I have tested several types of pulsed lasers, which can be generally divided in:

- i. Actively mode-locked laser
- ii. Spectrally filtered femtosecond laser
- iii. Temporally gated continuous-wave laser.

The first approach, **active mode-locking**, the light pulse is formed by periodically modulating the losses within the optical resonator, by means of an acousto-optic (AO) modulator [147]. In this way, light is generated only when the losses are lower than the gain of the active medium. A periodic train of light pulses will be emitted by the laser, with a temporal duration which can be tuned by acting on the AO modulation power. This enables to phase-lock the cavity modes, obtaining pulses with durations between tens *ps* to ~ 1 *ns* and good coherence length².

The second approach is based on a **femtosecond laser**, which is **spectrally filtered** after the optical resonator. The final pulse duration will strongly depend on the selected bandwidth [148,149]. With very narrow filters, the obtained laser pulse can have durations up to tens or hundreds of *ps*. However, with respect to active mode locking, the temporal duration is difficult to tune.

The third approach is based on using a **CW laser**, which is **temporally gated** outside the optical resonator [150,151]. This method enables to obtain tuneable pulse durations (down to the *ps* level), however it

² For active mode locking, the theoretical pulse duration is given by $\tau_p \sim \left(\frac{g_0}{\delta_m}\right)^{1/4} \left(\frac{1}{\omega_m \Delta\omega_0}\right)^{1/2}$, where g_0 is the gain of the active medium, δ_m is the modulation efficiency, ω_m is the modulation frequency, and $\Delta\omega_0$ is the gain bandwidth [147,152].

requires a very high modulation efficiency, in order to cut undesired tails in the temporal profile of the output pulse.

Let me note that, while the first method does not need an amplification stage, the second and the third generally need an optical amplifier to obtain a sufficient laser power. This might distort the spectral/temporal properties of the output pulse, which might lead to instabilities. In addition, the temporal tunability obtainable with active mode-locking is particularly useful for optimizing the laser pulse for the specific application. For this reason, in this thesis work I used a laser belonging to the first category, specifically a custom-made active mode-locking *Ti:Sapphire* laser. In the next section, I will describe in some detail this specific laser source.

3.2.1. Ti:Sapphire laser

Here I will present the Ti:Sapphire laser source which I used extensively in this thesis work, developed in Ref. [152,153], see Figure 3-2. A frequency-doubled Nd:YAG CW laser, 4 W max power (Millenia V, Spectra Physics, USA), pumps a Ti:Sapphire crystal placed in the centre of a Z-folded optical resonator. The resonator is a modified version of a commercial CW system (3900, Spectra Physics, USA).

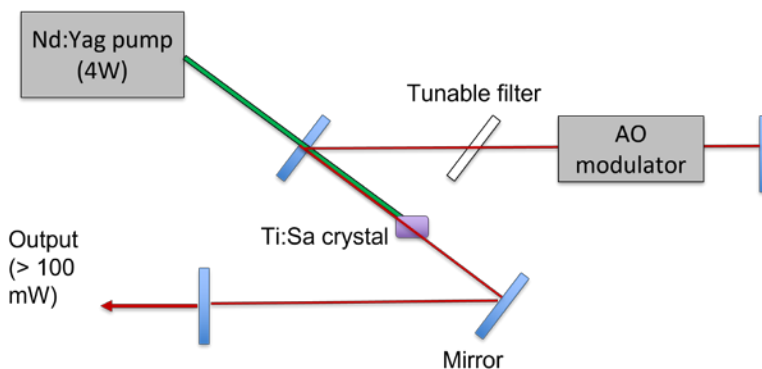


Figure 3-2: Scheme of the Ti:Sapphire laser used in this work. Light from a Nd:YAG CW laser is delivered to a Ti:Sapphire crystal, in a Z-shaped optical resonator. A tuneable filter is used for wavelength selection. An acousto-optic (AO) modulator (100 MHz modulating frequency) is used for the active mode-locking. The wavelength range is 700-850 nm for typical mirror set, 900-1050 nm for the IR mirror set. The average power is above 100 mW, while the pulse duration is tuneable between 50 ps and 1 ns.

The mirrors of the cavity are designed to have maximum reflectivity in a certain wavelength range i.e., 700-850 nm for the typical mirrors set, 900-1050 nm for an IR-optimized mirror set. The left end mirror has a ~2% optical transmission to couple the generated light (red line in the Figure) outside the cavity. A tuneable Lyot filter is placed in the cavity for a fine selection of the wavelength.

For the pulse generation, an acousto-optic (AO) modulator is placed in the cavity, see Figure 3-2. The AO modulator is tuneable in frequency, around 100 MHz, power - also called *carrier level* - and angle (to select the desired diffraction order). The AO modulation efficiency can be monitored by measuring the RF power reflected by the crystal. In order to optimize the pulse, first the reflected RF power should be minimized by tuning the AO modulation frequency. Then, for tuning the pulse duration it is necessary to micro-metrically change the cavity length, by translating the totally reflective end mirror. The minimum pulse duration is obtained when the cavity length (more precisely the repetition frequency) is exactly matched to the AO modulation frequency, this can be obtained by maximizing the output laser power. Let me note that the minimum pulse duration is determined also by the chosen RF power level. Higher modulation powers, so-called carrier levels, correspond to shorter pulse durations, but also to lower laser power.

Power performance

Depending on the selected wavelength and with the present pump laser (4 W power), the average power generally exceeds 200 mW in the CW regime, and 100 mW in the pulsed regime. By acting of the carrier level and the cavity length, the pulse duration can be tuned between 50 ps and 1 ns full width at half-maximum (FWHM). In Figure 3-3, I show the laser power as a function of the wavelength, for the typically used mirror set (700-850 nm), in the CW regime.

As seen in Figure 3-3, except around 700-750 nm, the CW laser power is well above 100 mW. In the pulsed regime, the average power depends strongly on the laser configuration (e.g., the carrier level), but typically is around one half of the value obtained in CW. As we will see in the next chapter, the quality of the data e.g., signal-to-noise ratio (SNR), depends both on the pulse duration and stability (which affects the coherence parameter β) and the average optical power. Thus,

there exists a *trade-off* between pulse duration, coherence, and power, that needs to be tackled for reaching the optimal SNR. For this laser source, the optimal pulse duration in TD-DCS experiments is between 150 and 300 ps (FWHM).

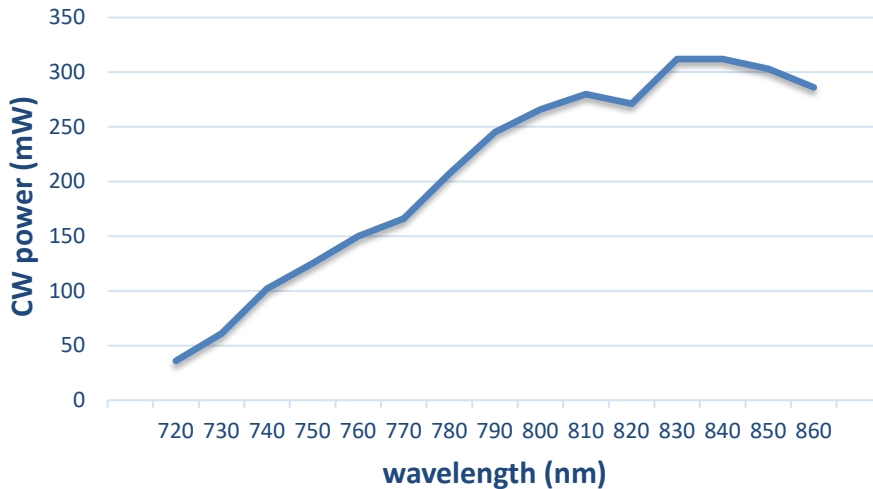


Figure 3-3: Laser power as a function of wavelength, for the typical mirror set (700-850 nm), CW regime. In the pulsed regime the average power is roughly halved (but it depends strongly on the laser configuration).

In the next two sections, I will present the photodetectors, acquisition boards and post-processing software I used in the experiments.

3.3. Single-photon detectors

In this section, I will present briefly the single-photon detectors used in this thesis work. Generally, the optimal TD-DCS detector should have high temporal resolution, high detection efficiency, and low noise and after-pulsing. In particular, the detector response should be comparable or better than the pulse duration (ideally < 100 ps) to not degrade the overall temporal performance (i.e., the IRF). The detection efficiency is critical to TD-DCS since we are constrained to single-mode detection, thus a high quantum efficiency is desired. For the same reason, the background noise, also called dark counts, should be very small (ideally < 1 kcps), to maintain a high dynamic range. The after-pulsing i.e., the generation of secondary (undesired) photo-counts, as

a consequence of a detected photon, needs also to be limited, since it affects the shape of the autocorrelations at early τ .

Based on the above considerations, in this thesis work I have used the following photodetectors:

1. Single-photon avalanche diode (SPAD)
2. InGaAs photomultiplier (PMT)
3. Single-photon superconducting nanowire detector (SPSND)

The **SPAD detector** (PDM, Micro Photon Devices, Italy) is a silicon-based detector with high quantum efficiency (for $\lambda < 900$ nm). When a photon is detected, a photoelectron is generated, yielding an electronic avalanche, that can be read by suitable electronics. The output signal marks with high resolution (~ 50 ps) the photon arrival time. The detector dead time (the time it takes to be ready to measure another photon) is few tens of ns [18]. The detection fiber is coupled with the active area of the detector ($\varnothing = 100 \mu m$) by means of a microscope objective mounted on a positioning stage. In this work, I used this photodetector for the measurements in the wavelength region around ~ 800 nm.

For the measurements at longer wavelengths (~ 1000 nm), I used the **InGaAs photomultiplier** (H10330-25 Hamamatsu Photonics, Japan), which was fiber connected. Being based on III-V semiconductors, it has a lower energy gap, which extends its sensitivity more in the NIR. The quantum efficiency in this spectral range is $\sim 2\%$ (higher than the SPAD in this spectral region), and the temporal resolution is ~ 400 ps (being limited by the spread in transit times) [154].

The **SPSND detector** (EOS, Single Quantum, Netherlands), was used to evaluate its suitability for TD-DCS. The detectors are based on superconducting nanowires kept at cryogenic temperatures (< 3 K). The detection mechanism is completely different compared to the other two detectors. The nanowire is biased with a current slightly lower than the nanowire's critical current. When a photon is absorbed, the nanowire becomes resistive, thus a small voltage drop is created, which can be read after electronic amplification. After few ns the nanowire recovers

its superconducting state, thus it is ready to measure another photon. The SPSND has very high quantum efficiency (up to 90%), temporal resolution (<20 ps), and very limited background noise (few tens of cps) [155,156]. One drawback is its high complexity, due to the need of a cryostat and a compressor for its operation. The detection system I used had 4 fiber-connected channels, 2 optimized for ~ 800 nm and 2 for ~ 1000 nm.

All three detectors have SMA electronic outputs with are delivered to the data acquisition board (see next Section).

3.4. Data acquisition and processing

In this section, I will present the acquisition boards and correlation algorithm I used in the experiments.

3.4.1. Acquisition boards

The acquisition boards I used in the experiments are based on time-correlated single photon counting (TCSPC). In our technique, the acquisition board needs to measure two quantities:

1. The photon **time-of-flight**, with $\sim ps$ resolution (sometimes called micro-time). The photon time-of-flight is measured, similarly to TD-NIRS, by exploiting two types of channels:
 - i. The *signal channel(s)*, which measure the arrival time of the detected photons, from the output of the single-photon detector(s), see Section 3.3.
 - ii. The *sync channel*, which measures the times at which the laser pulse is emitted, from the output of the photodiode, see Section 3.1.

The time-of-flight is then measured as the time difference between the photon arrival time (signal channel) and the time of the nearest pulse emission (sync channel).

2. The photon **absolute arrival time**, with $\sim ns$ resolution (sometimes called macro-time), computed by identifying the laser repetitions for which a photon is detected (signal channel).

During the experiment, the TCSPC board acquires, for every detected photon, both the time-of-flight and the arrival time (together called timestamps) and store it in a binary file, which can then be post-processed for computing the DTOF and autocorrelations (see next sub-section).

In this thesis, I have used the following TCSPC boards, depending on the number of required channels:

1. TimeHarp 260 pico (PicoQuant, Germany), having one signal and one sync channel, 25 ps temporal bin width, max count-rate 40 Mcps (25 ns dead time).
2. Time Tagger Ultra (Swabian instruments, Germany), having 7 signal channels and one sync channel, tuneable bin width (10 ps jitter), max count-rate 35 Mcps (2 ns dead time).

Both the TCSPC board have SMA electrical inputs, and are connected with the PC with a PCIe port or USB (respectively). The detected timestamps are stored continuously in a binary-file, which is then post-processed.

3.4.2. Post-processing and fitting

The post-processing software I used, developed by colleagues in *Python* (see Ref. [157]), is able to process the acquired time stamps to compute the following quantities:

- Detected intensity (counts)
- Time-of-flight histogram (DTOF)
- Time-gated autocorrelations $[g_2(\tau)]$.

All the three quantities can be obtained with a flexible temporal resolution (e.g., 1-10 Hz sampling rate). For the autocorrelations, the

computing time is approximately 30 minutes for 100 M acquired photons, while is relatively shorter for the other two quantities.

For the correlation computation, we used the method proposed by Wahl *et al.* [158]. In this algorithm, the autocorrelation is computed directly from the photon arrival times (timestamps), instead of computing it from the measured intensity as in the multi-tau algorithm [159]. For the typical count rates obtained in our experiments (<1 Mcps), this timestamps processing is much faster compared to the classical method (i.e., bin and correlate the photons) [158,160].

Briefly, the used algorithm computes the autocorrelation by shifting the photon arrival time array by the given τ , and then counting the number of photons pairs with matching times. For increasing values of τ , the computation is performed with lower temporal resolutions, by rounding the arrival times array to a broader temporal resolution. This makes the computation at long τ values much faster, compared to the classical linear autocorrelation (e.g., FFT based).

In this algorithm, the τ array has the following form:

$$\tau_j = \begin{cases} \tau_{min} & \text{for } j = 1 \\ \tau_{j-1} + 2^{int(\frac{j-1}{B})} & \text{for } j > 1 \end{cases} \quad (3-1)$$

In the equation, τ_{min} is the minimum lag time. While B, the so-called cascade length, determines the number of linear steps of τ before the arrival times resolution is doubled, and j (which is the index for τ) goes from 1 to $N_{casc}B$ (with N_{casc} number of linear cascades). For our application, I typically set the parameters to $\tau_{min} = 10$ ns, $B = 6$, and $N_{casc} = 25$. With these parameters, the τ array has an approximately logarithmic increase from 10 ns to ~ 0.2 s.

In order to compute the time-gated autocorrelation, the algorithm is performed by considering the photons with time-of-flight belonging to a certain temporal window (e.g., from 1 ns to 2 ns). Typically, multiple time gates are considered, with position and widths which are determined in post-processing depending on the shape of the DTOF and the signal level.

The second level analysis, in particular the fitting of the autocorrelation functions for retrieving the BFI, was implemented in *MATLAB* using the models presented in Sections 2.3 and 2.4 (for ungated and time-gated acquisition, respectively). In all cases, the fit was performed using the Nelder-Mead simplex optimization method (*MATLAB* “fminsearch” function).

3.5. Physiological sensors

In this last section, I will briefly describe how I integrated additional physiological sensors in the setup. The sensors used (produced by Thought Technology Ltd, Canada) were the following:

- Electrocardiogram (EKG)
- Respiration rate
- Blood volume pulse (BVP)

The EKG sensor is composed of 3 electrodes (+/- electrodes placed below the shoulder blade of the subject, ground electrode placed below the navel). The Respiration rate sensor is composed of a flexible band placed around the chest of the subject. Finally, the BVP sensor (similar to a pulse oximeter) is placed on the index fingertip of the subject. The data from these sensors were acquired with a single acquisition board (Flex Comp Infinity, Thought Technology Ltd, Canada), and suitably synchronized with the TCSPC board, see Figure 3-4.

As shown in Figure 3-4, the synchronization of the optical signal with the other sensor was achieved by using an electronic trigger, generated by the PC every second, and delivered to both the devices. Let me note that, due to the different input impedance of the TCSPC board (50Ω) and the physiological sensors ($\sim 1 \text{ M}\Omega$), a buffer stage was used to avoid electronic reflections.

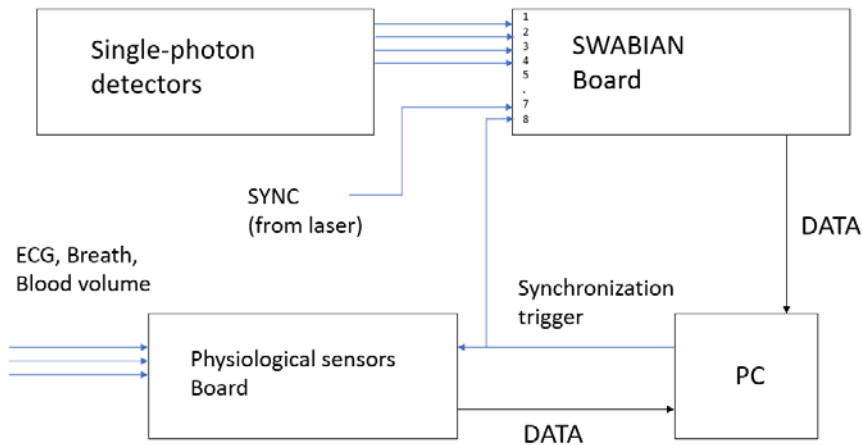


Figure 3-4: Integration of the physiological sensors in the experimental setup. The three sensors (electrocardiogram, respiration monitor, peripheral blood volume) were placed on the subject, and the data acquired with their acquisition board. In order to synchronize the optical data with the physiological sensors, an electronic TTL signal was generated by a PC and delivered to the two acquisition boards.

Summary and perspective

To summarize, in this Chapter I showed how I designed and developed an experimental setup for TD-DCS. The key components presented were laser sources, single-photon detectors, acquisition board and software, and physiological sensors. In the following, I will present the experimental results, starting with a system validation/characterization with tissue-mimicking phantoms (Chapter 4). Then, I will show how the system was exploited to observe and characterize an interesting physical effect, namely the temporal speckle (Chapter 5). Finally, the system was used for biomedical applications, performing several *in vivo* experiments on adult volunteers (Chapter 6).

Chapter 4: System characterization

In this chapter, I will characterize the developed TD-DCS system, with the help of tissue-mimicking phantom experiments. First, I will characterize the dependence of the coherence parameter (β) on the system (e.g., pulse duration) and sample (e.g., optical properties) configurations. Then, I will evaluate the accuracy of the developed theoretical model (IRF model) for retrieving the blood index (BFI). Finally, I will compare the performance of different laser sources and detectors and evaluate the feasibility of moving to longer wavelengths.

4.1. Characterizing the coherence parameter (β)

In this section, I will characterize the developed system, particularly in terms of the coherence parameter (β). This parameter, defined as the amplitude of the intensity autocorrelation $g_2(\tau)$, is crucial for TD-DCS experiments. In fact, it directly affects the signal-to-noise ratio of the measured auto-correlations, and thus the accuracy of the BFI measurement [141]. For the characterization, I carried out phantom experiments with the system presented in Chapter 3. In particular, I used the Ti:Sapphire laser source (see Section 3.2.1), the SPAD detector (see Section 3.3), and the Picoquant TCSPC board (see Section 3.4.1). The tissue-mimicking liquid phantoms were prepared using recipes from the literature [161]. Here I will describe the dependence of the coherence parameter (β) on the following parameters:

1. pulse duration (Section 4.1.1)
2. optical properties (Section 4.1.2)
3. gate width (Section 4.1.3).

4.1.1. Pulse duration effect

In this section, I will study the effect of the pulse duration on the measured β parameter. For simplicity, I will start by considering ungated acquisition (similarly to “classical” DCS). I prepared a liquid phantom by mixing 5% of Intralipid 20 (B. Braun Melsungen AG, Germany) and 95 % of distilled water, which corresponds to the nominal optical properties $\mu'_s = 10 \text{ cm}^{-1}$ and $\mu_a = 0.02 \text{ cm}^{-1}$ [161]. The laser wavelength was set to $\lambda = 785 \text{ nm}$, at which the absorption is almost entirely due to water, and the source-detector separation $\rho = 1.5 \text{ cm}$. The integration time was 10 s, for 30 repetitions (300 s in total). In Figure 4-1, I show the experimental results for five different laser pulse durations (FWHM, tuned by acting of the RF power of the acousto-optic modulator). Subpanel (a) shows the intensity autocorrelation $g_2(\tau)$, and (b) the electric-field auto-correlation $g_1(\tau)$ computed using the Siegert relation. In the subpanel (c) I show the measured β parameter, and in (d) the estimated Brownian diffusing coefficient (D_B) using the (CW) solution of the CDE (see Section 2.3.3).

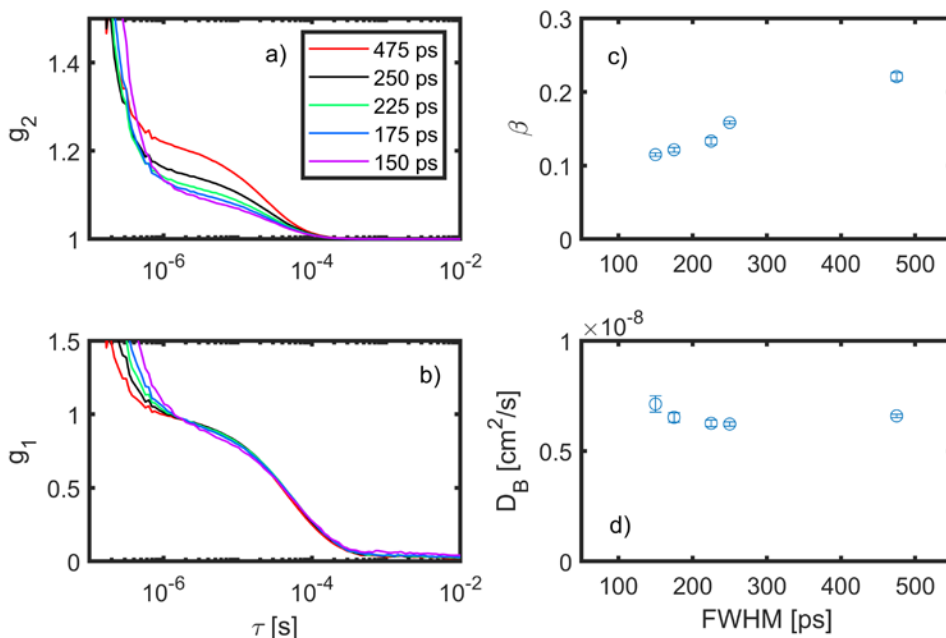


Figure 4-1: Liquid phantom results for ungated acquisition, for different IRF FWHM. The laser pulse duration was tuned by acting on the acousto-optic modulation power. Panels (a) and (b) show the intensity and electric-field auto-correlations [$g_2(\tau)$ and $g_1(\tau)$]. At very short lag times τ ($< 10^{-6}$ s) the spurious effect of the detector after-pulsing is visible, while the behaviour at longer τ is mainly determined by the dynamics of the sample. Panels (c) and (d) show the corresponding coherence parameter and brownian diffusion coefficient [β and D_B]. The error-bars denote standard deviations. Figure adapted from Ref. [144].

As shown in Figure 4-1, the amplitude of $g_2(\tau)$ increases for increasing pulse durations. This effect can be interpreted by an increase of the laser coherence length [23], which is expected to increase for longer pulse durations [162]. This dependence is more evident looking at the β parameter, which ranges from ~ 0.1 to > 0.2 , depending on the pulse duration (its theoretical value is 0.5 for infinite coherence length). Interestingly, the decay rate of $g_1(\tau)$, quantified by the coefficient D_B , is less dependent on the pulse duration. In particular, for large pulse durations (> 200 ps) is approximately constant, while for shorter ones a certain discrepancy appears. This might be an effect of the detector after-pulsing, or the breakdown of the Siegert relation [23,138].

4.1.2. Optical properties effect

In this section, I will study the dependence of the measured β parameter on the optical properties (i.e., absorption and reduced scattering coefficients). Also here, for simplicity, I restrict myself to ungated acquisition, while on the next section I will show the effect of temporal gating. In order to study the effect on the optical properties, I prepared two sets of liquid phantoms: i) Absorption variation: different values of absorption coefficient ($\mu_a = 0.02, 0.1, 0.2, 0.3 \text{ cm}^{-1}$), with fixed reduced scattering $\mu'_s = 10 \text{ cm}^{-1}$. ii) Scattering variation: different values of reduced scattering coefficient ($\mu'_s = 5, 7.5, 10 \text{ cm}^{-1}$), with fixed absorption $\mu_a = 0.1 \text{ cm}^{-1}$. In Figure 4-2 I show the result for absorption variations, while in Figure 4-3 for scattering variations. As before, the measurements were performed for five different pulse durations (IRF FWHM), always with $\lambda = 785 \text{ nm}$ and $\rho = 1.5 \text{ cm}$.

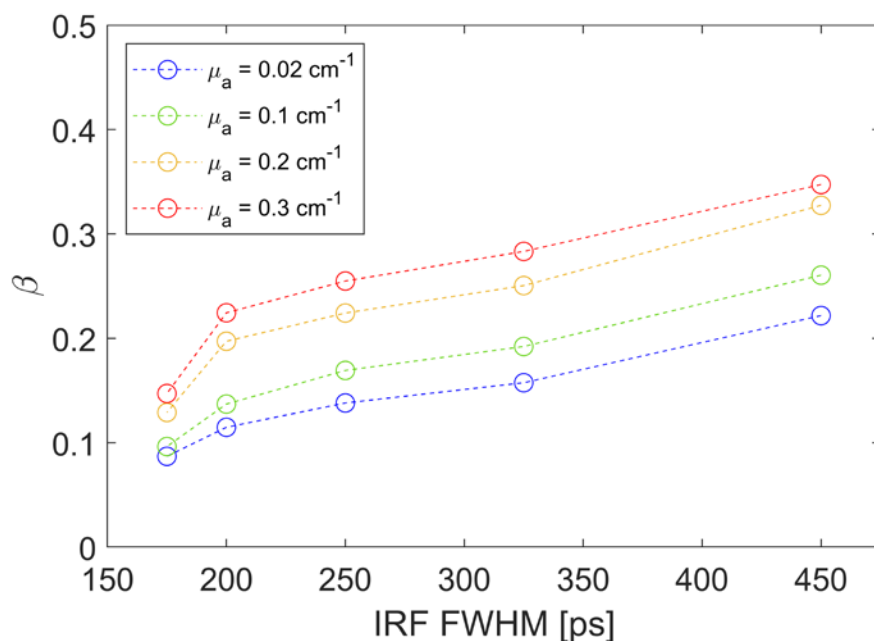


Figure 4-2: Dependence of the measured coherence parameter β (y axis) on the absorption coefficient. The experiments were performed for different pulse durations (IRF FWHM, x axis), in ungated acquisition. The samples are liquid phantoms with fixed reduced scattering ($\mu'_s = 10 \text{ cm}^{-1}$), and different absorptions (see legend).

As shown in Figure 4-2, the absorption coefficient plays an important role in the value of the β parameter. In particular, higher μ_a generally corresponds to higher coherence. This might be interpreted by the fact that the absorption modulates the tail of the path length distribution $P(s)$ (estimated by the theoretical reflectance). Thus, for a fixed pulse duration (i.e., coherence length), narrower $P(s)$ will increase the degree of interference of the detected photons [23].

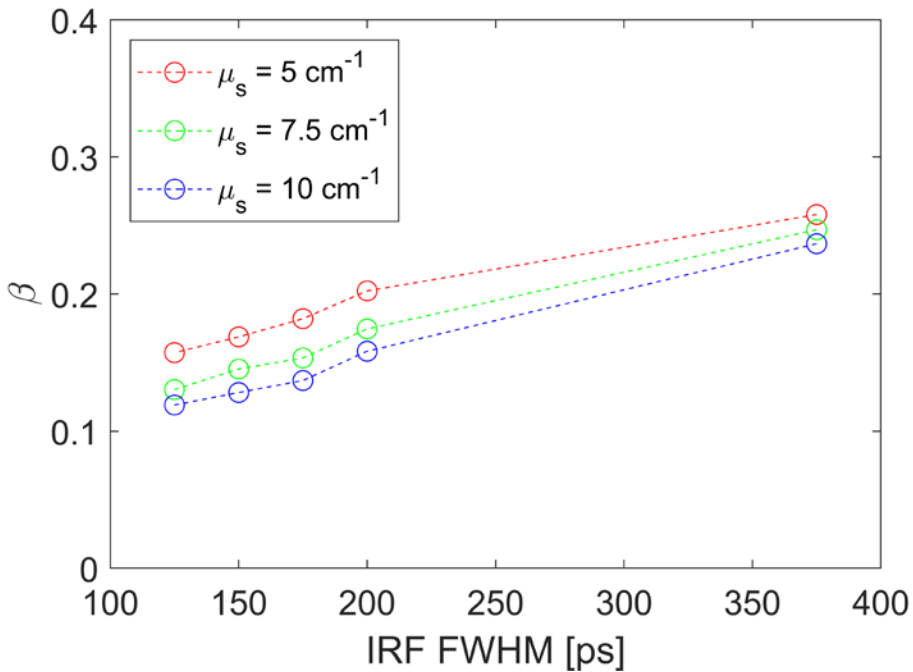


Figure 4-3: Dependence of the measured coherence parameter β (y axis) on the reduced scattering coefficient. The experiments were performed for different pulse durations (IRF FWHM, x axis), in ungated acquisition. The samples are liquid phantoms with fixed absorption ($\mu_a = 0.1 \text{ cm}^{-1}$), and different values of reduced scattering (see legend).

A similar effect is seen also for scattering variations (Figure 4-3). In this case, higher β is seen for lower reduced scattering coefficients. This agrees with the previous interpretation, since lower μ'_s correspond to narrower $P(s)$, since the photons are less temporally broadened by the sample (see Section 1.2.1). Thus, we might see that the β parameter strongly depends on the combination of pulse duration (FWHM) and

optical properties (more specifically the path length distribution). In the following, I will study the effect of the gate duration, which we will see is a key parameter to consider in TD-DCS experiments [163,164].

4.1.3. Gate width effect

In this section I will study the effect of the gate width of the β parameter. I have measured a liquid phantom, with nominal optical properties $\mu'_s = 10 \text{ cm}^{-1}$ and $\mu_a = 0.02 \text{ cm}^{-1}$, and set $\rho = 1.5 \text{ cm}$. As in the previous section, five different laser pulse durations (FWHM) were considered. For each FWHM, the time-gated autocorrelations $g_2(\tau)$ were measured for different gate widths i.e., 250, 500, 1000, 2000, 4000, 7000 ps. In all cases, the gate start was set at the peak of the DTOF curve. The maximum gate width was limited by the laser repetition rate [$100 \text{ MHz} = (10 \text{ ns})^{-1}$]. In Figure 4-4 I report the measured β parameter as a function of the gate width, for the different IRF FWHM considered.

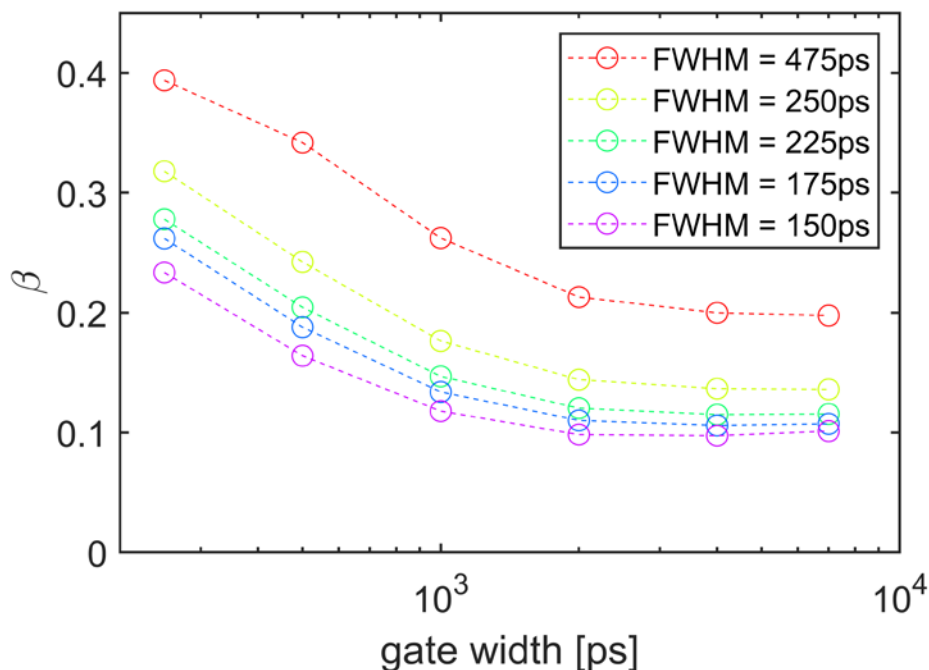


Figure 4-4: Measured β parameter as a function of gate duration (250, 500, 1000, 2000, 4000, 7000 ps), always starting at the DTOF peak. The measurements were performed for five different pulse durations (IRF FWHM, see legend). The x axis is in log scale for better readability.

In Figure 4-4, we might see that the β parameter strongly increases when the gate width is reduced. In particular, its value approximately doubles when moving from 7000 ps gate width (i.e., ungated acquisition) to 250 ps. Note that I did not consider smaller gate widths in order to keep the photon count to a sufficiently high value. The increase of the β parameter might be explained by the narrowing of the *effective* path length distribution induced by the temporal gating. In fact, when the photons are temporally gated, the probability of detecting two photons having a path lengths difference smaller than the laser coherence length increases [89,144]. On the other hand, as I noted before, smaller gate widths correspond to a smaller number of detected photons. Thus, it is necessary to carefully evaluate the gate duration for obtaining an optimal SNR [164,165].

To summarize, in this Section 4.1 I have shown that the experimental coherence parameter β depends on several quantities, both on the side of the system (pulse duration, gate duration) and the sample (optical properties). This characterization might give guidance to optimize the system parameters for obtaining the best performance with the given sample under study. In the next section, I will assess the theoretical models for retrieving accurately the blood flow index (BFI) from experimental data.

4.2. Characterizing the BFI accuracy: comparing theoretical models

In this Section, by means of phantom experiments, I will assess which is the most accurate theoretical model for extracting the BFI from the measured autocorrelations. The two theoretical models I will compare are the “ideal system” TD-DCS model (Sec 2.4.1), and the IRF-corrected model, which I proposed in Sec. 2.4.2. Let me note that I also compared the two models using Monte Carlo simulations (not shown here), for details see Ref. [144]³.

For the experiments, as in the previous section, I have prepared a homogeneous liquid phantom, with nominal optical properties

³ Article #1 in the List of publications.

$\mu'_s = 10 \text{ cm}^{-1}$, $\mu_a = 0.02 \text{ cm}^{-1}$. The source-detector separation was set to $\rho = 1.2 \text{ cm}$, and the wavelength $\lambda = 785 \text{ nm}$. The autocorrelations were measured with 20 s integration time, for 25 repetitions (for a total of 500 s of acquisition). The autocorrelations were computed for 5 temporal gates, with centre ranging from $t = 0 \text{ ns}$ to $t = 2 \text{ ns}$ (starting from the IRF peak). Each gate had 1 ns duration, each one 500 ps overlapped with the previous one (for increasing the signal-to-noise ratio).

In Figure 4-5, panel (a), I show the IRF and overall DTOF. In panel (b) I show, for two representative gates ($t = 0 \text{ ns}$, Early gate, and $t = 1.5 \text{ ns}$, Late gate), the measured autocorrelation (g_1), and the corresponding best-fits with the ideal model (dashed lines) and IRF-corrected model (continuous lines). In all cases, the fits were performed from $\tau = 10^{-6} \text{ s}$ to the lag τ where $g_1 = 0.5$, and then averaged across repetitions. In Figure 4-6(a), I show the corresponding BFI estimations, together with the reference BFI value (obtained with ungated analysis), while panel (b) shows the measured β parameter.

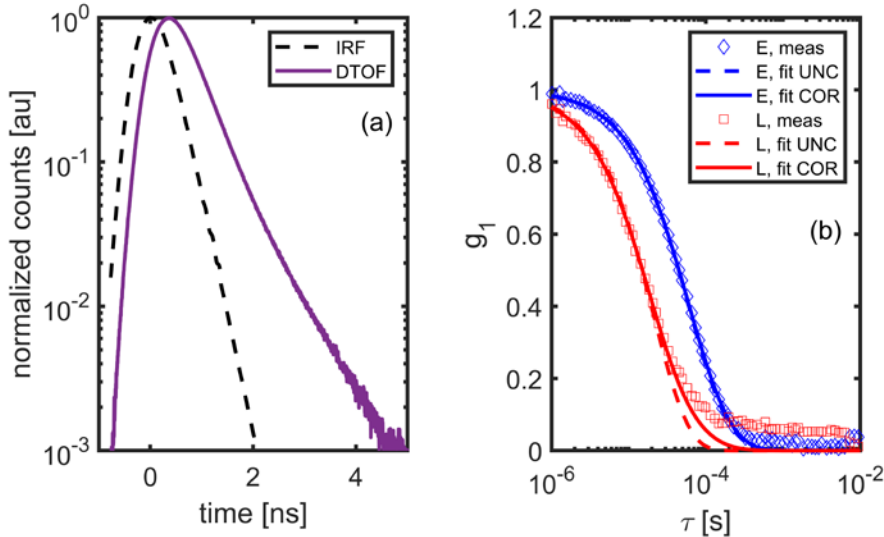


Figure 4-5: (a) IRF and DTOF from the phantom experiment. (b) Measured autocorrelations (g_1) for an early gate (E, blue diamonds) and a late gate (L, red squares). The gates were centred at $t = 0 \text{ ns}$ and $t = 1.5 \text{ ns}$ respectively. Dashed lines denote their best-fits with uncorrected model (UNC), while continuous lines the best-fits with the IRF-corrected model (COR).

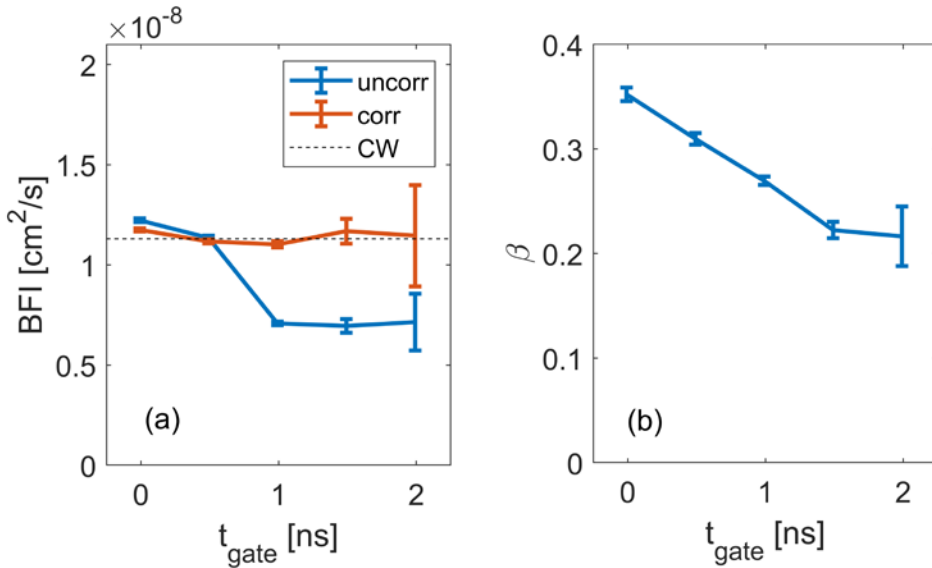


Figure 4-6: (a) comparison of the retrieved BFI for the uncorrected (uncorr, blue points) and IRF-corrected (corr, brown points) fits, together with the reference BFI obtained with ungated analysis (CW, dashed line). (b) Measured β parameter (from the amplitude of the autocorrelations), for the 5 considered temporal gates. For both the panels, the error bars report the measured mean and standard deviation across all the repetitions.

As shown in Figure 4-5(b), the measured autocorrelations seem to be fitted well both by the uncorrected and IRF-corrected models (with a slight difference only for the late gate case). However, the retrieved BFI in Figure 4-6(a) is much different for the two cases. In particular, we see that the BFI, retrieved using the uncorrected model (blue points), has a large discrepancy from its the reference CW value, especially for late times (>1 ns). This might be an effect of the IRF tail, which maps a certain fraction of the early photons in the later gates. Due to this, the measured photons have (on average) smaller path lengths than expected, thus obtaining an underestimation of the BFI. On the other hand, if one considers the IRF effect, the retrieved BFI well matches the expected one (brown points). In particular, for the later gates the average discrepancy (from the reference) is reduced from 37% to 3%.

Finally, see Figure 4-6(b), the β parameter is relatively high for all the considered gates. Thus, we might assume that the finite coherence is not significantly affecting the BFI estimation (see Section 4.1).

To summarize, in this section I compared two theoretical models for the analysis (i.e., fitting) of the measured autocorrelations curves. I showed that the proposed IRF model enables to retrieve more accurately the BFI, especially for later gates. This result is important since it might enable to measure quantitatively the BFI, which is crucial for many biomedical applications.

4.3. Laser sources comparison

In this Section, I will compare the performance of different laser sources, in order to assess their suitability for TD-DCS [166]⁴. In particular, I compared the following laser sources:

1. Pulse diode laser (PDL 800-D+LDH-P-C-N-760, PicoQuant, Germany)
2. Ti:Sapphire laser
3. Master Oscillator Fiber Amplified laser (VisIR-765-HP "STED", PicoQuant, Germany)

The Ti:Sapphire laser is the source typically used in the setup (see Section 3.2.1). The pulse diode laser (which I will name LDH) is a compact laser, which was optimized by the producer for narrow-band emission, with 12 mW maximum power. The fiber amplified laser (which I will name VisIR) is a high-power laser, with 560 mW maximum power. The PDL and VisIR lasers are both fiber coupled, 80 MHz repetition rate, with emission wavelength $\lambda = 760$ and 765 nm (respectively). Due to the slightly lower wavelength of the two commercial lasers (compared to the typical value), the Ti:Sapphire was tuned to $\lambda = 763 \text{ nm}$ for ease of comparison.

4.3.1. Emission bandwidth and pulse temporal shape (IRF)

As initial characterization, we measured the spectrum of the three laser modules using a commercial spectrometer (Anritsu MS9710B, 0.07 nm

⁴ Article #4 in the list of Publications.

resolution). Also, we measured the instrument response function (IRF) of each laser module using the general setup presented in Chapter 3. For these measurements, in particular, a single mode detection fiber with $4.4\ \mu\text{m}$ core diameter (780HP, Thorlabs, Sweden) was coupled with the SPAD detector (see Section 3.3). Then, the detected photons were acquired with a TCSPC board (SPC-130, Becker&Hickl, Germany). The resulting spectra and IRF are reported in Figure 4-7.

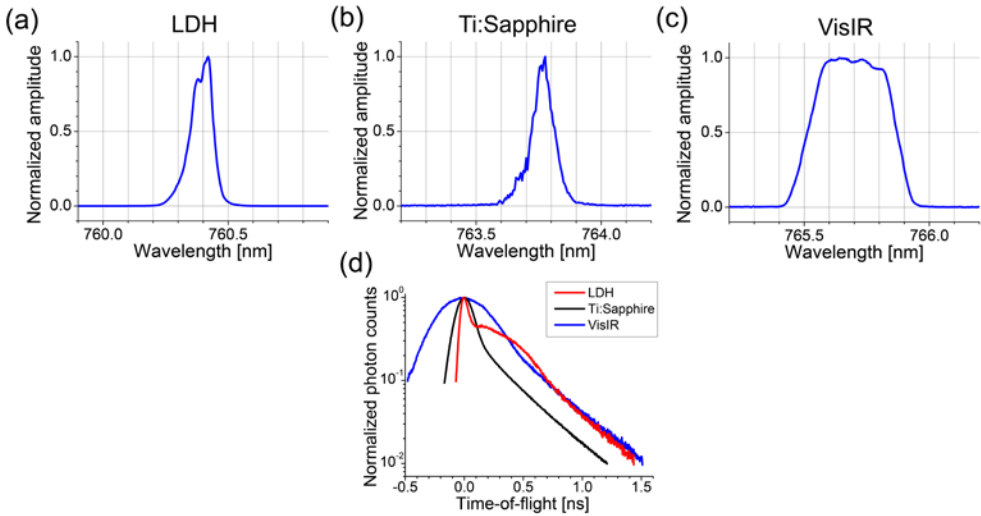


Figure 4-7: (a-c) Measured emission spectra for each laser module, normalized to amplitude. (d) Comparison of the IRF for each laser, normalized to amplitude and with $t = 0$ ns defined as the peak of the IRF. Figure adapted from Ref. [166].

From Figure 4-7(a-c) it is possible to note that the emission bandwidth of the LDH and Ti:Sapphire laser are similar, while the VisIR laser has a larger bandwidth. Regarding the temporal performance, Figure 4-7(d), the Ti:Sapphire has a relatively narrow IRF, while the LDH has a secondary peak which might be due to saturation of the emitting diode. The broad peak of the VisIR might be related to dispersion or non-linearities in the amplification process. For all three lasers, the IRF has a long tail which is mainly determined by the SPAD detector (so-called diffusion tail) [19].

In Table 1, I report a summary of the measured parameters. In particular, the wavelength λ and emission bandwidth $\Delta\lambda$ were directly

extracted from the measured spectrum. The coherence length was estimated, assuming a Gaussian spectrum, using the relation $L_c = \lambda^2 / \Delta\lambda$ [167]. The last two columns refer to the IRF full width at half-maximum (FWHM), and IRF width at 10% of its maximum.

Table 1: Comparison of the three lasers modules. The quantities were extracted from the spectral (first three columns) and IRF (last two columns) measurements.

| Laser module | Wavelength λ [nm] | Emission bandwidth $\Delta\lambda$ [nm] | Coherence length L_c [mm] | IRF FWHM [ps] | IRF width at 10% of maximum [ps] |
|--------------|---------------------------|-----------------------------------------|-----------------------------|---------------|----------------------------------|
| LDH | 760 | 0.095 | 6.1 | 106 | 776 |
| Ti:Sa | 763 | 0.093 | 6.3 | 185 | 575 |
| VisIR | 766 | 0.359 | 1.6 | 535 | 1173 |

Table 1 summarizes some preliminary information for characterizing pulsed laser modules. However, as we have seen in the previous sections, a measurement of the (time-gated) autocorrelation is necessary for evaluating the laser performance more directly. For this reason, in the next section I will show the results of phantom experiments using the different lasers. This might help to elucidate the relationship between spectral/temporal profile and the overall system performance e.g., coherence parameter β , and blood flow index (BFI).

4.3.2. Coherence parameter (β)

Here, I will report the results of liquid phantom experiments performed with the three different lasers (LHD, Ti:Sapphire, and VisIR). In particular, we prepared a liquid phantom having nominal optical properties $\mu'_s = 10 \text{ cm}^{-1}$ and $\mu_a = 0.06 \text{ cm}^{-1}$. The absorption was modified by adding a calibrated batch of Black Ink to the mixture,

according to Ref. [161]. We considered two differed source-detector separations: $\rho = 1 \text{ cm}$ and 1.5 cm . For each measurement, we acquired a fixed number of photons, 5 million (M) photons, considered 5 different repetitions (for evaluating variability), and computed the corresponding (gated) autocorrelation functions. In the case of the LDH laser, we discarded the $\rho = 1.5 \text{ cm}$ data due to the limited count rate. Finally, four different gate widths were considered: 50, 100, 200, and 400 ps. Figure 4-8 shows the resulting β parameter, estimated from the amplitude of the autocorrelations, for the two different source-detector separations (SDS, rows), and three lasers (columns). Time $t = 0 \text{ ns}$ was defined as the IRF maximum.

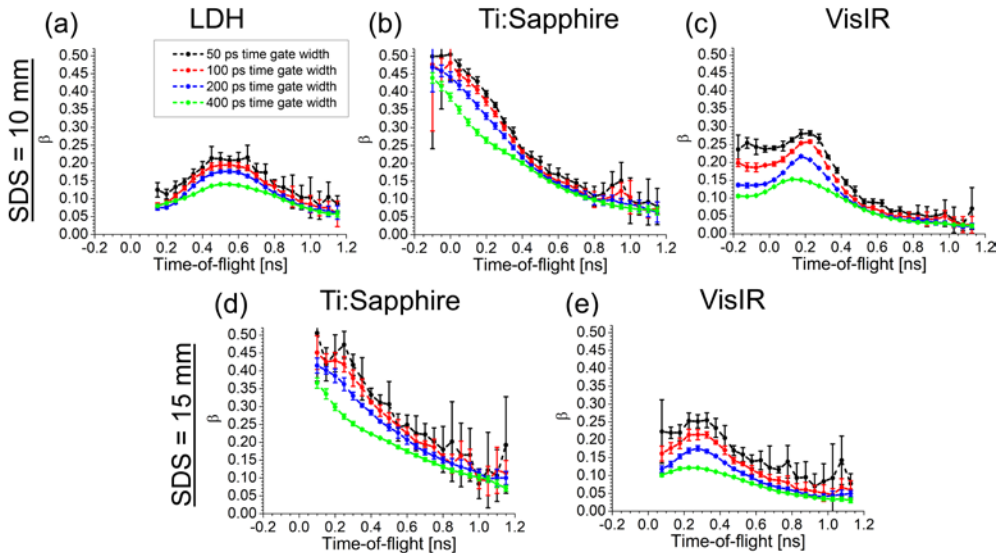


Figure 4-8: Measured coherence parameter (β) for the three different lasers (columns), and two source-detector separations (SDS, rows). Different colours map different gate widths (see legend). Average and standard deviation were computed along 5 different repetitions, each having a fixed number of photons (5 M). Figure adapted from Ref. [166].

In Figure 4-8, it is possible to see that the measured β parameter depends strongly on the considered laser source, and the SD separation (which modifies the path length distribution). Also, shorter gate widths correspond to higher β values, as expected by the lower spread of photon path lengths. Interestingly, it seems that the

β parameter does not depend only on the emission bandwidth ($\Delta\lambda$) - or equivalently the coherence length (L_c) - but also on the pulse temporal shape. For instance, the LDH and Ti:Sapphire laser have similar emission bandwidths (~ 0.1 nm), but the β parameter of the Ti:Sapphire laser is almost double. This might be due to the lack of secondary peaks in the Ti:Sapphire IRF. Also, the dependence of the β parameter on the gate position is qualitatively different for the three lasers. Thus, we might see that there is a complex interplay between coherence length (L_c), pulse duration (IRF), and gate position (and width). Let me note that researchers have developed a theoretical model for predicting the temporal trend of β , by adapting the model of Bellini *et al.* [23] to the pulsed regime [89]. However, the proposed model did not match accurately the experimental observations.

4.4. Single-photon detectors comparison

In this Section, I will compare few single-photon detectors, in order to assess their suitability for TD-DCS experiments. I will start from the typical spectral window (i.e., $\lambda = 785$ nm). In this case, the two detectors I considered are (see Section 3.3):

1. single-photon avalanche diode (SPAD)
2. single-photon superconducting nanowire detector (SPSND).

Regarding the setup, the experiments were performed with the Ti:Sapphire source, and the Swabian TCSPC board (see Sections 3.2.1 and 3.4). As in the previous sections, I have performed liquid phantom experiments. The phantom was prepared with nominal optical properties $\mu'_s = 10$ cm⁻¹ and $\mu_a = 0.02$ cm⁻¹. The measurement with the two detectors were performed in parallel, with source-detector separation $\rho = 1$ cm. Here, I will evaluate the performance in terms of i) IRF/DTOF curves, and ii) the time-gated autocorrelation functions.

4.4.1. IRF and DTOF curves

As initial comparison, the instrument response function (IRF) and distribution of time-of-flights (DTOF) curves were evaluated. In Figure

4-9, I compare the two curves for the SNSPD and SPAD detectors [top and bottom rows, respectively].

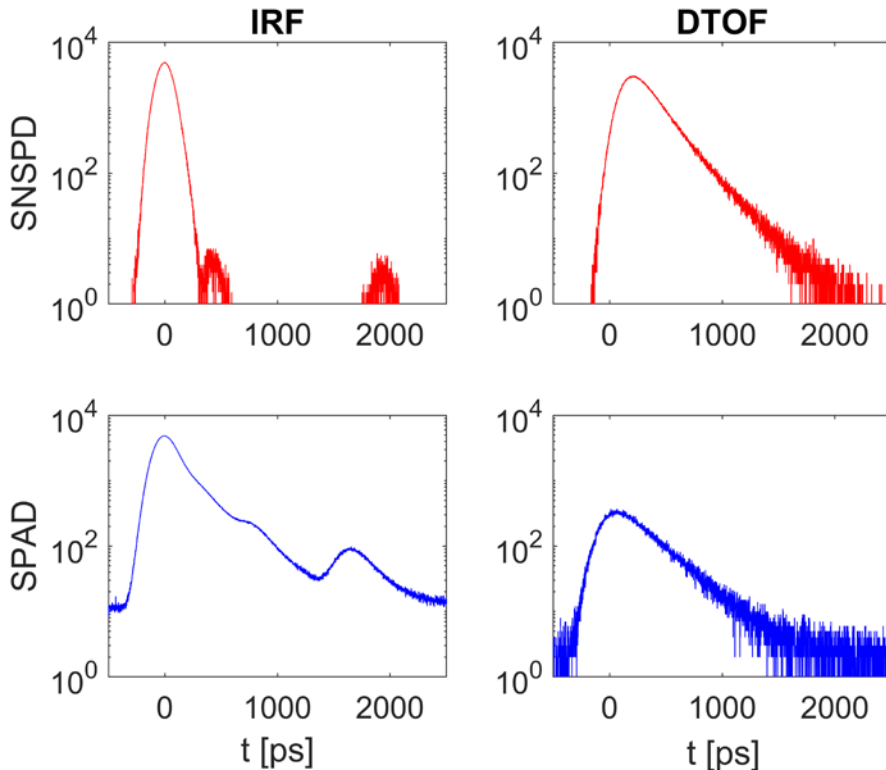


Figure 4-9: Comparison of the IRF (left columns) and DTOF (right columns) for the SNSPD (top row, in red) and SPAD (bottom rows, in blue) detectors. The time $t = 0$ ps was set to the peak of the IRF. Integration time was 0.1 s, no background subtraction. Note the different shape of the IRF, and dynamic range of the IRF and DTOF.

As shown in Figure 4-9, the SNSPD and SPAD detectors exhibit significantly different temporal responses. The IRF full width at half maximum (FWHM) are not very different, however at late times the SPAD shows a long tail (so-called diffusion tail), which is completely absent for the SNSPD detector. This is due to the different detection mechanism in the two detectors. Also, the background level (which is the sum of the dark counts and the after-pulsing) is much lower for the SNSPD. Finally, the SNSPD has a higher quantum efficiency compared to semiconductor-based detectors. Thus, the dynamic

range is at least 1 decade higher (see below). Regarding the possible integration in other systems, the SPAD has a relatively small size (~ 5 cm) and much simpler operation, as compared to the SNSPD which is quite bulky and complex.

In Table 2, I summarize the main *figures of merit* of the two detectors. In the first three columns, the measured IRF full width at half maximum (FWHM), and its width at different fractions of the maximum (10% and 1%) are reported. The quantum efficiency and dark counts (nominal values) are also shown, together with the measured dynamic range.

Table 2: Comparison of the two single-photon detectors (SPAD and SNSPD)

| Detector module | IRF FWHM [ps] | IRF width at 10% of max [ps] | IRF width at 1% of max [ps] | Quantum efficiency (@ 785 nm) | Dark noise (cps) | Dynamic range (decades) |
|-----------------|---------------|------------------------------|-----------------------------|-------------------------------|------------------|-------------------------|
| SPAD | 250 | 648 | 2140 | 15% | 500 | ~ 3 |
| SNSPD | 162 | 303 | 436 | 90% | 10 | ~ 4 |

As can be seen in Table 2, the SPAD and SNSPD have significantly different performances, in particular in terms of temporal response (IRF), quantum efficiency, and noise/dynamic range. This is generally due to the different detection mechanism and architecture. However, as noted before, these differences come at the cost of a higher complexity (and size) of the SNSPD compared to the SPAD. Up to here, I have assessed the key figures of merit of the two single-photon detectors (SPAD and SNSPD). In the next sub-section, I will report a comparison of the (time-gated) intensity [$g_2(\tau)$] and electric field [$g_1(\tau)$] autocorrelations.

4.4.2. Auto-correlations functions

In this sub-section, I will compare the intensity auto-correlation functions measured with the aforementioned detectors (SPAD and SNSPD). As before, the liquid phantom had the optical properties $\mu'_s = 10 \text{ cm}^{-1}$ and $\mu_a = 0.2 \text{ cm}^{-1}$, and a source-detector separation $\rho = 1 \text{ cm}$ was used. Figure 4-10 reports, from a parallel measurement with the two detectors, a comparison of the ungated auto-correlation function $g_2(\tau)$, averaging 30 autocorrelations each having 0.1 s integration time (3 s in total).

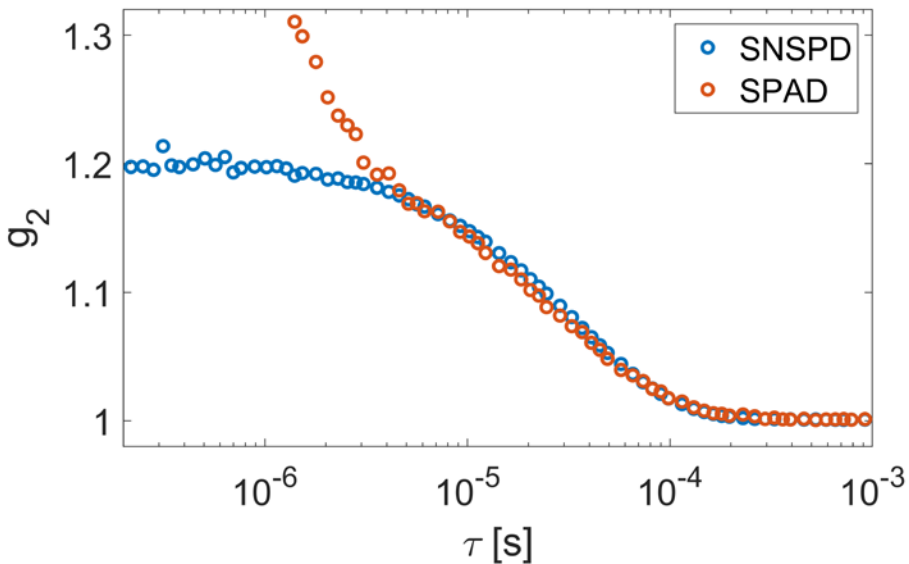


Figure 4-10: Comparison of the intensity auto-correlation function (ungated), for a parallel measurement with the SNSPD (blue) and SPAD (red) detectors. Note the highly different behaviour at short lag times (i.e., for $\tau < 10^{-6} \text{ s}$).

As can be seen from Figure 4-10, the intensity auto-correlation function has similar decay rates, however very different behaviours are present at short lag times i.e., $\tau < 10^{-6} \text{ s}$. This is related to the negligible after-pulsing probability of the SNSPD module, as compared to the SPAD. In fact, in the SPAD sensitive region, any microscopic defect might trap a photoelectron and subsequently trigger an avalanche (even in absence of an absorbed photon). The time scale of this process is in the micro-seconds range, thus the process causes an undesired

increase of the auto-correlation in that temporal region [168]. The SNSPD, on the other hand, does not suffer from this effect, since the electronic signal can be generated only when the nanowire absorbs a photon and exits from its superconducting state [155].

In this section, I have assessed the suitability of two single-photon detectors for TD-DCS. In particular, I focused on temporal response, efficiency, and noise properties. This might help in finding the best compromise between performance and complexity, based on the required application and environment (e.g., laboratory or clinics).

4.5. Wavelength comparison

In this section, I will briefly report the results of phantom experiments performed at longer wavelengths (i.e., $\lambda = 1000 \text{ nm}$) and compare them with experiments at the typically used wavelength ($\lambda = 785 \text{ nm}$). The longer wavelength has several possible advantages, such as higher penetration depth (due to the lower scattering), and a slower auto-correlation decay (which might improve the signal-to-noise ratio) [169,170]⁵.

For these experiments, I used the InGaAs photomultiplier at $\lambda = 1000 \text{ nm}$ and the SPAD at $\lambda = 785 \text{ nm}$ (see Section 3.3). In order to operate the Ti:Sapphire at the longer wavelength, it was necessary to substitute its cavity mirrors. In particular, the mirror set used here enables spectral tunability between 900 nm and 1000/1020 nm (see Section 3.2.1). As in the previous sections, I prepared a homogeneous liquid phantom by mixing 5% intralipid with 95% distilled water. This results in a nominal reduced scattering of $\mu'_s = 10 \text{ cm}^{-1}$ at $\lambda = 785 \text{ nm}$ and $\mu'_s = 7.4 \text{ cm}^{-1}$ at 1000 nm . The source-detector separation was $\rho = 1 \text{ cm}$, and the excitation power $\sim 50 \text{ mW}$. In both the experiments, 500 auto-correlation curves (1 s sampling time) were measured.

Figure 4-11 reports the average autocorrelations (intensity and electric field) for an early and late gate, and for ungated acquisition. The IRF width (FWHM) was approximately 400 ps in both cases, while the count

⁵ Article #2 in the list of Publications.

rate was 639 ± 2 kcps and 249 ± 3 kcps for the 785 nm and 1000 nm measurements, respectively.

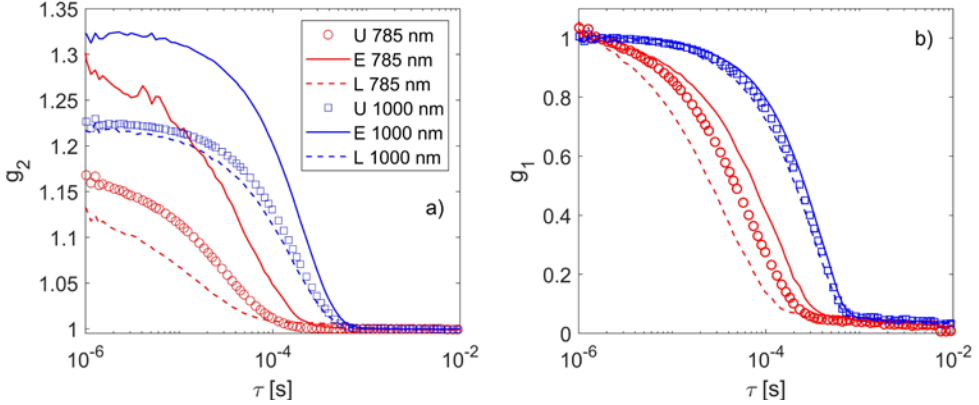


Figure 4-11: Comparison of the intensity (a) and electric field (b) auto-correlation functions [$g_2(\tau)$ and $g_1(\tau)$], measured at 785 nm (red curves) and 1000 nm (blue curves). The curves are shows for ungated acquisition (U, symbols), early gate (E, continuous lines), and late gate (L, dashed lines). Figure from Ref. [170].

As shown in Figure 4-11, moving to the longer wavelength we observe two major effects: i) higher coherence parameter β , and ii) slower auto-correlation decays. The β parameter increase - here from 0.16 to 0.22 in the ungated case - is probably due to the change of optical properties, which narrows the path length distribution $P(s)$ (see Section 4.1.2). Regarding instead the auto-correlation decay rate (defined as the point where $g_1(\tau) = 0.5$), here it moves from $45 \mu\text{s}$ to $217 \mu\text{s}$, becoming almost five times slower. This is a combined effect of the smaller wavenumber k_0 and the different optical properties (see Section 2.4). Even if different decay rates are seen, the measured blood flow index is $D_B = (1.0 \pm 0.1) \cdot 10^{-8} \text{ cm}^2/\text{s}$ and $(0.97 \pm 0.04) \cdot 10^{-8} \text{ cm}^2/\text{s}$ at 785 nm and 1000 nm, respectively, showing no significant change.

To summarize, in this Section I have shown that it is possible to carry out TD-DCS experiments also at longer wavelengths (i.e., at $\lambda \sim 1 \mu\text{m}$), discussing the differences observed in the measured autocorrelations.

Summary and perspective

In conclusion, in this Chapter, I reported several phantom experiments for characterizing the overall system performance (coherence and blood flow index), and the impact of the lasers source, detector, and wavelength on the quality of the experimental data. In the next two Chapters, I will exploit the developed system for two applications. The first concerns the physics of light propagation in random media, with the observation of temporal speckle (Chapter 5). The second concerns the biomedical application of the technique, for which I will show extensive *in vivo* measurements on adult volunteers (Chapter 6).

Chapter 5: Temporal speckle effect

In this Chapter, I will report an unexpected phenomenon, which I will term temporal speckle. This effect, novel for diffuse optics, causes large temporal fluctuations in the distribution of time-of-flights (DTOF) curve, and is more visible for samples having limited motion of the scatterers (e.g., solids). First, I will characterize this effect with different types of tissue-mimicking phantoms. Then, I will provide a statistical interpretation to elucidate its physical origin. Finally, I will demonstrate a possible biomedical application regarding the *in vivo* measurement of blood flow.

5.1. Experimental observations

In this Chapter, I will present the first experimental evidence of the temporal speckle effect in bulk diffusive media. In this and the following section (Sec. 5.1 and 5.2) I will report the results with tissue-mimicking phantoms [133]⁶, while in Sec 5.3 I will move to *in vivo* experiments to demonstrate a novel biomedical application.

The experimental setup I used is summarized in Figure 5-1(a). Briefly, the light from the Ti:Sapphire source (see Section 3.2.1) is delivered to the sample and recollected, at a distance $\rho = 1.5\text{ cm}$, with a single mode fiber. On the acquisition side, the SPAD detector together with the PicoQuant TCPSC board (see Sections 3.3 and 3.4) were used. The bottom part shows, from a Monte Carlo simulation [171], the distribution of the re-collected photons, as a function of their time-of-flight (colour-map in the inset). As discussed in Chapter 2, photons with longer time-of-flights are characterized by a higher penetration depth (on average).

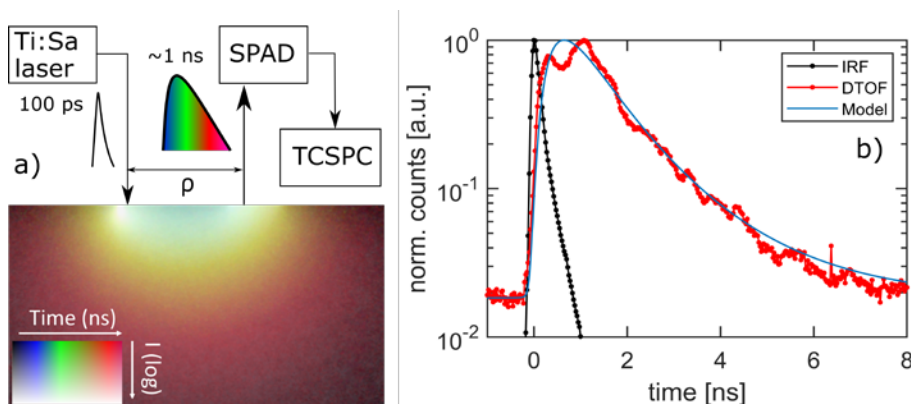


Figure 5-1: (a) Setup scheme: Ti:Sapphire (Ti:Sa) laser, the SPAD detector, and the TCSPC board. The source-detector separation is $\rho = 1.5\text{ cm}$. The bottom part shows, from a Monte Carlo simulation, the distribution of the re-collected photons as a function of their time-of-flight (colour-map in the inset) (b) Experimental results: instrument response function (IRF), measured distribution of times-of-flights (DTOF) from a solid resin phantom, and for comparison the theoretical curve (diffuse reflectance convolved with IRF). Figure from Ref. [133].

⁶ Article #3 in the list of Publications.

Figure 5-1(b) shows the experimental results for a tissue-mimicking solid resin phantom (4.5 cm height x 10.5 cm diameter), with nominal optical properties $\mu'_s = 18.9 \text{ cm}^{-1}$ and $\mu_a = 0.01 \text{ cm}^{-1}$ [172]. The instrument response function (IRF, black line) was measured by facing the injection and collection fibers, obtaining a 200 ps full width at half maximum (FWHM). The distribution of times-of-flights (DTOF, red line) was obtained by averaging 100 curves, 100 ms integration time each, for a total of 10 s. The result is compared with the theoretical time-resolved reflectance convolved with the IRF (Model, blue line).

As can be seen from Figure 5-1(b), the measured DTOF curve displays unexpected temporal fluctuations, which are not predicted by photon diffusion theory (Section 2.1). The effect might be due to the “coherent” interference of the diffusely reflected photons, which can be constructive or destructive depending on their specific path length. Let me highlight that the effect is observed only for high temporal coherence (i.e., very narrow bandwidth) and single-mode detection.

5.1.1. Effect of scatterers motion and fiber collection area

To elucidate the origin of the observed effect, I carried out experiments with samples having different scatterers motions, and collection fibers with different core diameters. The following samples were measured:

- a) Liquid phantom, with 5% of Intralipid and 95% of distilled water, nominal properties $\mu'_s = 10 \text{ cm}^{-1}$ and $\mu_a = 0.02 \text{ cm}^{-1}$,
- b) Flexible silicone phantom, nominal properties $\mu'_s = 10 \text{ cm}^{-1}$ and $\mu_a = 0.05 \text{ cm}^{-1}$,
- c) Solid resin phantom ($\mu'_s = 18.9 \text{ cm}^{-1}$ and $\mu_a = 0.01 \text{ cm}^{-1}$).

For each phantom, 3000 DTOF curves were measured continuously with 100 ms sampling time (300 seconds in total). Then, in order to quantify the variations, we computed the DTOF “contrast” as:

$$C(t, T) = \frac{DTOF(t, T) - \langle DTOF(t, T) \rangle_T}{\langle DTOF(t, T) \rangle_T} \quad (5-1)$$

Where $DTOF(t, T)$ is the measured DTOF curve as function of the time-of-flight t (so-called “micro-time”, in ns) and the elapsed time T (so-

called “macro-time”, in seconds), and $\langle \dots \rangle_T$ denotes temporal average over the elapsed time T .

In Figure 5-2 (top row) the colour-coded contrast $\mathcal{C}(t, T)$ is reported for the different phantoms, where the x-axis corresponds to the elapsed time T [s], and the y-axis to the time-of-flight t [ns]. As it is possible to see, for the liquid phantom (a) the DTOF fluctuations are absent. However, when the scatterers motion is increased i.e., for silicone (b) and resin (c), the DTOF fluctuations are increasingly apparent. Thus, the effect is observable only when the scatterers motion is sufficiently slow compared to the DTOF sampling time (here 100 ms). When this does not hold, the fluctuations are “averaged-out”, as in the case of the liquid phantom, and partly also for the silicone one. It is interesting to note that the position where the contrast is maximum (or minimum) changes over the course of the experiment i.e., over the elapsed time. This might be due to the combined effect of sample de-correlation and system drifts (e.g., source and optical fibers).

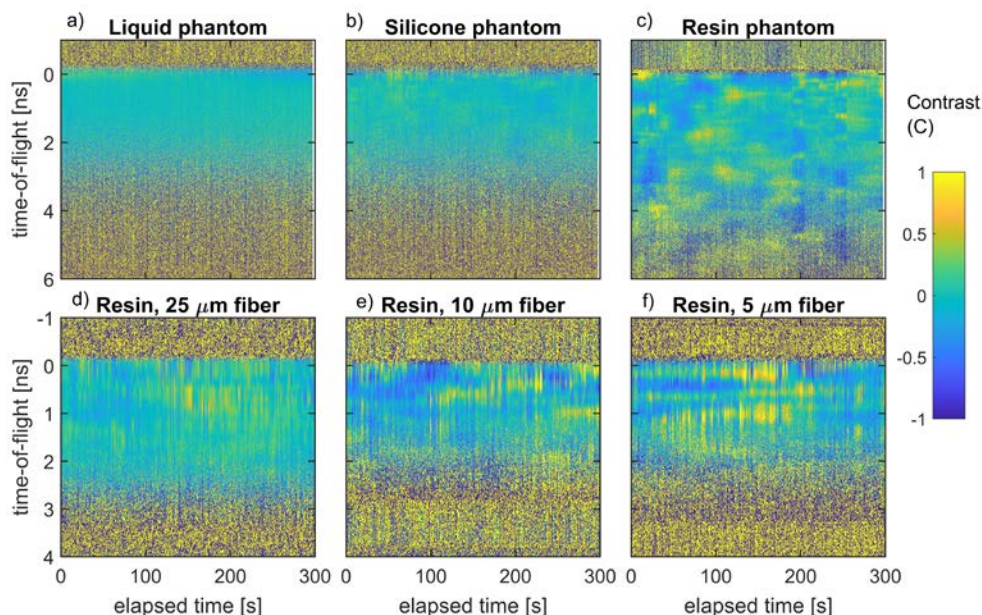


Figure 5-2: DTOF contrast (see Eq. 5-1) as a function of the elapsed time T (x-axis, in seconds) and the time-of-flight t (y-axis, in ns). Top rows (a-c): phantoms with different scatterers motions (liquid, silicone, and resin), single mode collection fiber ($5 \mu\text{m}$). Bottom rows (d-f): resin phantom, different collection fibers core diameters ($\phi = 25, 10, 5 \mu\text{m}$). Figure from Ref. [133].

In Figure 5-2 (bottom row) I report the measured DTOF contrast for a resin phantom having properties $\mu'_s = 10 \text{ cm}^{-1}$ and $\mu_a = 0.1 \text{ cm}^{-1}$, using different collection fiber core diameters: $\emptyset = 25, 10, 5 \mu\text{m}$. This gradually decreases the number of speckles collected at the surface of the sample [93]. As expected, the DTOF fluctuations are more visible when light is collected with smaller core diameters, in particular with the $5 \mu\text{m}$ core (single mode fiber).

In summary, we might see that the measured contrast displays, at least qualitatively, the scaling relations typically of *spatial* speckle patterns. In particular, the contrast/visibility increases when more rigid samples are measured, and when smaller collection areas are used. However, in this case the fluctuations are observed in the *temporal* domain, thus we might consider this effect as an example of **temporal speckle**. The effect has been observed in other fields such as seismology [173–175], acoustic waves [176,177], excitonic emission [178], THz spectroscopy [127,179], and laser ranging [180,181]. It has been also observed in the field of optics in random media, but only for thin scattering samples [22,128,182–186]. In the next section, I will propose a new approach for the analysis and interpretation of the observed effect, adapting Goodman's statistical theory [21] to the time-resolved regime.

5.2. Physical interpretation

5.2.1. Statistical model

In this Section, I will provide a physical model to interpret the observed DTOF fluctuations, adapting speckle statistics to the pulsed regime. As we have seen in Section 2.2, in the general case, the measured intensity probability can be described as a *mixture* of speckle fluctuations (due to the light interference) and Poisson noise (due to the detection process). By looking at Eq. (2-8), we might see that the variance σ_I^2 of the measured intensity depends of the number of *effective* modes M [21,93]. By exploiting the relationship between coherence parameter and M i.e., $\beta = 1/M$ we might express the overall variance σ_I^2 as:

$$\sigma_I^2(t) = \langle I(t) \rangle + \beta(t) \langle I(t) \rangle^2, \quad (5-2)$$

where the possible dependence of the quantities on the photon time-of-flight t was made explicit. In fact, as we have seen in Chapter 4, not only the intensity (i.e., DTOF) but also the coherence parameter (β) are generally time-dependant [79,89]. Thus, we might see that the measured variance (for a fixed time-of-flight t) is simply given by the sum of Poisson noise and speckle fluctuations, which have a (relative) strength determined by $\beta(t)$. Let me note that this model is strictly valid only for quasi-static samples, because it does not consider sample de-correlations.

5.2.2. Experimental results

In order to verify this physical interpretation, I measured a resin phantom, with nominal properties $\mu'_s = 4.7 \text{ cm}^{-1}$ and $\mu_a = 0.059 \text{ cm}^{-1}$, under different laser temporal coherence levels. In particular, three different pulse durations (IRF FWHM) were considered: 450, 225, and 175 ps. The pulse duration was tuned by increasing the RF power of the acousto-optic modulator⁷. Each measurement had a duration of 300 seconds (5 min), from which the DTOF and autocorrelation curves were extracted.

Regarding the DTOF curves, they were measured with 100 ms sampling time. From the DTOF curves, the intensity variance ($\sigma_I^2(t)$) was evaluated for each “micro-time” channel (25 ps width) independently, and de-noised with a 200ps-width moving average. This, coupled with the measured $\langle I(t) \rangle$ (obtained by averaging all the measured DTOF), enabled to estimate $\beta(t)$ by inverting Eq. (5-3).

This result was compared with the “ground-truth” $\beta(t)$, measured from the amplitude of the time-resolved autocorrelations $g_2(\tau, t)$, with a 100 ps gate width and 10 s sampling time. The coherence parameter was obtained by fitting, for each time-gate, the measured $g_2(\tau, t)$ in the range $\tau = 10^{-6} - 10^{-5} \text{ s}$, with respect to amplitude and decay rate

⁷ For each RF power (carrier level), the pulse duration was minimized by tuning the RF frequency and laser cavity length (see Section 3.2.1).

(single-exponential model for simplicity). Finally, from the measured $\beta(t)$ the average and standard deviation was computed across 30 repetitions. Figure 5-3 report a comparison of the $\beta(t)$ computed from the autocorrelations $g_2(\tau, t)$ (blue points with shaded standard deviation), and from Eq. (5-4), for the three different pulse durations considered.

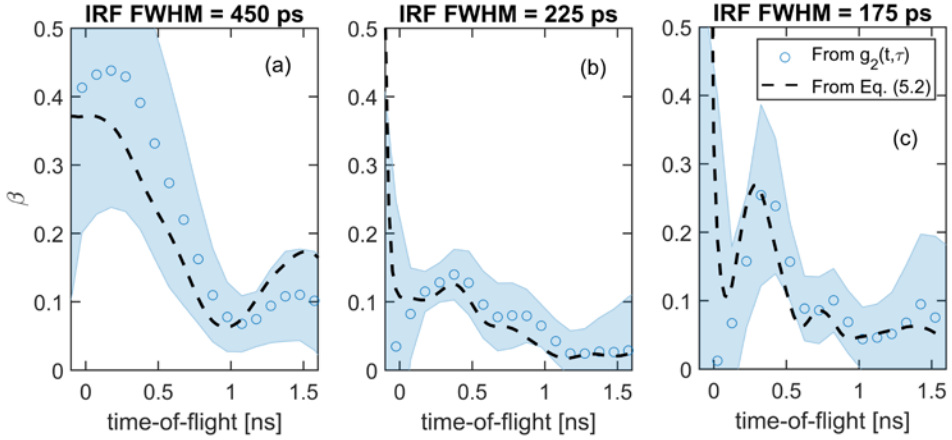


Figure 5-3: Comparison of the measured $\beta(t)$ from the amplitude of the autocorrelations $g_2(t, \tau)$ (blue points with shaded standard deviation), with the $\beta(t)$ retrieved with Eq. (5.2) using the measured intensity fluctuations $\sigma_I^2(t)$ and average intensity $\langle I(t) \rangle$. The three subplots correspond to three different pulse durations (IRF FWHM): a) 450 ps, b) 225 ps, and c) 175 ps. Figure adapted from Ref. [133].

As shown in Figure 5-3, the $\beta(t)$ retrieved with Eq. (5-5) agrees well (within experimental variability) with the “ground-truth” measured from the amplitude of the intensity autocorrelations. This indicates that the observed fluctuations can be indeed described by (time-resolved) speckle statistics. As we have seen in the previous Chapter, the temporal behaviours of $\beta(t)$ depends both on the pulse shape and coherence properties, and on the sample optical properties (which modulate the path length distribution) [89]. The proposed statistical model does not aim to predict this complex interplay, instead it was used to guide the physical interpretation of the observed DTOF fluctuations. Finally, let me highlight that the understanding of this phenomena might help in designing future experimental systems.

5.3. Biomedical application

In this Section, I will report a novel biomedical application of the observed effect. We have seen that the strength of the DTOF fluctuations is related to the amount of scatterers motion. For this reason, it might be interesting to study whether the effect is observable also *in vivo*. For this reason, I have conducted an arterial occlusion experiment on an adult volunteer. The optical probe was placed on the forearm of the subject, in correspondence of the brachioradialis muscle. A pneumatic tourniquet was placed in the midpoint between the elbow and the armpit of the subject. To comply with ANSI safety limits, the excitation power was reduced to 30 mW with the variable attenuator. The subject, wearing laser safety goggles, was seated with the arm resting on a table (approximately at the heart level). The protocol was composed of three phases, with a total duration of 10 minutes:

- Baseline (2 min), tourniquet deflated
- Arterial occlusion (3 min), tourniquet inflated at 220 mmHg pressure
- Recovery (5 min), tourniquet deflated

The baseline count rate was approximately 200 kcps. The DTOF curves were computed in post-processing with 100 ms sampling time (10 Hz). In order to quantify the fluctuations, the so-called “speckle contrast” was computed by inverting Eq. (5-1):

$$k^2 = \frac{\sigma_I^2 - \langle I \rangle}{\langle I \rangle^2} \quad (5-3)$$

Note that the symbol β is replaced with k^2 for being consistent with speckle contrast literature [25,31]. In the experiment, the variance σ_I^2 and average intensity $\langle I \rangle$ were computed from the DTOF total counts, considering a 5 second moving window (50 time points).

Figure 5-4(a) reports the count rate measured during the experiment (integral of the DTOF curves normalized to the sampling time). As can be seen, the count rate is relatively stable during the baseline. On the

other hand, during the occlusion (starting at minute 2) the count rate starts to oscillate strongly, resuming to its previous condition only when the tourniquet is released (at minute 5). Figure 5-4(b) reports the temporal evolution of $1/k^2$, which was shown in literature to scale as the blood flow [31,187], normalized to its baseline average value. Its temporal evolution has the expected trend: it decreases by more than one decade during the occlusion part and shows has a strong increase few seconds after the occlusion is release (so-called hyperaemic peak) [87].

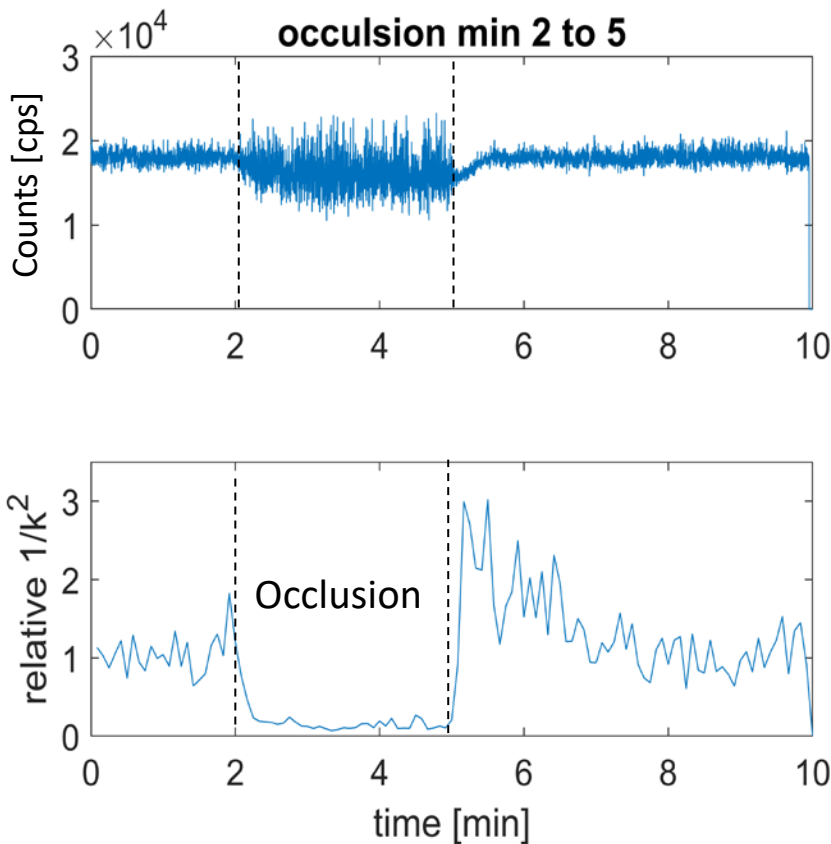


Figure 5-4: Arterial occlusion experiment a) DTOF total counts (cps), with 100 ms temporal resolution. The black dashed lines enclose the occlusion period (from minute 2 to 5). b) Reciprocal of the speckle contrast (normalized to the initial baseline) temporal evolution, where the occlusion and hyperaemic peak (after minute 5) are clearly visible.

Summary and perspective

In summary, in this Chapter I have reported and interpreted a novel effect in the field of diffuse optics, namely the temporal speckle effect. I have shown that it is observable not only in phantom experiments, but also *in vivo*, and that it can give insightful information regarding the physiological condition of tissues. This results give insights of the possible applications of the observed effect, for instance the measurement of tissue blood flow. In fact, to observe the effect, the knowledge of the intensity auto-correlation functions is not needed, thus the analysis might be performed with much lower computational cost.

In the next Chapter, I will return on the classical DCS approach (based on the temporal autocorrelations functions), since it is a more consolidated method for measuring the blood flow. In particular, I will report several *in vivo* experiments, both on the muscle and the brain, with the aim to assess the performance and the applicability of the technique in biomedical settings.

Chapter 6: *In vivo* experiments

In this Chapter, I will present several examples of the *in vivo* experiments which were carried out during this work. First, I will present the materials and methods (i.e., protocols) specific to these experiments. Then, I will focus on two applications: cuff occlusion and head measurements. Finally, I will present few results in the spectral region beyond $1 \mu m$. Let me highlight that the presented results have not the aim to represent a systematic study, but to perform an evaluation of the developed system and its possible applications.

6.1. Materials and methods

In this section, I will present the materials and methods which were used for the *in vivo* experiments presented in this Chapter. I will conceptually divide the description in three parts:

1. Optical probe and physiological sensors
2. Protocols
3. Data analysis

6.1.1. Optical probe and physiological sensors

For the experiments, a custom optical probe was 3D-printed in our laboratory. The probe, having a square footprint with rounded angles, had precisely sized holes for inserting the source and detection fibers, which had all FC connectors, see Figure 6.1. The illumination fiber (see Section 3.1) was placed at the centre of the probe. The collection fibers (up to 6 single mode fibers) were placed circularly symmetric with respect to the source fiber, at a source-detector separation $\rho = 1\text{ cm}$ (or 1.5 cm). Both the illumination and detection fiber were perpendicular to the tissue (i.e., not bended).

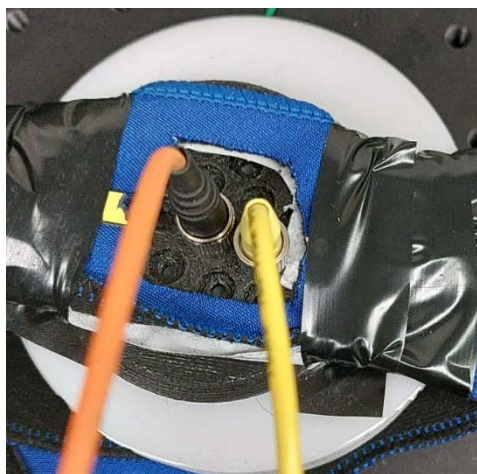


Figure 6-1: Photo of the custom optical probe, with the source and collection fibers (orange and yellow, respectively). The blue band is used for attaching the probe to the tissue.

In several cases, I have also used additional physiological sensors, which were suitably synchronized with the optical (i.e., TD-DCS) data. As introduced in Section 3.5, the sensors used were:

- i) Electrocardiogram (EKG),
- ii) breath rate (BR),
- iii) blood volume pulse (BVP).

The EKG sensor had 3 electrodes (positive, negative, and ground). The positive and negative electrodes were placed below the subject's clavicles, the ground close to the subject's navel. The BR sensor was a flexible band which was placed around the subject's chest, passing through the bottom of the sternum. The BVP sensor was placed on the fingertip (right hand, index finger).

6.1.2. Protocols

In this Section, I will describe the (in vivo) protocols which were used in the experiments presented in this Chapter. In the majority of the experiments, the wavelength used was $\lambda = 785 \text{ nm}$, excluding the last Section where I will present experiments at $\lambda = 1000 - 1020 \text{ nm}$. The protocols I will present are:

1. Cuff occlusion (forearm)
2. Resting state (forehead)
3. Breath hold (forehead)

Cuff occlusion

The cuff occlusion experiment is a relatively simple protocol which is used to assess the muscular reactivity to external perturbations. As shown in Figure 6-2, the subject is asked to lay its arm on a table. A pneumatic tourniquet is placed above its elbow, and the optical probe is placed on the brachioradialis muscle (forearm). The protocol is composed of three phases:

- baseline (2 min),

- occlusion (variable duration, see below),
- recovery (5 min).

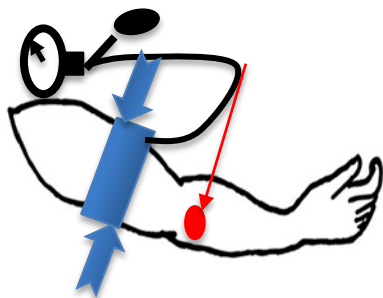


Figure 6-2: Schematics of the cuff occlusion experiments, where the positions of the inflatable tourniquet (blue band) and the optical probe (red circle) are highlighted.

In the baseline, the tourniquet is kept deflated. In the occlusion, the tourniquet is inflated manually to a certain pressure level, which is maintained constant. In the recovery, the tourniquet is deflated in a couple of seconds and maintained empty up to the end of the experiment.

In this thesis work, I performed two types of protocols: an **arterial** occlusion or **venous** occlusion. In the first, the tourniquet is inflated to a 220-mmHg pressure for 3 minutes, in order to block the blood flow in all the circulatory compartments (arteries included). In the second, the tourniquet is inflated approximately to 100-mmHg pressure for 20 seconds, in order to block only the venous flow⁸. Let me highlight that the two protocols are expected to induce different physiological responses in the tissue.

Resting state and breath hold

Here I will describe the two other protocols which will be presented in this chapter: resting state and breath hold. In both cases, the subject

⁸ Note that the venous occlusion pressure is chosen to be intermediate between the systolic and diastolic blood pressures of the subject (measured before the protocol with a standard blood pressure sensor).

was asked to lay on a bed tilted at 45°. The optical probe was placed on the forehead, in correspondence of the FP1 point of the 10-20 EEG reference system. The other physiological sensors were also used (see the previous sub-section). The two protocols were defined as follows:

- **Resting state** protocol: the subject was asked to breath normally (without a metronome), for 7 minutes in total.
- **Breath hold** protocol, subdivided in this way:
 1. Baseline (1 minute)
 2. $\left\{ \begin{array}{l} \text{i) Breath IN (5 seconds)} \\ \text{ii) Breath OUT (5 seconds)} \\ \text{iii) Breath HOLD (20 seconds)} \\ \text{iv) Normal breathing (2 minutes)} \end{array} \right.$

where block #2 was repeated 3 times, for a total duration of 7.5 minutes.

Let me highlight that, while the aim of the resting state protocol was to monitor the cerebral blood flow in a standard physiological condition, the breath hold protocol was designed to study the cerebral auto-regulatory response to an external (yet transitory) perturbation.

6.1.3. Data analysis

As described in Section 3.4, the TD-DCS raw data consists of a time-tags file, which contains the time-of-flight (TOF) and absolute arrival time of each detected photon. The post-processing algorithm (so-called software correlator) was described in detail in Section 3.4.2. Briefly, the autocorrelations $g_2(t, \tau)$ are computed binning the data with a fixed sampling rate, typically between 1 and 10 Hz (depending on the application and given count rate). The temporal gates (i.e., TOF gate) are also selected in post-processing, in order to optimize the signal-to-noise ratio (SNR) and depth sensitivity.

The intensity autocorrelations are then fitted using the model described in Section 2.4.2, with two free parameters: the coherence parameter (β) and the blood flow index (BFI). Typically, the autocorrelations are fitted from $\tau > 10^{-6}$ s to the point where $g_1(\tau) = 0.5$ (in order to avoid the after-pulsing and the low SNR region at short and long τ ,

respectively). The resulting BFI might then be normalized to the baseline period, to obtain a relative BFI (rBFI) temporal trace (for each time gate).

Let me highlight that the tissue optical properties (absorption μ_a and reduced scattering coefficient μ'_s) are necessary for a correct BFI estimation. Their value was obtained by fitting the baseline-averaged DTOF curve with respect to the theoretical time-resolved diffuse reflectance (see Section 2.1.1) convolved with the IRF (measured by facing the illumination and detection fibers). In specific cases, such as in the beyond $1\ \mu\text{m}$ experiments (performed with an InGaAs photomultiplier having a broad IRF), the optical properties were measured with a different time-resolved diffuse optical spectroscopy system [154].

6.2. Cuff occlusion experiments

In this Section, I will present the result of the cuff occlusion experiments introduced in Section 6.1.2. The experiments were carried out with three different laser sources, introduced in Section 4.3, and for $n = 3$ different subjects [166]⁹. In particular, here I will show the results of arterial cuff occlusions experiments (220 mmHg tourniquet inflation). The aim of the measurements is to evaluate the optimal laser source, and to evaluate the usability of the overall system, for *in vivo* experiments on human subjects.

In the experiments, the SPAD detector (see Section 3.3) was used. Three 100ps-wide temporal gates were considered, centred at $t = 240$ ps (early gate), 390 ps (intermediate gate), and 540 ps (late gate) with respect to the IRF peak (defined as $t = 0$ ps). The autocorrelations were computed with 5 s sampling time and fitted to extract the BFI of each gate (as described in Section 6.1.3). Then, the BFI was normalized to the baseline value, to retrieve a relative BFI (rBFI).

Figure 6-3 reports the experimental results, where the columns refer to the three different subjects, and the rows to the three different lasers used (LDH, Ti:Sapphire and VisIR). Note that while for the Ti:Sapphire and VisIR the power was limited to 30 mW, for the LDH the power was

⁹ Article #4 in the list of Publications.

12 mW (the maximum achievable with this source). From Figure 6-3, we might see that the measurements show a sufficiently good signal-to-noise ratio (SNR) for following hemodynamic variations. In particular, the measured rBFI, for all the experiments and gate positions, has the expected temporal trend: it decreases by more than one decade during the occlusion, and it exhibits a large peak after the release, so-called hyperaemic peak. The latter effect is a response to the lack of oxygen in the tissue, induced by the occlusion manoeuvre. Thus, the rBFI trend is qualitatively in agreement with the expected results. In order to perform a more detailed analysis, we have analysed the hyperaemic region (after the occlusion release) in more detail. In particular, Table 3 reports the value of the rBFI hyperaemic peak (10-20 seconds after the occlusion release), averaged across the three subjects.

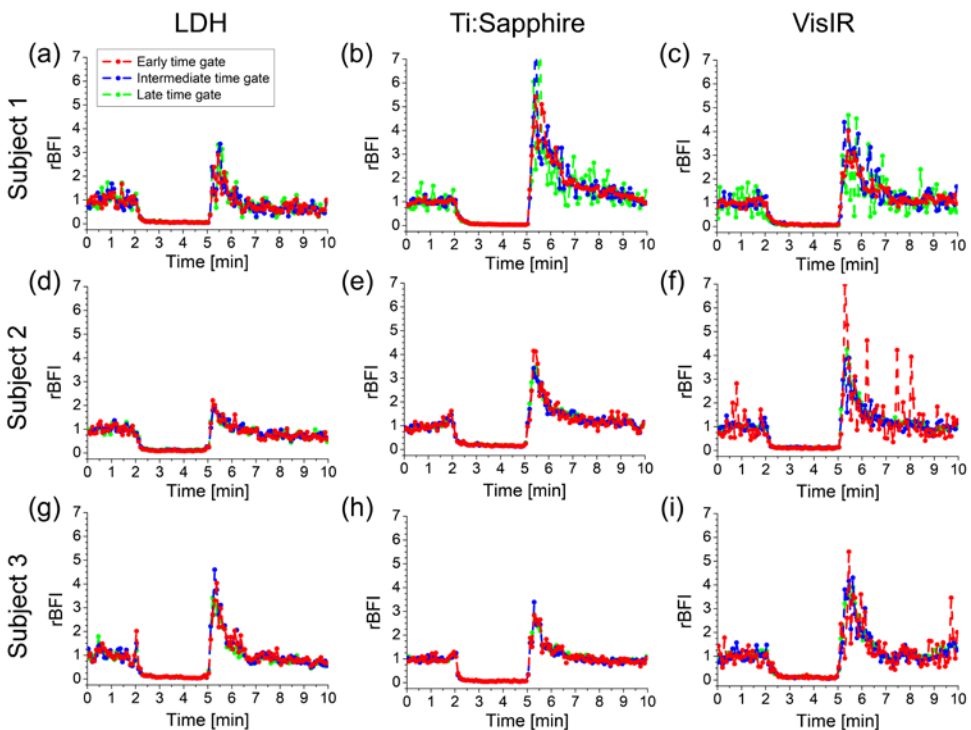


Figure 6-3: Results of the cuff occlusion experiments. Each row corresponds to a different subject, while each column to a different laser source (LDH, Ti:Sapphire and VisIR). The occlusion (220 mmHg pressure) was performed from minute 2 to minute 5. The rBFI time trace is shown for an early gate (red), an intermediate gate (blue), and a late gate (red points). Figure from Ref. [166].

Table 3: Values of the rBFI at the hyperaemic peak (10-20 s after the occlusion release), averaged across the three subjects, for the three considered laser sources (columns) and gate positions (rows).

| Gate position | LDH | Ti:Sapphire | VisIR |
|---------------|-----|-------------|-------|
| Early | 2.6 | 3.8 | 3.7 |
| Intermediate | 2.7 | 4.8 | 4.0 |
| Late | 2.4 | 3.8 | 4.5 |

From Table 3 it is possible to see that, in general, the measured rBFI shows similar hyperaemic values for the three considered time gates, probably due to a limited thickness of the tissue's superficial layers (between 2.7 and 6.5 mm, as measured with a mechanical calliper), which limits the possibility to disentangle superficial from deeper hemodynamics. In addition, the hyperaemic peak value does not show large changes for different laser, except for the LDH laser which is characterized by a lower average power.

To summarize, in this section I showed that TD-DCS is capable of monitoring dynamic hemodynamic changes with sufficient SNR. Let me highlight that, due to the single-mode detection requirement, large laser powers (yet not exceeding the skin safety limit) are necessary for a precise BFI estimation, especially for gated acquisition. Here, as initial assessment, I showed experiments for three different laser sources. However, in the next sections I will restrict myself to the Ti:Sapphire source, due to its high flexibility in terms of temporal duration and emission wavelength.

6.3. Brain experiments

In this Section, I will present the results of *in vivo* experiments performed on the forehead. I will focus first on resting state experiments, then on dynamic experiments (breath hold), see Section 6.1.2 for protocol details. In both cases, the experiments were performed with the Ti:Sapphire source, the superconducting nanowire single-photon detector (SNSPD), together with the Swabian TCSPC (see Sections 3.2-4). As we will see, the high efficiency of the SNSPD enables measurements at high sampling rates, in this case down to 10

Hz in gated acquisition. This might enable to study physiological phenomena which are difficult to measure with “standard” detectors¹⁰.

6.3.1. Resting state: vascular pulsatility

In this sub-section, I will focus on resting state experiments. The TD-DCS probe and the other physiological sensors (EKG, Breath monitor, and BVP) were positioned on the subject (see Section 6.1), and the data were acquired continuously for 7 minutes. Figure 6-4(a) reports the measured IRF and DTOF curves (light and dark blue, respectively), with 1 second integration time. Time $t=0$ ps is defined as the IRF peak. As already seen in the phantom measurements, the IRF show a gaussian-like shape, without undesired “diffusion tails” at late times. Both the IRF and DTOF exhibit a high dynamic range (4 decades).

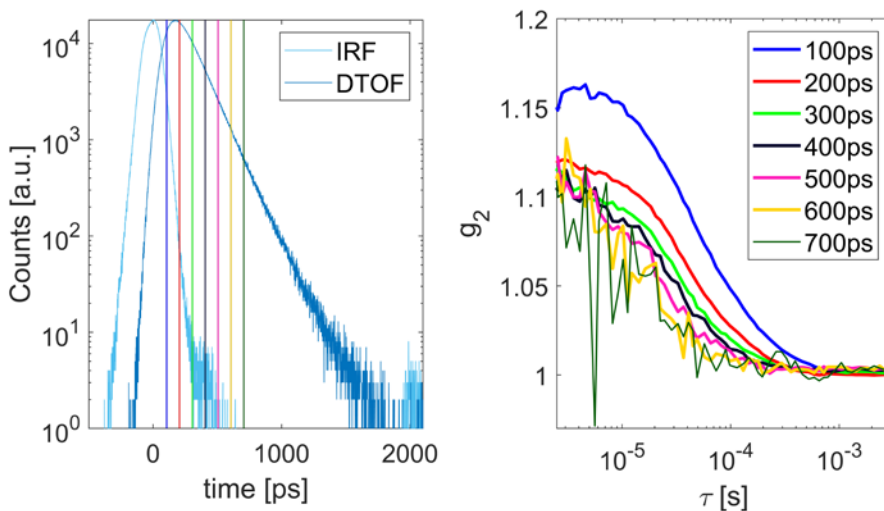


Figure 6-4: a) Measured IRF and DTOF curve on the forehead. The IRF show a gaussian-like shape, while both the curves have >4 decades dynamic range. The vertical lines denote the central time of the considered gates (200 ps width, 100 ps overlap). b) Intensity autocorrelation curves, for 7 different gate positions (see legend). The data suggests that the signal quality is sufficient for gates centred up to $t = 500-600$ ps.

The vertical lines denote the considered temporal gates (central time) in the computation of the autocorrelation functions. τ . All the gates have

¹⁰ Article #6 in the list of Publications

200ps duration, and 100ps overlap with the following one. Figure 6-4(b) shows the corresponding intensity autocorrelation functions, with 5 s integration time. As can be seen, the autocorrelations have a relatively high value of the coherence parameter β (0.1 – 0.15), and exhibit a sufficient signal quality for gates centred up to $t = 500 - 600$ ps. This initial characterization suggests that, due to the high SNR, it might be possible to measure the autocorrelations, and thus the BFI, at higher sampling rates. In particular, in the following a sampling rate of 10 Hz has been chosen. We will see that this enables to directly observe an interesting effect: the vascular pulsatility.

Vascular pulsatility: TD-DCS vs EKG

In order to extract a more robust BFI, broader temporal gates were considered: an early gate (centred at $t = 200$ ps), and a late gate (centred at $t = 650$ ps), both having a width of 500 ps. Also, ungated acquisition was considered (integrating the whole DTOF curve). Figure 6-5 reports the resulting *r*BFI temporal traces (normalized by their average value) for the three acquisition methods, with 10 Hz sampling.

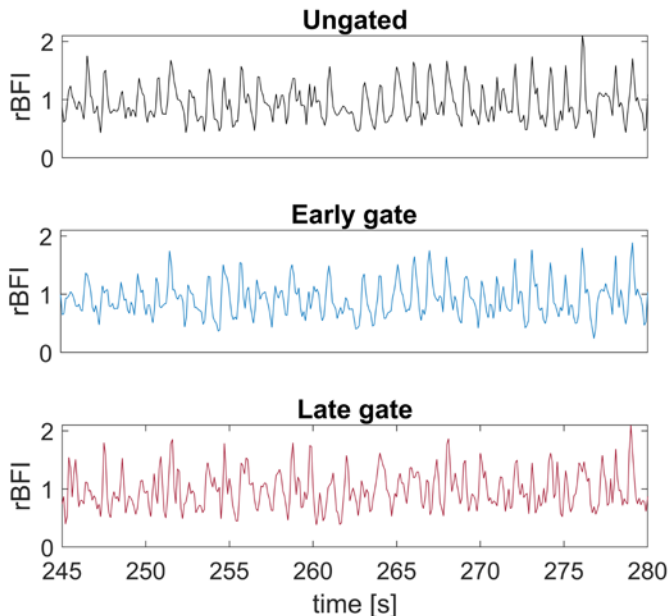


*Figure 6-5: Measured *r*BFI (BFI normalized to average) for ungated acquisition, early and late gate (upper, middle, and lower panels). The sampling rate is 10 Hz in all cases, without smoothing. In all three cases, vascular pulsatility is clearly visible.*

As can be seen from Figure 6-5, for all three acquisition methods the rBFI temporal traces show the fingerprint of vascular pulsatility, with a periodicity of approximately 1 Hz (60 beats/min). In order to confirm this, we have performed a Fourier analysis of the rBFI temporal traces acquired during the whole experiment (7 min) and compared it to PSD of the simultaneously measured electrocardiograph (EKG). Figure 6-6 shows the comparison of the BFI and EKG power spectral densities (PSD i.e., Fourier amplitude squared).

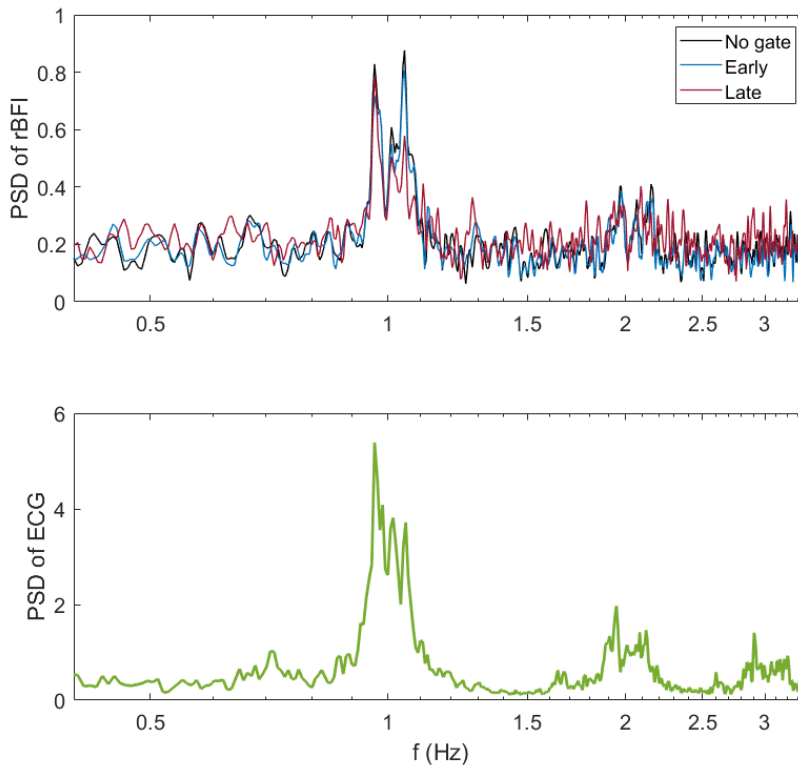


Figure 6-6: Comparison of the power spectral density (PSD) of the rBFI (ungated, early gate, and late gate) and the electrocardiograph (ECG) trace. Interestingly, the two spectra show a very similar shape around the 1 Hz region (corresponding to the heart-beat periodicity). The second harmonic (around 2 Hz) is also visible in both the modalities.

From Figure 6-6, it is interesting to see that the rBFI and EKG spectra show remarkably similar features around the 1 Hz region, which corresponds to the heart-beat periodicity. Also, the second harmonic

(around 2 Hz) is visible in both the modalities. This confirms that the observed oscillations are indeed due to heart-induced pulsatility. Additionally, while the Early gate trace is quite similar to the ungated one, the Late gate displays somehow different features.

Since this work is focalized more on the system development and validation (and the physics of the technique), I will not study these physiological aspects in detail. Rather, these phenomena could be thoroughly addressed in following works. In fact, the cerebrovascular pulsatility was shown to be tightly connected to the cerebral autoregulation, which is in turn important for the subject well-being. Thus, measuring accurately the cerebral pulsatility (disentangling it from the superficial contributions) might have a strong physiological and clinical impact.

To summarize, in this sub-section I have considered resting state experiments, and showed that it is possible to observe directly the vascular pulsatility in the TD-DCS data (obtaining results strongly correlated with EKG-related data). In the next sub-section, I will focus instead on a dynamic experiment, in particular reporting the results of breath hold measurements.

6.3.2. Breath hold experiment

In this Section, I will present an example of dynamic protocol: the breath hold experiment. The protocol of this experiment is described in Section 6.1.2, and is designed to induce a slight perturbation in the cerebral hemodynamics, by asking the subject to hold its breath for 20 seconds. As in the previous sub-section (Sec. 6.3.1), the Ti:Sapphire laser was used, together with the SNSPD detection system and the Swabian TCSPC module. The respiratory condition of the subject was verified with the breath rate (BR) sensor.

In Figure 6-7, I report the results of the experiment for one subject. The upper plot shows the rBFI time trace, normalized to the initial baseline, for ungated acquisition, early gate, and late gate. The three cyan rectangles denote the breath hold regions (20 seconds duration). The lower plot shows the chest/lungs volume (from the BR sensor) time trace, where higher values correspond to higher chest volumes (in

arbitrary units). The respiratory sensor confirms that the subject is actually holding its breath in all three repetitions.

As can be seen in Figure 6-7(b), in 2 out of 3 repetitions a rBFI increase is observed, starting from the middle/end of the breath hold period, probably for maintaining a constant oxygen supply in the tissues. The rBFI then goes back to the baseline value approximately 30 seconds after the end of the breath hold window. Interestingly, the rBFI response is significantly different for the early and late gate acquisition, with the ungated rBFI more similar to the early gate. This might indicate a different physiological response of the superficial (skin) and deeper (cerebral) layers. However, a higher number of subjects would be necessary to confirm this hypothesis.

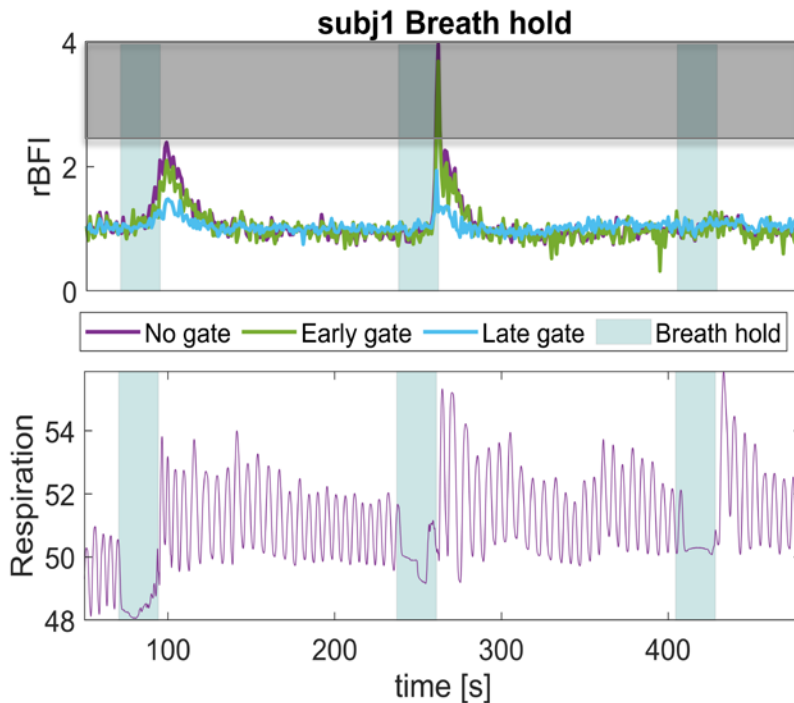


Figure 6-7: Breath hold experiment a) rBFI time trace for ungated (purple), early gate (green), and late gate (light blue) acquisition. All the data is normalized to the initial baseline condition. The three cyan rectangles denote the breath hold window (20 second duration each). b) Respiration time trace (from the BR sensor). The sensor returns a value proportional to the chest/lung volume. From this, it is possible to verify that the subject is actually holding the breath when requested by the examiner.

From this result, we might see that the system sensitivity is sufficiently high for detecting the induced physiological change, thanks to the high detection throughput. However, more systematic measurements would be needed to characterize the different layer's BFI response more accurately.

In conclusion, in this Section I have shown few examples of brain experiments, in particular focusing on resting state and breath hold protocols. The reported experiments showed the potentiality of the technique for detecting important physiological effects, which might be used to assess, for instance, cerebral autoregulation. Let me highlight that, by increasing the number of channels, it might be possible to improve even more the signal-to-noise ratio, and thus the system's sensitivity.

6.4. Experiments beyond the water peak

In this Section, I will present the results of *in vivo* experiments performed beyond the water absorption peak, in particular at $\lambda = 1000 \text{ nm}$. As we have already seen in Section 4.5, performing the experiments at longer wavelength might improve the depth sensitivity and the signal-to-noise ratio. Here, I will focus on cuff occlusion experiments, see Section 6.1.2, which were performed on $n=4$ adult subjects (30-53 years old, all male). The measurements were performed with the Ti:Sapphire laser, operated with the IR mirror set (see Section 3.2.1), the InGaAs photomultiplier detector (see Section 3.3), and the Picoquant TCSCP module (see Section 3.4.1) [170]¹¹.

6.4.1. Optical properties at longer wavelengths

Initially, the absorption (μ_a) and reduced scattering (μ'_s) coefficients were measured on the region of interest (brachioradialis muscle) with a broadband TD-DOS system [154], in the spectral region $680 \div 1030 \text{ nm}$. The results for each subject, together with the corresponding thickness of the superficial layer (measured with the plicometer), are reported in Figure 6-8. From the figure, two considerations arise. First of all, we can see that the absorption coefficient (upper plot) has a high

¹¹ Article #2 in the list of Publications.

inter-subject variability, probably due to the different superficial thickness (see legend). However, after the peak at approximately 970 nm due to water, the absorption coefficient sharply decreases to reasonably low values.

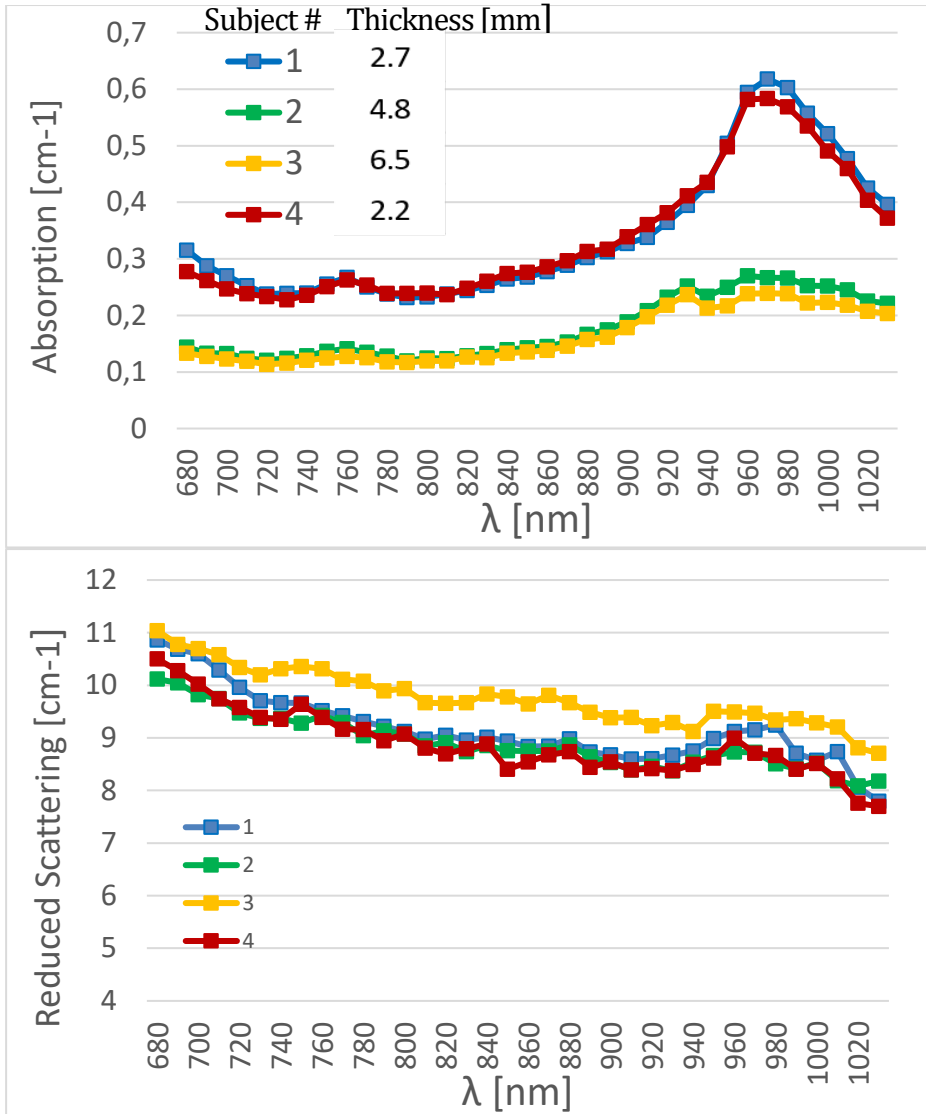


Figure 6-8: Absorption (μ_a) and reduced scattering (μ'_s) spectra (upper and lower plot respectively) for each subject, measured with a TD-DOS system.

Secondly, the reduced scattering (lower plot) also decreases when moving to longer wavelengths. The results are numerically summarized in Table 4. Based on these two considerations, the overall tissue attenuation at the longer wavelength appears to be similar to the one obtained at the typically used one.

Table 4: Superficial thickness and measured absorption and reduced scattering coefficients at 785 nm and 1000 nm.

| Subject | Superficial thickness [mm] | μ_a [cm ⁻¹] | μ'_s [cm ⁻¹] | μ_a | μ'_s |
|---------|----------------------------|-----------------------------|------------------------------|-----------|----------|
| | | @ 785 nm | | @ 1000 nm | |
| 1 | 2.7 | 0.24 | 9.3 | 0.52 | 7.7 |
| 2 | 4.8 | 0.13 | 9.4 | 0.25 | 7.9 |
| 3 | 6.5 | 0.12 | 10.4 | 0.22 | 8.9 |
| 4 | 2.2 | N/A | N/A | 0.49 | 7.8 |

6.4.2. Cuff occlusion experiments

After the optical properties' characterization, the actual cuff occlusion experiments were performed (see Section 6.1.2), at a wavelength $\lambda = 1000 \text{ nm}$ and a source-detection separation $\rho = 1 \text{ cm}$. For comparison, the same experiments were performed also at 785 nm using, instead of the InGaAs photomultiplier, the SPAD detector (see Section 3.3). Figure 6.8 shows the measured intensity and electric-field autocorrelations (red at 785 nm and blue at 1000 nm), for an Early and a Late gate, during baseline.

From Figure 6.8, similarly to the phantom experiments of Section 4.5, two important effects appear. First, an average increase of the β parameter (the amplitude of the intensity autocorrelation). In particular, the late gate value moves from 0.16 to 0.22. Secondly, a strong decrease of the electric-field autocorrelation (g_1) decay-rate, approximately 5-fold, is observed. This might improve the signal-to-noise ratio due to the higher correlation bin widths present at longer τ .

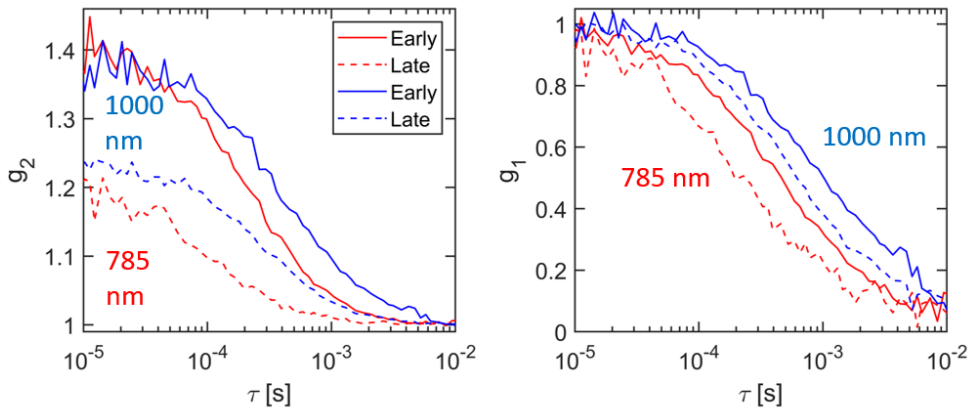


Figure 6-9: Comparison of the baseline intensity (g_2 , left plot) and electric-field (g_1 , right plot) autocorrelations, measured at 785 nm (red curves) and 1000 nm (blue curves), for Early and Late gate (continuous and dashed lines, respectively). The two main effects observed are: i) an increase of the late gate β and ii) an approximately 5-fold decrease of the de-correlation time (i.e., g_1 decay rate). All curves refer to subject #1.

After a quantitative analysis (see Section 6.1.3), Table 5 reports, for all the 4 subjects, the count rate and the BFI for Early gate, Late gate, and Ungated acquisition (all averaged over the baseline period). The results are compared with the Ungated BFI measured at 785 nm.

Table 5: Results of the cuff occlusion experiment (averaged over the baseline period). The first 4 columns report the count rate and BFI (early gate, late gate, and ungated acquisition) measured at 1000 nm. As comparison, the ungated BFI measured at 785 nm is also reported.

| Subject | Count rate [kcps] | BFI $\left[10^{-9} \frac{cm^2}{s}\right]$ @ 1000 nm | | | BFI @ 785 nm Ungated |
|---------|-------------------|-----------------------------------------------------|-----------------|-----------------|----------------------|
| | | Early | Late | Ungated | |
| 1 | 151 ± 3 | 3.1 ± 0.4 | 3.0 ± 0.4 | 3.0 ± 0.36 | 3.6 ± 0.38 |
| 2 | 263 ± 9 | 1.2 ± 0.24 | 1.3 ± 0.2 | 1.1 ± 0.2 | 0.74 ± 0.09 |
| 3 | 336 ± 7 | 0.63 ± 0.07 | 0.72 ± 0.06 | 0.59 ± 0.05 | 1.5 ± 0.13 |
| 4 | 112 ± 11 | 1.2 ± 0.25 | 1.3 ± 0.31 | 1.2 ± 0.2 | N/A |

As can be seen from Table 5, the count rate and baseline BFI appear to have a strong inter-subject variability, most probably due to different tissue properties (compare with Table 4). For all the subjects, the Early, Late gate, and Ungated BFI exhibit comparable values. This might be related to the relatively low superficial thickness of the considered subjects, which limits the discrimination of superficial and deeper hemodynamics. Let me highlight that the (Ungated) BFI appear to be different at the two wavelengths (785 nm and 1000 nm). Further studies would be necessary to elucidate the origin of this difference.

As a final result, in Figure 6-10 I report the time trace of the (absolute) BFI, measured at 1000 nm, for Early and Late gate (1 Hz sampling rate). From Figure 6-10, it might be seen that the BFI time traces have the expected temporal trend, for all the measured subjects. In particular, the occlusion and the hyperaemic peaks are clearly visible. In addition, the BFI hyperaemic peak (relative to baseline) show a large inter-subject variability, probably due to a different auto-regulatory response in each subject.

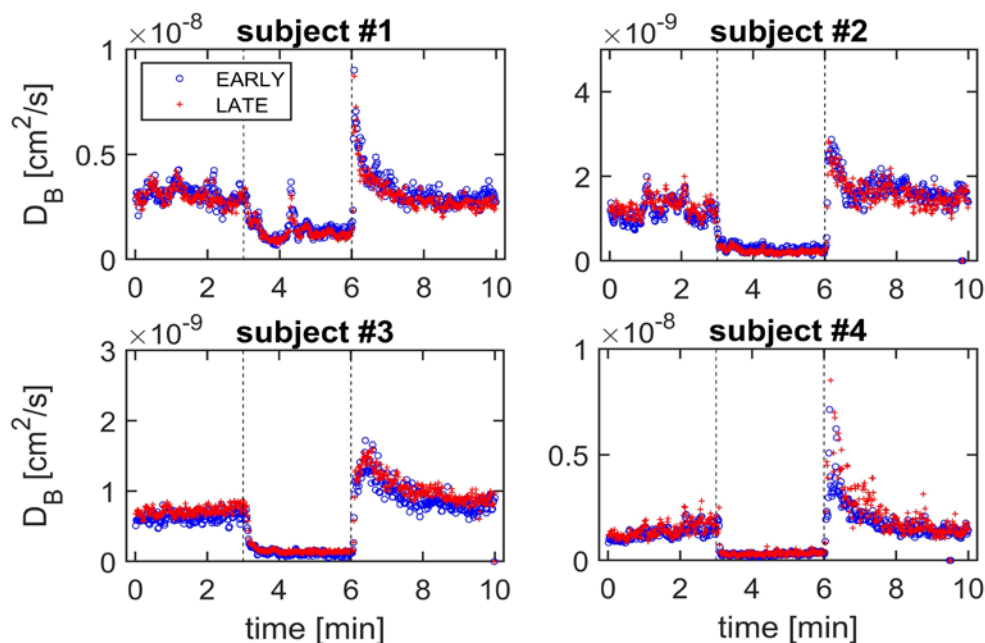


Figure 6-10: Cuff occlusion experiments BFI time traces, measured at 1000 nm, for all the 4 subjects (1 Hz sampling rate). Blue circles and red crosses refer to the Early and Late gate, respectively. Figure from Ref. [170].

In conclusion, the reported results demonstrate the feasibility and biomedical applicability of TD-DCS beyond the water absorption peak, here in particular at 1000 nm. This might be interesting also because of the larger availability of opto-electronic components in this spectral region. This might facilitate the development of more compact systems, with the potentiality of translating the technique towards clinical uses.

Summary

In summary, in this Chapter I have reported several *in vivo* TD-DCS experiments, for studying both muscle and brain hemodynamics. In addition, I have studied the feasibility of experiments in a longer spectral range (around 1 micron). These results might be helpful for the design and performance assessment of new TD-DCS systems, either in laboratory or clinical settings.

Conclusions

In this work, I contributed to lay the foundations of a novel diffuse optical technique, time-domain diffuse correlation spectroscopy (TD-DCS), both on the theoretical and experimental sides. In the following, I will briefly summarize the key achievements of this thesis work:

1. *Development and validation of a novel theoretical model*, which describes the effects of the instrument response function (IRF) and gate width. The model helped in providing physical insights regarding the impact of finite path length (i.e., temporal) resolution on the data, and to estimate in a more quantitative way the blood flow index (BFI).
See Chapter 2 and Chapter 3.
2. *Development and characterization of a versatile lab system*, through an evaluation and comparison of its main components (laser source, photodetectors, acquisition modules). In particular, I showed the impact of the individual components on the quality of the measurements. This was achieved by defining and characterizing suitable figures of merit, in particular the coherence parameter β and the accuracy of the BFI. Finally, I suitably integrated additional physiological sensors in the experimental system.
See Chapter 3 and Chapter 4.
3. *Observation and interpretation of the temporal speckle effect*. First, I presented the experimental evidence of this interesting phenomena, then I provided a simple theoretical interpretation, by adapting analysis approaches which were developed in other fields. Finally, I demonstrate the effect with an in vivo experiment. The observed effect was used successfully for the measurement of blood flow changes in a biomedical scenario.
See Chapter 5.

4. *Demonstration of in vivo experiments on human subjects.*
The first application I considered was a cuff occlusion experiment, which confirmed the suitability of the system to biomedical application. Then, I moved to experiments on the brain, focusing on two protocols: resting state and breath hold. This enabled to observe interesting physiological phenomena, such as vascular pulsatility. These *in vivo* experiments are one of the first reported in the TD-DCS literature.
See Chapter 6.

5. *In vivo experiments beyond the water absorption peak.*
Finally, I showed the feasibility of performing experiments in a novel spectral window, in particular beyond $1\ \mu\text{m}$. The experiments were performed both on tissue-mimicking phantoms and *in vivo*, on adult volunteers. For performing these experiments, I suitably modified the system (in particular the laser source) for operation in this spectral region.
See Chapter 4 and Chapter 6.

To summarize, with this thesis work I contributed to the foundations of TD-DCS, starting from the physics of the technique (points 1 and 3), and moving to the experimental and biomedical applications (points 2, 4 and 5). This work might provide crucial insights for the interpretation of the experimental data, but also help in the design and/or optimization of next generation, high-performance systems.

Regarding future developments, there are several interesting directions. First, the development of multi-channel systems. This might enable to increase dramatically the signal-to-noise ratio, and thus the accuracy and depth sensitivity of the technique. In addition, this might enable to obtain tomographic information of the tissue under study, with a strong impact on several biomedical applications. Second, the development of multi-wavelength systems, which might enable to extract in parallel both the BFI and the concentration of the main tissue constituents (as in diffuse optical spectroscopy/tomography). Last but not least, the development of real-time analysis software, which is crucial in several environments where the measurement is not easily repeatable.

In conclusion, let me highlight that the developed technique might be used not only for studying physiological effects, but also to study the pathophysiology. For instance, in clinical environments, the technique might help in the diagnosis and/or monitoring of several highly impacting diseases, such as cancer, stroke, or cognitive disorders.

Bibliography

- [1] Durduran, T., Choe, R., Baker, W. B., and Yodh, A. G., "Diffuse optics for tissue monitoring and tomography," *Reports Prog. Phys.* **73**, 076701 (2010), <http://dx.doi.org/10.1088/0034-4885/73/7/076701>.
- [2] Martelli, F., Bianco, S. del, Ismaelli, A., and Zaccanti, G., "Photon Migration Through Diffusive Media: Theory, Solutions, and Software," *Spie B.* **1365** (2010), <https://doi.org/10.1117/3.824746>.
- [3] Lorenzo, J. R., "Principles of Diffuse Light Propagation: Light Propagation in Tissues with Applications in Biology and Medicine", *World Scientific Publishing Co. Pte. Ltd.* (2012), <https://doi.org/10.1142/7609>.
- [4] Asllanaj, F., Contassot-Vivier, S., Hohmann, A., and Kienle, A., "Light propagation in biological tissue," *J. Quant. Spectrosc. Radiat. Transf.* **224**, (2019), <http://dx.doi.org/10.1016/j.jqsrt.2018.11.001>.
- [5] De Blasi, R. A., Ferrari, M., Natali, A., Conti, G., Mega, A., and Gasparetto, A., "Noninvasive measurement of forearm blood flow and oxygen consumption by near-infrared spectroscopy," *J. Appl. Physiol.* **76**, 1388–1393 (1994), <http://dx.doi.org/10.1152/jappl.1994.76.3.1388>.
- [6] Mesquita, R. C., Durduran, T., Yu, G., Buckley, E. M., Kim, M. N., Zhou, C., Choe, R., Sunar, U., and Yodh, A. G., "Direct measurement of tissue blood flow and metabolism with diffuse optics," *Philos. Trans. R. Soc. A Math. Phys. Eng. Sci.* (2011), <http://dx.doi.org/10.1098/rsta.2011.0232>.
- [7] Kim, M. N., Durduran, T., Frangos, S., Edlow, B. L., Buckley, E. M., Moss, H. E., Zhou, C., Yu, G., Choe, R., Maloney-Wilensky, E., Wolf, R. L., Grady, M. S., Greenberg, J. H., Levine, J. M., Yodh, A. G., Detre, J. A., and Kofke, W. A., "Noninvasive measurement of cerebral blood flow and blood oxygenation using near-infrared and diffuse correlation spectroscopies in critically brain-injured adults," *Neurocrit. Care* (2010), <http://dx.doi.org/10.1007/s12028-009-9305-x>.

Bibliography

- [8] Torricelli, A., Contini, D., Pifferi, A., Caffini, M., Re, R., Zucchelli, L., and Spinelli, L., "Time domain functional NIRS imaging for human brain mapping," *Neuroimage* (2014), <http://dx.doi.org/10.1016/j.neuroimage.2013.05.106>.
- [9] Pifferi, A., Farina, A., Torricelli, A., Quarto, G., Cubeddu, R., and Taroni, P., "Review: Time-domain broadband near infrared spectroscopy of the female breast: A focused review from basic principles to future perspectives," *J. Near Infrared Spectrosc.* 20, 223–235 (2012), <http://dx.doi.org/10.1255/jnirs.980>.
- [10] Scholkmann, F., Kleiser, S., Metz, A. J., Zimmermann, R., Mata Pavia, J., Wolf, U., and Wolf, M., "A review on continuous wave functional near-infrared spectroscopy and imaging instrumentation and methodology," *Neuroimage* 85, (2014), <http://dx.doi.org/10.1016/j.neuroimage.2013.05.004>.
- [11] Fantini, S. and Sassaroli, A., "Frequency-Domain Techniques for Cerebral and Functional Near-Infrared Spectroscopy," *Front. Neurosci.* 14, (2020), <http://dx.doi.org/10.3389/fnins.2020.00300>.
- [12] Gioux, S., Mazhar, A., and Cuccia, D. J., "Spatial frequency domain imaging in 2019: principles, applications, and perspectives," *J. Biomed. Opt.* 24, (2019), <http://dx.doi.org/10.1117/1.jbo.24.7.071613>.
- [13] Jöbsis, F. F., "Noninvasive, infrared monitoring of cerebral and myocardial oxygen sufficiency and circulatory parameters," *Science* (80-.). 198, (1977), <http://dx.doi.org/10.1126/science.929199>.
- [14] Hallacoglu, B., "Absolute measurement of cerebral optical coefficients, hemoglobin concentration and oxygen saturation in old and young adults with near-infrared spectroscopy," *J. Biomed. Opt.* 17, (2012), <http://dx.doi.org/10.1117/1.jbo.17.8.081406>.
- [15] Pifferi, A., Contini, D., Mora, A. D., Farina, A., Spinelli, L., Torricelli, A., Dalla Mora, A., Farina, A., Spinelli, L., Torricelli, A., Mora, A. D., Farina, A., Spinelli, L., and Torricelli, A., "New frontiers in time-domain diffuse optics, a review," *J. Biomed. Opt.* 21, 091310 (2016), <http://dx.doi.org/10.1117/1.jbo.21.9.091310>.
- [16] Lange, F. and Tachtsidis, I., "Clinical brain monitoring with time domain NIRS: A review and future perspectives," *Appl. Sci.* 9, (2019), <http://dx.doi.org/10.3390/app9081612>.

Bibliography

- [17] Yamada, Y., Suzuki, H., and Yamashita, Y., "Time-domain near-infrared spectroscopy and imaging: A review," *Appl. Sci.* **9**, (2019), <http://dx.doi.org/10.3390/app9061127>.
- [18] Martelli, F., Binzoni, T., Pifferi, A., Spinelli, L., Farina, A., and Torricelli, A., "There's plenty of light at the bottom: Statistics of photon penetration depth in random media," *Sci. Rep.* **6**, (2016), <http://dx.doi.org/10.1038/srep27057>.
- [19] Mora, A. D., Contini, D., Arridge, S., Martelli, F., Tosi, A., Boso, G., Farina, A., Durduran, T., Martinenghi, E., Torricelli, A., and Pifferi, A., "Towards next-generation time-domain diffuse optics for extreme depth penetration and sensitivity," *Biomed. Opt. Express* (2015), <http://dx.doi.org/10.1364/boe.6.001749>.
- [20] Goodman, J. W., "Statistical properties of laser speckle patterns," in (1975), <http://dx.doi.org/10.1007/bfb0111436>.
- [21] Goodman, J. W., "Some Effects of Target-Induced Scintillation on Optical Radar Performance," *Proc. IEEE* (1965), <http://dx.doi.org/10.1109/PROC.1965.4341>.
- [22] Mounaix, M., Defienne, H., and Gigan, S., "Deterministic light focusing in space and time through multiple scattering media with a time-resolved transmission matrix approach," *Phys. Rev. A* (2016), <http://dx.doi.org/10.1103/PhysRevA.94.041802>.
- [23] Bellini, T., Glaser, M. A., Clark, N. A., and Degiorgio, V., "Effects of finite laser coherence in quasielastic multiple scattering," *Phys. Rev. A* **44**, 5215–5223 (1991), <http://dx.doi.org/10.1103/PhysRevA.44.5215>.
- [24] Senarathna, J., Rege, A., Li, N., and Thakor, N. V., "Laser speckle contrast imaging: Theory, instrumentation and applications," *IEEE Rev. Biomed. Eng.* (2013), <http://dx.doi.org/10.1109/RBME.2013.2243140>.
- [25] Basak, K., Manjunatha, M., and Dutta, P. K., "Review of laser speckle-based analysis in medical imaging," *Med. Biol. Eng. Comput.* (2012), <http://dx.doi.org/10.1007/s11517-012-0902-z>.
- [26] Vaz, P. G., Humeau-Heurtier, A., Figueiras, E., Correia, C., and Cardoso, J., "Laser Speckle Imaging to Monitor Microvascular Blood Flow: A Review," *IEEE Rev. Biomed. Eng.* **9**, 106–120 (2016), <http://dx.doi.org/10.1109/RBME.2016.2532598>.

Bibliography

- [27] Rajan, V., Varghese, B., Van Leeuwen, T. G., and Steenbergen, W., "Review of methodological developments in laser Doppler flowmetry," *Lasers Med. Sci.* 24, (2009), <http://dx.doi.org/10.1007/s10103-007-0524-0>.
- [28] Briers, J. D., "Laser Doppler, speckle and related techniques for blood perfusion mapping and imaging," *Physiol. Meas.* 22, (2001), <http://dx.doi.org/10.1088/0967-3334/22/4/201>.
- [29] Dunn, A. K., Devor, A., Bolay, H., Andermann, M. L., Moskowitz, M. A., Dale, A. M., and Boas, D. A., "Simultaneous imaging of total cerebral hemoglobin concentration, oxygenation, and blood flow during functional activation," *Opt. Lett.* 28, (2003), <http://dx.doi.org/10.1364/ol.28.000028>.
- [30] Gonik, M. M., Mishin, A. B., and Zimnyakov, D. A., "Visualization of blood microcirculation parameters in human tissues by time-integrated dynamic speckles analysis," in *Annals of the New York Academy of Sciences* (2002), <http://dx.doi.org/10.1111/j.1749-6632.2002.tb04591.x>.
- [31] Valdes, C. P., Varma, H. M., Kristoffersen, A. K., Dragojevic, T., Culver, J. P., and Durduran, T., "Speckle contrast optical spectroscopy, a non-invasive, diffuse optical method for measuring microvascular blood flow in tissue," *Biomed. Opt. Express* 5, 2769 (2014), <http://dx.doi.org/10.1364/BOE.5.002769>.
- [32] Lee, K., "Diffuse speckle contrast analysis (DSCA) for deep tissue blood flow monitoring," *Adv. Biomed. Eng.* 9, (2020), <http://dx.doi.org/10.14326/abe.9.21>.
- [33] Bi, R., Du, Y., Singh, G., Ho, J.-H., Zhang, S., Ebrahim Attia, A. B., Li, X., and Olivo, M. C., "Fast pulsatile blood flow measurement in deep tissue through a multimode detection fiber," *J. Biomed. Opt.* (2020), <http://dx.doi.org/10.1117/1.jbo.25.5.055003>.
- [34] Parthasarathy, A. B., James Tom, W., Gopal, A., Zhang, X., Dunn, A. K., Durduran, T., Burnett, M., Yu, G., Zhou, C., Furuya, D., Yodh, A., Detre, J., Greenberg, J., Atochin, D., Murciano, J., GURSOY-OZDEMIR, Y., KRASIK, T., NODA, F., AYATA, C., DUNN, A., MOSKOWITZ, M., HUANG, P., MUZYKANTOV, V., ANDERSON, J., CHIU, D., JACKMAN, R., CHERNIAVSKAYA, O., McDONALD, J., WU, H., WHITESIDES, S., and WHITESIDES, G., "Robust flow measurement with multi-exposure speckle imaging Quantification of Cerebral Blood Flow During Functional Activation in Rat Somatosensory Cortex Using Laser- Speckle Flowmetry," *J. Cereb. Blood Flow Metab. OSA Opt. EXPRESS* (2004).

Bibliography

- [35] Brady, K. M., Lee, J. K., Kibler, K. K., Smielewski, P., Czosnyka, M., Easley, R. B., Koehler, R. C., and Shaffner, D. H., "Continuous time-domain analysis of cerebrovascular autoregulation using near-infrared spectroscopy," *Stroke* (2007), <http://dx.doi.org/10.1161/STROKEAHA.107.485706>.
- [36] Goadsby, P. J. and Edvinsson, L., "The trigeminovascular system and migraine: Studies characterizing cerebrovascular and neuropeptide changes seen in humans and cats," *Ann. Neurol.* 33, (1993), <http://dx.doi.org/10.1002/ana.410330109>.
- [37] Huang, Z., Huang, P. L., Ma, J., Meng, W., Ayata, C., Fishman, M. C., and Moskowitz, M. A., "Enlarged infarcts in endothelial nitric oxide synthase knockout mice are attenuated by nitro-L-arginine," *J. Cereb. Blood Flow Metab.* 16, (1996), <http://dx.doi.org/10.1097/00004647-199609000-00023>.
- [38] Fredriksson, I. and Larsson, M., "On the equivalence and differences between laser Doppler flowmetry and laser speckle contrast analysis," *J. Biomed. Opt.* (2016), <http://dx.doi.org/10.1117/1.jbo.21.12.126018>.
- [39] Humeau-Heurtier, A., Mahe, G., Durand, S., and Abraham, P., "Skin perfusion evaluation between laser speckle contrast imaging and laser Doppler flowmetry," *Opt. Commun.* 291, (2013), <http://dx.doi.org/10.1016/j.optcom.2012.11.054>.
- [40] Binzoni, T., Humeau-Heurtier, A., Abraham, P., and Mahe, G., "Blood perfusion values of laser speckle contrast imaging and laser doppler flowmetry: Is a direct comparison possible?," *IEEE Trans. Biomed. Eng.* 60, (2013), <http://dx.doi.org/10.1109/TBME.2012.2232294>.
- [41] Omarjee, L., Larralde, A., Jaquinandi, V., Stivalet, O., and Mahe, G., "Performance of noninvasive laser Doppler flowmetry and laser speckle contrast imaging methods in diagnosis of Buerger disease: A case report," *Med. (United States)* 97, (2018), <http://dx.doi.org/10.1097/MD.00000000000012979>.
- [42] Puissant, C., Abraham, P., Durand, S., Humeau-Heurtier, A., Faure, S., Lefthériotis, G., Rousseau, P., and Mahé, G., "Reproducibility of Non-Invasive Assessment of Skin Endothelial Function Using Laser Doppler Flowmetry and Laser Speckle Contrast Imaging," *PLoS One* 8, (2013), <http://dx.doi.org/10.1371/journal.pone.0061320>.
- [43] Weitz, D. A., Gang, H., Pine, D. J., Zhu, J. X., and Durian, D. J., "Diffusing-wave spectroscopy: The technique and some applications," *Phys. Scr.*

Bibliography

- (1993), <http://dx.doi.org/10.1088/0031-8949/1993/T49B/040>.
- [44] Weitz, D. A., Pine, D. J., Pusey, P. N., and Tough, R. J. A., "Nondiffusive Brownian motion studied by diffusing-wave spectroscopy," *Phys. Rev. Lett.* (1989), <http://dx.doi.org/10.1103/PhysRevLett.63.1747>.
- [45] Boas, D. A. and Yodh, A. G., "Spatially varying dynamical properties of turbid media probed with diffusing temporal light correlation," *J. Opt. Soc. Am. A* 14, 192–215 (1997), <http://dx.doi.org/10.1364/josaa.14.000192>.
- [46] Boas, D. A., Campbell, L. E., and Yodh, A. G., "Scattering and Imaging with Diffusing Temporal Field Correlations," *Phys. Rev. Lett.* 75, 1855–1858 (1995), <http://dx.doi.org/10.1103/PhysRevLett.75.1855>.
- [47] Yu, G., Floyd, T. F., Durduran, T., Zhou, C., Wang, J., Detre, J. A., and Yodh, A. G., "Validation of diffuse correlation spectroscopy for muscle blood flow with concurrent arterial spin labeled perfusion MRI," *Opt. Express* (2007), <http://dx.doi.org/10.1364/OE.15.001064>.
- [48] Durduran, T., Yu, G., Burnett, M. G., Detre, J. A., Greenberg, J. H., Wang, J., Zhou, C., and Yodh, A. G., "Diffuse optical measurement of blood flow, blood oxygenation, and metabolism in a human brain during sensorimotor cortex activation," *Opt. Lett.* 29, 1766 (2004), <http://dx.doi.org/10.1364/ol.29.001766>.
- [49] Yu, G., "Near-infrared diffuse correlation spectroscopy in cancer diagnosis and therapy monitoring," *J. Biomed. Opt.* (2012), <http://dx.doi.org/10.1117/1.jbo.17.1.010901>.
- [50] Li, Z., Baker, W. B., Parthasarathy, A. B., Ko, T. S., Wang, D., Schenkel, S., Durduran, T., Li, G., and Yodh, A. G., "Calibration of diffuse correlation spectroscopy blood flow index with venous-occlusion diffuse optical spectroscopy in skeletal muscle," *J. Biomed. Opt.* (2015), <http://dx.doi.org/10.1117/1.jbo.20.12.125005>.
- [51] Boas, D. A., Sakadžić, S., Selb, J., Farzam, P., Franceschini, M. A., and Carp, S. A., "Establishing the diffuse correlation spectroscopy signal relationship with blood flow," *Neurophotonics* 3, 031412 (2016), <http://dx.doi.org/10.1117/1.nph.3.3.031412>.
- [52] Mason, T. G., Gang, H., and Weitz, D. A., "Diffusing-wave-spectroscopy measurements of viscoelasticity of complex fluids," *J. Opt. Soc. Am. A* (1997), <http://dx.doi.org/10.1364/josaa.14.000139>.

Bibliography

- [53] Palmer, A., Mason, T. G., Xu, J., Kuo, S. C., and Wirtz, D., "Diffusing wave spectroscopy microrheology of actin filament networks," *Biophys. J.* (1999), [http://dx.doi.org/10.1016/S0006-3495\(99\)77271-1](http://dx.doi.org/10.1016/S0006-3495(99)77271-1).
- [54] Galvan-Miyoshi, J., Delgado, J., and Castillo, R., "Diffusing wave spectroscopy in Maxwellian fluids," *Eur. Phys. J. E* (2008), <http://dx.doi.org/10.1140/epje/i2007-10335-8>.
- [55] Dragojević, T., Hollmann, J. L., Tamborini, D., Portaluppi, D., Buttafava, M., Culver, J. P., Villa, F., and Durduran, T., "Compact, multi-exposure speckle contrast optical spectroscopy (SCOS) device for measuring deep tissue blood flow," *Biomed. Opt. Express* 9, 322 (2018), <http://dx.doi.org/10.1364/BOE.9.000322>.
- [56] Postnov, D., Tang, J., Erdener, S. E., Kılıç, K., and Boas, D., "Dynamic Laser Speckle Imaging," *bioRxiv* 2, 626515 (2019), <http://dx.doi.org/10.1101/626515>.
- [57] Rice, T. B., Kwan, E., Hayakawa, C. K., Durkin, A. J., Choi, B., and Tromberg, B. J., "Quantitative, depth-resolved determination of particle motion using multi-exposure, spatial frequency domain laser speckle imaging," *Biomed. Opt. Express* (2013), <http://dx.doi.org/10.1364/boe.4.002880>.
- [58] Dragojević, T., Bronzi, D., Varma, H. M., Valdes, C. P., Castellvi, C., Villa, F., Tosi, A., Justicia, C., Zappa, F., and Durduran, T., "High-speed multi-exposure laser speckle contrast imaging with a single-photon counting camera," *Biomed. Opt. Express* 6, 2865 (2015), <http://dx.doi.org/10.1364/BOE.6.002865>.
- [59] Varma, H. M., Valdes, C. P., Kristoffersen, A. K., Culver, J. P., and Durduran, T., "Speckle contrast optical tomography: A new method for deep tissue three-dimensional tomography of blood flow," *Biomed. Opt. Express* 5, (2014), <http://dx.doi.org/10.1364/BOE.5.001275>.
- [60] Giovannella, M., Spinelli, L., Pagliuzzi, M., Contini, D., Greisen, G., Weigel, U. M., Torricelli, A., and Durduran, T., "Accuracy and precision of tissue optical properties and hemodynamic parameters estimated by the BabyLux device: a hybrid time-resolved near-infrared and diffuse correlation spectroscopy neuro-monitor," *Biomed. Opt. Express* 10, 2556 (2019), <http://dx.doi.org/10.1364/BOE.10.002556>.
- [61] Durian, D. J., "Accuracy of diffusing-wave spectroscopy theories," *Phys. Rev. E* (1995), <http://dx.doi.org/10.1103/PhysRevE.51.3350>.

- [62] Verdecchia, K., Diop, M., Lee, T.-Y., and St. Lawrence, K., "Quantifying the cerebral metabolic rate of oxygen by combining diffuse correlation spectroscopy and time-resolved near-infrared spectroscopy," *J. Biomed. Opt.* (2013), <http://dx.doi.org/10.1117/1.jbo.18.2.027007>.
- [63] Zhang, S., Chen, S., Liu, Y., Liu, Y., and Tan, Z., "Effects of tissue surface curvature and incident light angle on diffuse correlation spectroscopy," *J. Mod. Opt.* *66*, (2019), <http://dx.doi.org/10.1080/09500340.2018.1512670>.
- [64] Tamborini, D., Farzam, P., Zimmermann, B., Wu, K.-C., Boas, D. A., and Franceschini, M. A., "Development and characterization of a multidistance and multiwavelength diffuse correlation spectroscopy system," *Neurophotonics* (2017), <http://dx.doi.org/10.1117/1.nph.5.1.011015>.
- [65] Farzam, P. and Durduran, T., "Multidistance diffuse correlation spectroscopy for simultaneous estimation of absolute scattering and absorption coefficient and the blood flow index," *J. Biomed. Opt.* (2015), <http://dx.doi.org/10.1117/1.JBO.20.5.055001>.
- [66] Selb, J., Boas, D. A., Chan, S.-T., Evans, K. C., Buckley, E. M., and Carp, S. A., "Sensitivity of near-infrared spectroscopy and diffuse correlation spectroscopy to brain hemodynamics: simulations and experimental findings during hypercapnia," *Neurophotonics* *1*, (2014), <http://dx.doi.org/10.1117/1.nph.1.1.015005>.
- [67] Gagnon, L., Desjardins, M., Jehanne-Lacasse, J., Bherer, L., and Lesage, F., "Investigation of diffuse correlation spectroscopy in multi-layered media including the human head," *Opt. Express* *16*, 15514 (2008), <http://dx.doi.org/10.1364/oe.16.015514>.
- [68] Jaillon, F., Li, J., Dietsche, G., Elbert, T., and Gisler, T., "Activity of the human visual cortex measured non-invasively by diffusing-wave spectroscopy," *Opt. Express* *15*, 6643 (2007), <http://dx.doi.org/10.1364/OE.15.006643>.
- [69] Verdecchia, K., Diop, M., Lee, A., Morrison, L. B., Lee, T.-Y., and St. Lawrence, K., "Assessment of a multi-layered diffuse correlation spectroscopy method for monitoring cerebral blood flow in adults," *Biomed. Opt. Express* *7*, 3659 (2016), <http://dx.doi.org/10.1364/boe.7.003659>.
- [70] Yodh, A. G., Kaplan, P. D., and Pine, D. J., "Pulsed diffusing-wave spectroscopy: High resolution through nonlinear optical gating," *Phys. Rev. B* *42*, 4744–4747 (1990), <http://dx.doi.org/10.1103/PhysRevB.42.4744>.

Bibliography

- [71] Bizheva, K. K., Siegel, A. M., and Boas, D. A., "Path-length-resolved dynamic light scattering in highly scattering random media: The transition to diffusing wave spectroscopy," *Phys. Rev. E* **58**, 7664–7667 (1998), <http://dx.doi.org/10.1103/PhysRevE.58.7664>.
- [72] Borycki, D., Kholiqov, O., and Srinivasan, V. J., "Reflectance-mode interferometric near-infrared spectroscopy quantifies brain absorption, scattering, and blood flow index in vivo," *Opt. Lett.* **42**, 591 (2017), <http://dx.doi.org/10.1364/OL.42.000591>.
- [73] Tualle, J.-M., Nghiem, H. L., Cheikh, M., Ettori, D., Tinet, E., and Avrillier, S., "Time-resolved diffusing wave spectroscopy beyond 300 transport mean free paths," *J. Opt. Soc. Am. A* **23**, 1452 (2006), <http://dx.doi.org/10.1364/JOSAA.23.001452>.
- [74] Boas, D. A., Bizheva, K. K., and Siegel, A. M., "Using dynamic low-coherence interferometry to image Brownian motion within highly scattering media," *Opt. Lett.* **23**, (1998), <http://dx.doi.org/10.1364/ol.23.000319>.
- [75] Tualle, J.-M., Tinet, E., and Avrillier, S., "A new and easy way to perform time-resolved measurements of the light scattered by a turbid medium," *Opt. Commun.* **189**, 211–220 (2001), [http://dx.doi.org/10.1016/S0030-4018\(01\)01045-8](http://dx.doi.org/10.1016/S0030-4018(01)01045-8).
- [76] Tualle, J.-M., Nghiem, H. L., Schäfauer, C., Berthaud, P., Tinet, E., Ettori, D., and Avrillier, S., "Time-resolved measurements from speckle interferometry," *Opt. Lett.* (2005), <http://dx.doi.org/10.1364/ol.30.000050>.
- [77] Borycki, D., Kholiqov, O., Chong, S. P., and Srinivasan, V. J., "Interferometric Near-Infrared Spectroscopy (iNIRS) for determination of optical and dynamical properties of turbid media," *Opt. Express* (2016), <http://dx.doi.org/10.1364/oe.24.000329>.
- [78] Sutin, J., Zimmerman, B., Tyulmankov, D., Tamborini, D., Wu, K. C., Selb, J., Gulinatti, A., Rech, I., Tosi, A., Boas, D. A., and Franceschini, M. A., "Time-domain diffuse correlation spectroscopy," *Optica* **3**, 1006 (2016), <http://dx.doi.org/10.1364/optica.3.001006>.
- [79] Pagliuzzi, M., Sekar, S. K. V., Colombo, L., Martinenghi, E., Minnema, J., Erdmann, R., Contini, D., Mora, A. D., Torricelli, A., Pifferi, A., and Durduran, T., "Time domain diffuse correlation spectroscopy with a high coherence pulsed source: in vivo and phantom results," *Biomed. Opt. Express* **8**, 5311 (2017), <http://dx.doi.org/10.1364/boe.8.005311>.

Bibliography

- [80] Pagliazzi, M., Sekar, S. K. V., Di Sieno, L., Colombo, L., Durduran, T., Contini, D., Torricelli, A., Pifferi, A., Mora, A. D., Konugolu Venkata Sekar, S., Di Sieno, L., Colombo, L., Durduran, T., Contini, D., Torricelli, A., Pifferi, A., Mora, A. D., Sekar, S. K. V., Di Sieno, L., Colombo, L., Durduran, T., Contini, D., Torricelli, A., Pifferi, A., and Mora, A. D., "In vivo time-gated diffuse correlation spectroscopy at quasi-null source-detector separation," *Opt. Lett.* **43**, 2450 (2018), <http://dx.doi.org/10.1364/ol.43.002450>.
- [81] Contini, D., Spinelli, L., Torricelli, A., Pifferi, A., and Cubeddu, R., "Novel method for depth-resolved brain functional imaging by timedomain NIRS," *Opt. InfoBase Conf. Pap.* **6629**, 1–7 (2007), <http://dx.doi.org/10.1117/12.728104>.
- [82] Del Bianco, S., Martelli, F., and Zaccanti, G., "Penetration depth of light re-emitted by a diffusive medium: Theoretical and experimental investigation," *Phys. Med. Biol.* **47**, 4131–4144 (2002), <http://dx.doi.org/10.1088/0031-9155/47/23/301>.
- [83] Mazurenka, M., Jelzow, A., Wabnitz, H., Contini, D., Spinelli, L., Pifferi, A., Cubeddu, R., Mora, A. D., Tosi, A., Zappa, F., and Macdonald, R., "Non-contact time-resolved diffuse reflectance imaging at null source-detector separation," *Opt. Express* **20**, 283 (2012), <http://dx.doi.org/10.1364/oe.20.000283>.
- [84] Mora, A. D., Sieno, L. Di, Re, R., Pifferi, A., and Contini, D., "Time-Gated single-photon detection in time-domain diffuse optics: A review," *Appl. Sci.* **10**, (2020), <http://dx.doi.org/10.3390/app10031101>.
- [85] Irwin, D., Dong, L., Shang, Y., Cheng, R., Kudrimoti, M., Stevens, S. D., and Yu, G., "Influences of tissue absorption and scattering on diffuse correlation spectroscopy blood flow measurements," *Biomed. Opt. Express* (2011), <http://dx.doi.org/10.1364/boe.2.001969>.
- [86] Durduran, T., "Noninvasive measurements of tissue hemodynamics with hybrid diffuse optical methods," *Med. Phys.* **31**, 2178 (2004), <http://dx.doi.org/10.1118/1.1763412>.
- [87] Yu, G., Durduran, T., Lech, G., Zhou, C., Chance, B., Mohler, E. R., and Yodh, A. G., "Time-dependent blood flow and oxygenation in human skeletal muscles measured with noninvasive near-infrared diffuse optical spectroscopies," *J. Biomed. Opt.* (2005), <http://dx.doi.org/10.1117/1.1884603>.

Bibliography

- [88] Bellini, M., Lynga, C., Tozzi, A., Gaarde, M. B., Hansch, T. W., L'Huillier, A., and Wahlstrom, C. G., "Temporal coherence of ultrashort high-order harmonic pulses," *Conf. Lasers Electro-Optics Eur. - Tech. Dig.* 337 (1998).
- [89] Cheng, X., Tamborini, D., Carp, S. A., Shatrovov, O., Zimmerman, B., Tyulmankov, D., Siegel, A., Blackwell, M., Franceschini, M. A., and Boas, D. A., "Time domain diffuse correlation spectroscopy: modeling the effects of laser coherence length and instrument response function," *Opt. Lett.* 43, 2756 (2018), <http://dx.doi.org/10.1364/ol.43.002756>.
- [90] Tamborini, D., Stephens, K., Wu, M., Farzam, P., Siegel, A., Shatrovov, O., Blackwell, M., Boas, D., Carp, S., and Franceschini, M. A., "Portable system for Time-Domain Diffuse Correlation Spectroscopy," *IEEE Trans. Biomed. Eng.* 66, 3014 (2019), <http://dx.doi.org/10.1109/tbme.2019.2899762>.
- [91] McKinney, J. D., Webster, M. A., Webb, K. J., and Weiner, A. M., "Characterization and imaging in optically scattering media by use of laser speckle and a variable-coherence source," *Opt. Lett.* (2000), <http://dx.doi.org/10.1364/ol.25.000004>.
- [92] Curry, N., Bondareff, P., Leclercq, M., van Hulst, N. F., Sapienza, R., Gigan, S., and Grésillon, S., "Direct determination of diffusion properties of random media from speckle contrast," *Opt. Lett.* (2011), <http://dx.doi.org/10.1364/ol.36.003332>.
- [93] Gisler, T., Rürger, H., Egelhaaf, S. U., Tschumi, J., Schurtenberger, P., and Rička, J., "Mode-selective dynamic light scattering: theory versus experimental realization," *Appl. Opt.* (1995), <http://dx.doi.org/10.1364/ao.34.003546>.
- [94] Zhou, C., Yu, G., Furuya, D., Greenberg, J. H., Yodh, A. G., and Durduran, T., "Diffuse optical correlation tomography of cerebral blood flow during cortical spreading depression in rat brain," *Opt. Express* 14, 1125–1144 (2006), <http://dx.doi.org/10.1364/oe.14.001125>.
- [95] Dietsche, G., Ninck, M., Ortoft, C., Li, J., Jaillon, F., and Gisler, T., "Fiber-based multispeckle detection for time-resolved diffusing-wave spectroscopy: Characterization and application to blood flow detection in deep tissue," *Appl. Opt.* 46, 8506–8514 (2007), <http://dx.doi.org/10.1364/AO.46.008506>.
- [96] Zhou, W., Kholiqov, O., Chong, S. P., and Srinivasan, V. J., "Highly parallel, interferometric diffusing wave spectroscopy for monitoring cerebral blood

Bibliography

- flow dynamics," *Optica* 5, 518 (2018),
<http://dx.doi.org/10.1364/optica.5.000518>.
- [97] Robinson, M. B., Boas, D. A., Sakadzic, S., Franceschini, M. A., and Carp, S. A., "Interferometric diffuse correlation spectroscopy improves measurements at long source–detector separation and low photon count rate," *J. Biomed. Opt.* 25, (2020),
<http://dx.doi.org/10.1117/1.jbo.25.9.097004>.
- [98] Boas, D. A., Pitris, C., and Ramanujam, N., *Handbook of Biomedical Optics* (2016).
- [99] Buckley, E. M., Cook, N. M., Durduran, T., Kim, M. N., Zhou, C., Choe, R., Yu, G., Schultz, S., Sehgal, C. M., Licht, D. J., Arger, P. H., Putt, M. E., Hurt, H. H., and Yodh, A. G., "Cerebral hemodynamics in preterm infants during positional intervention measured with diffuse correlation spectroscopy and transcranial Doppler ultrasound," *Opt. Express* 17, (2009),
<http://dx.doi.org/10.1364/oe.17.012571>.
- [100] Favilla, C. G., Mesquita, R. C., Mullen, M., Durduran, T., Lu, X., Kim, M. N., Minkoff, D. L., Kasner, S. E., Greenberg, J. H., Yodh, A. G., and Detre, J. A., "Optical bedside monitoring of cerebral blood flow in acute ischemic stroke patients during head-of-bed manipulation," *Stroke* 45, (2014),
<http://dx.doi.org/10.1161/STROKEAHA.113.004116>.
- [101] Bangalore-Yogananda, C.-G., Rosenberry, R., Soni, S., Liu, H., Nelson, M. D., and Tian, F., "Concurrent measurement of skeletal muscle blood flow during exercise with diffuse correlation spectroscopy and Doppler ultrasound," *Biomed. Opt. Express* 9, (2018),
<http://dx.doi.org/10.1364/boe.9.000131>.
- [102] Yu, G., Durduran, T., Zhou, C., Wang, H. W., Putt, M. E., Saunders, H. M., Sehgal, C. M., Glatstein, E., Yodh, A. G., and Busch, T. M., "Noninvasive monitoring of murine tumor blood flow during and after photodynamic therapy provides early assessment of therapeutic efficacy," *Clin. Cancer Res.* 11, (2005), <http://dx.doi.org/10.1158/1078-0432.CCR-04-2582>.
- [103] Durduran, T., Zhou, C., Buckley, E. M., Kim, M. N., Yu, G., Choe, R., Gaynor, J. W., Spray, T. L., Durning, S. M., Mason, S. E., Montenegro, L. M., Nicolson, S. C., Zimmerman, R. A., Putt, M. E., Wang, J., Greenberg, J. H., Detre, J. A., Yodh, A. G., and Licht, D. J., "Optical measurement of cerebral hemodynamics and oxygen metabolism in neonates with congenital heart defects," *J. Biomed. Opt.* 15, (2010), <http://dx.doi.org/10.1117/1.3425884>.

Bibliography

- [104] Carp, S. A., Dai, G. P., Boas, D. A., Franceschini, M. A., and Kim, Y. R., "Validation of diffuse correlation spectroscopy measurements of rodent cerebral blood flow with simultaneous arterial spin labeling MRI; towards MRI-optical continuous cerebral metabolic monitoring," *Biomed. Opt. Express* 1, (2010), <http://dx.doi.org/10.1364/boe.1.000553>.
- [105] A., K., M., K., S., F., R., W., J., L., and A., Y., "Validation of a non-invasive regional cerebral blood flow monitor," *J. Neurosurg. Anesthesiol.* 21, (2009).
- [106] Durduran, T. and Yodh, A. G., "Diffuse correlation spectroscopy for non-invasive, micro-vascular cerebral blood flow measurement," *Neuroimage* 85, (2014), <http://dx.doi.org/10.1016/j.neuroimage.2013.06.017>.
- [107] Buckley, E. M., Parthasarathy, A. B., Grant, P. E., Yodh, A. G., and Franceschini, M. A., "Diffuse correlation spectroscopy for measurement of cerebral blood flow: future prospects," *Neurophotonics* 1, 011009 (2014), <http://dx.doi.org/10.1117/1.nph.1.1.011009>.
- [108] Cheung, C., Culver, J. P., Takahashi, K., Greenberg, J. H., and Yodh, A. G., "In vivo cerebrovascular measurement combining diffuse near-infrared absorption and correlation spectroscopies," *Phys. Med. Biol.* 46, (2001), <http://dx.doi.org/10.1088/0031-9155/46/8/302>.
- [109] Zhou, C., Eucker, S. A., Durduran, T., Yu, G., Ralston, J., Friess, S. H., Ichord, R. N., Margulies, S. S., and Yodh, A. G., "Diffuse optical monitoring of hemodynamic changes in piglet brain with closed head injury," *J. Biomed. Opt.* 14, (2009), <http://dx.doi.org/10.1117/1.3146814>.
- [110] Durduran, T., Zhou, C., Edlow, B. L., Yu, G., Choe, R., Kim, M. N., Cucchiara, B. L., Putt, M. E., Shah, Q., Kasner, S. E., Greenberg, J. H., Yodh, A. G., and Detre, J. A., "Transcranial optical monitoring of cerebrovascular hemodynamics in acute stroke patients," *Opt. Express* 17, (2009), <http://dx.doi.org/10.1364/oe.17.003884>.
- [111] Busch, D. R., Rusin, C. G., Miller-Hance, W., Kibler, K., Baker, W. B., Heinle, J. S., Fraser, C. D., Yodh, A. G., Licht, D. J., and Brady, K. M., "Continuous cerebral hemodynamic measurement during deep hypothermic circulatory arrest," *Biomed. Opt. Express* 7, (2016), <http://dx.doi.org/10.1364/boe.7.003461>.
- [112] Li, T., Lin, Y., Shang, Y., He, L., Huang, C., Szabunio, M., and Yu, G., "Simultaneous measurement of deep tissue blood flow and oxygenation

Bibliography

- using noncontact diffuse correlation spectroscopy flow-oximeter," *Sci. Rep.* 3, 1–10 (2013), <http://dx.doi.org/10.1038/srep01358>.
- [113] Shang, Y., Zhao, Y. Q., Cheng, R., Dong, L. X., Irwin, D., and Yu, G. Q., "Portable optical tissue flow oximeter based on diffuse correlation spectroscopy," *Opt. Lett.* (2009), <http://dx.doi.org/10.1364/ol.34.003556>.
- [114] Cheng, R., Zhang, X., Daugherty, A., Shin, H., and Yu, G., "Noninvasive quantification of postocclusive reactive hyperemia in mouse thigh muscle by near-infrared diffuse correlation spectroscopy," *Appl. Opt.* 52, (2013), <http://dx.doi.org/10.1364/AO.52.007324>.
- [115] Quaresima, V., Farzam, P., Anderson, P., Farzam, P. Y., Wiese, D., Carp, S. A., Ferrari, M., and Franceschini, M. A., "Diffuse correlation spectroscopy and frequency-domain near-infrared spectroscopy for measuring microvascular blood flow in dynamically exercising human muscles," *J. Appl. Physiol.* 127, (2019), <http://dx.doi.org/10.1152/jappphysiol.00324.2019>.
- [116] Grosenick, D., Rinneberg, H., Cubeddu, R., and Taroni, P., "Review of optical breast imaging and spectroscopy," *J. Biomed. Opt.* 21, (2016), <http://dx.doi.org/10.1117/1.JBO.21.9.091311>.
- [117] Zhou, C., Choe, R., Shah, N., Durduran, T., Yu, G., Durkin, A., Hsiang, D., Mehta, R., Butler, J., Cerussi, A., Tromberg, B. J., and Yodh, A. G., "Diffuse optical monitoring of blood flow and oxygenation in human breast cancer during early stages of neoadjuvant chemotherapy," *J. Biomed. Opt.* 12, (2007), <http://dx.doi.org/10.1117/1.2798595>.
- [118] Yu, G., Durduran, T., Zhou, C., Zhu, T. C., Finlay, J. C., Busch, T. M., Malkowicz, S. B., Hahn, S. M., and Yodh, A. G., "Real-time In Situ Monitoring of Human Prostate Photodynamic Therapy with Diffuse Light," *Photochem. Photobiol.* 82, (2006), <http://dx.doi.org/10.1562/2005-10-19-ra-721>.
- [119] Wang, H. W., Putt, M. E., Emanuele, M. J., Shin, D. B., Glatstein, E., Yodh, A. G., and Busch, T. M., "Treatment-induced changes in tumor oxygenation predict photodynamic therapy outcome," *Cancer Res.* 64, (2004), <http://dx.doi.org/10.1158/0008-5472.CAN-03-3632>.
- [120] Van Rossum, M. C. W. and Nieuwenhuizen, T. M., "Multiple scattering of classical waves: Microscopy, mesoscopy, and diffusion," *Rev. Mod. Phys.* 71, (1999), <http://dx.doi.org/10.1103/revmodphys.71.313>.
- [121] Kim, A. D., "Transport theory for light propagation in biological tissue," *J.*

Bibliography

- Opt. Soc. Am. A* 21, (2004), <http://dx.doi.org/10.1364/josaa.21.000820>.
- [122] Patterson, M. S., Wilson, B. C., and Wyman, D. R., "The propagation of optical radiation in tissue I. Models of radiation transport and their application," *Lasers Med. Sci.* 6, (1991), <http://dx.doi.org/10.1007/BF02032543>.
- [123] Fleck, J. A. and Cummings, J. D., "An implicit Monte Carlo scheme for calculating time and frequency dependent nonlinear radiation transport," *J. Comput. Phys.* 8, (1971), [http://dx.doi.org/10.1016/0021-9991\(71\)90015-5](http://dx.doi.org/10.1016/0021-9991(71)90015-5).
- [124] Jacques, S. L. and Pogue, B. W., "Tutorial on diffuse light transport," *J. Biomed. Opt.* (2008), <http://dx.doi.org/10.1117/1.2967535>.
- [125] Hielscher, A. H., Jacques, S. L., Wang, L., and Tittel, F. K., "The influence of boundary conditions on the accuracy of diffusion theory in time-resolved reflectance spectroscopy of biological tissues," *Phys. Med. Biol.* 40, 1957–1975 (1995), <http://dx.doi.org/10.1088/0031-9155/40/11/013>.
- [126] Torricelli, A., Pifferi, A., Spinelli, L., Cubeddu, R., Martelli, F., Del Bianco, S., and Zaccanti, G., "Time-resolved reflectance at null source-detector separation: Improving contrast and resolution in diffuse optical imaging," *Phys. Rev. Lett.* 95, 2–5 (2005), <http://dx.doi.org/10.1103/PhysRevLett.95.078101>.
- [127] Pearce, J., Jian, Z., Mittleman, D. M., Planken, P., and Unterrainer, K., "Propagation of terahertz pulses in random media," *Philos. Trans. R. Soc. A Math. Phys. Eng. Sci.* (2004), <http://dx.doi.org/10.1098/rsta.2003.1324>.
- [128] Tomita, M. and Matsuoka, M., "Temporal fluctuations in disordered static optical media," *Phys. Rev. B* (1991), <http://dx.doi.org/10.1103/PhysRevB.43.13579>.
- [129] Tal, E. and Silberberg, Y., "Transformation from an ultrashort pulse to a spatiotemporal speckle by a thin scattering surface," *Opt. Lett.* 31, 3529 (2006), <http://dx.doi.org/10.1364/ol.31.003529>.
- [130] Goodman, J. W., "Some fundamental properties of speckle*," *J. Opt. Soc. Am.* (1976), <http://dx.doi.org/10.1364/josa.66.001145>.
- [131] Dainty, J. C., "The statistics of speckle patterns," *Prog. Opt.* 14, (1977), [http://dx.doi.org/10.1016/S0079-6638\(08\)70249-X](http://dx.doi.org/10.1016/S0079-6638(08)70249-X).
- [132] Tsai, B.-M. and Gardner, C. S., "Time-resolved speckle effects on the

Bibliography

- estimation of laser-pulse arrival times," *J. Opt. Soc. Am. A* 2, 649 (1985), <http://dx.doi.org/10.1364/josaa.2.000649>.
- [133] Colombo, L., Samaei, S., Lanka, P., Ancora, D., Pagliazzi, M., Durduran, T., Sawosz, P., Liebert, A., and Pifferi, A., "Coherent fluctuations in time-domain diffuse optics," *APL Photonics* 5, (2020), <http://dx.doi.org/10.1063/5.0011838>.
- [134] Carpenter, D. K., "Dynamic Light Scattering with Applications to Chemistry, Biology, and Physics (Berne, Bruce J.; Pecora, Robert)," *J. Chem. Educ.* 54, (1977), <http://dx.doi.org/10.1021/ed054pa430.1>.
- [135] Bhattacharjee, S., "DLS and zeta potential - What they are and what they are not?," *J. Control. Release* 235, (2016), <http://dx.doi.org/10.1016/j.jconrel.2016.06.017>.
- [136] Stetefeld, J., McKenna, S. A., and Patel, T. R., "Dynamic light scattering: a practical guide and applications in biomedical sciences," *Biophys. Rev.* 8, (2016), <http://dx.doi.org/10.1007/s12551-016-0218-6>.
- [137] Mandel, L. and Wolf, E., "Coherence properties of optical fields," *Rev. Mod. Phys.* 37, (1965), <http://dx.doi.org/10.1103/RevModPhys.37.231>.
- [138] Lemieux, P.-A. and Durian, D. J., "Investigating non-Gaussian scattering processes by using nth-order intensity correlation functions," *J. Opt. Soc. Am. A* 16, 1651–1664 (1999), <http://dx.doi.org/10.1364/josaa.16.001651>.
- [139] Maret, G. and Wolf, P. E., "Multiple light scattering from disordered media. The effect of brownian motion of scatterers," *Zeitschrift für Phys. B Condens. Matter* 65, 409–413 (1987), <http://dx.doi.org/10.1007/BF01303762>.
- [140] Pine, D. J., Weitz, D. A., Chaikin, P. M., and Herbolzheimer, E., "Diffusing wave spectroscopy," *Phys. Rev. Lett.* (1988), <http://dx.doi.org/10.1103/PhysRevLett.60.1134>.
- [141] Zhou, C., "In-vivo optical imaging and spectroscopy of cerebral hemodynamics," .
- [142] Boas, D. A. and Yodh, A. G., "Spatially varying dynamical properties of turbid media probed with diffusing temporal light correlation," *J. Opt. Soc. Am. A* 14, 192 (1997), <http://dx.doi.org/10.1364/JOSAA.14.000192>.
- [143] Ackerson, B. J., Dougherty, R. L., Reguigui, N. M., and Nobbmann, U.,

Bibliography

- "Correlation transfer: Application of radiative transfer solution methods to photon correlation problems," in *Journal of Thermophysics and Heat Transfer* (1992), Vol. 6, <http://dx.doi.org/10.2514/3.11537>.
- [144] Colombo, L., Pagliuzzi, M., Sekar, S. K. V., Contini, D., Mora, A. D., Spinelli, L., Torricelli, A., Durduran, T., and Pifferi, A., "Effects of the instrument response function and the gate width in time-domain diffuse correlation spectroscopy: model and validations," *Neurophotonics* 6, 1 (2019), <http://dx.doi.org/10.1117/1.NPh.6.3.035001>.
- [145] Samaei, S., Borycki, D., Kacprzak, M., Sawosz, P., and Liebert, A., "Time-domain diffuse correlation spectroscopy quantifies path-length-resolved dynamical properties of a layered turbid media," *Opt. InfoBase Conf. Pap. Part F142-*, 10–13 (2019), <http://dx.doi.org/10.1117/12.2527160>.
- [146] Contini, D., Dalla Mora, A., Spinelli, L., Farina, A., Torricelli, A., Cubeddu, R., Martelli, F., Zaccanti, G., Tosi, A., Boso, G., Zappa, F., and Pifferi, A., "Effects of time-gated detection in diffuse optical imaging at short source-detector separation," *J. Phys. D. Appl. Phys.* 48, 045401 (2015), <http://dx.doi.org/10.1088/0022-3727/48/4/045401>.
- [147] Svelto, O., *Principles of Lasers* (2010).
- [148] Kues, M., Reimer, C., Wetzel, B., Roztock, P., Little, B. E., Chu, S. T., Hansson, T., Viktorov, E. A., Moss, D. J., and Morandotti, R., "Passively mode-locked laser with an ultra-narrow spectral width," *Nat. Photonics* 11, 159–162 (2017), <http://dx.doi.org/10.1038/nphoton.2016.271>.
- [149] Pontecorvo, E., Ferrante, C., Elles, C. G., and Scopigno, T., "Spectrally tailored narrowband pulses for femtosecond stimulated Raman spectroscopy in the range 330–750 nm," *Opt. Express* 21, (2013), <http://dx.doi.org/10.1364/oe.21.006866>.
- [150] Malinowski, A., Vu, K. T., Chen, K. K., Nilsson, J., Jeong, Y., Alam, S., Lin, D., and Richardson, D. J., "High power pulsed fiber MOPA system incorporating electro-optic modulator based adaptive pulse shaping," *Opt. Express* 17, (2009), <http://dx.doi.org/10.1364/oe.17.020927>.
- [151] Yanhai Wang, 王艳海, Jiangfeng Wang, 王江峰, You'en Jiang, 姜有恩, Yan Bao, 鲍岩, Xuechun Li, 李学春, and Zunqi Lin, 林尊琪, "Laser pulse spectral shaping based on electro-optic modulation," *Chinese Opt. Lett.* 6, (2008), <http://dx.doi.org/10.3788/col20080611.0841>.

Bibliography

- [152] Pifferi, A., "TiSapphire mode-locked laser development and characterization," (1991).
- [153] Pifferi, A., Torricelli, A., Taroni, P., Comelli, D., Bassi, A., and Cubeddu, R., "Fully automated time domain spectrometer for the absorption and scattering characterization of diffusive media," *Rev. Sci. Instrum.* **78**, (2007), <http://dx.doi.org/10.1063/1.2735567>.
- [154] Konugolu Venkata Sekar, S., Dalla Mora, A., Bargigia, I., Martinenghi, E., Lindner, C., Farzam, P., Pagliazzi, M., Durduran, T., Taroni, P., Pifferi, A., and Farina, A., "Broadband (600-1350 nm) Time-Resolved Diffuse Optical Spectrometer for Clinical Use," *IEEE J. Sel. Top. Quantum Electron.* **22**, 406–414 (2016), <http://dx.doi.org/10.1109/JSTQE.2015.2506613>.
- [155] Natarajan, C. M., Tanner, M. G., and Hadfield, R. H., "Superconducting nanowire single-photon detectors: physics and applications," *Supercond. Sci. Technol.* **25**, 063001 (2012), <http://dx.doi.org/10.1088/0953-2048/25/6/063001>.
- [156] Korzh, B., Zhao, Q. Y., Allmaras, J. P., Frasca, S., Autry, T. M., Bersin, E. A., Beyer, A. D., Briggs, R. M., Bumble, B., Colangelo, M., Crouch, G. M., Dane, A. E., Gerrits, T., Lita, A. E., Marsili, F., Moody, G., Peña, C., Ramirez, E., Rezac, J. D., Sinclair, N., Stevens, M. J., Velasco, A. E., Verma, V. B., Wollman, E. E., Xie, S., Zhu, D., Hale, P. D., Spiropulu, M., Silverman, K. L., Mirin, R. P., Nam, S. W., Kozorezov, A. G., Shaw, M. D., and Berggren, K. K., "Demonstration of sub-3 ps temporal resolution with a superconducting nanowire single-photon detector," *Nat. Photonics* **14**, (2020), <http://dx.doi.org/10.1038/s41566-020-0589-x>.
- [157] Pagliazzi, M., "optical methods for path length flow," (2019).
- [158] Wahl, M., Gregor, I., Patting, M., and Enderlein, J., "Fast calculation of fluorescence correlation data with asynchronous time-correlated single-photon counting," *Opt. Express* **11**, (2003), <http://dx.doi.org/10.1364/oe.11.003583>.
- [159] Magatti, D. and Ferri, F., "Fast multi-tau real-time software correlator for dynamic light scattering," *Appl. Opt.* (2001), <http://dx.doi.org/10.1364/ao.40.004011>.
- [160] Waithe, D., Clausen, M. P., Sezgin, E., and Eggeling, C., "FoCuS-point: software for STED fluorescence correlation and time-gated single photon counting," *Bioinformatics* **32**, 958–960 (2016),

- <http://dx.doi.org/10.1093/bioinformatics/btv687>.
- [161] Cortese, L., Presti, G. Lo, Pagliuzzi, M., Contini, D., Mora, A. D., Pifferi, A., Sekar, S. K. V., Spinelli, L., Taroni, P., Zanoletti, M., Weigel, U. M., de Fraguier, S., Nguyen-Dihn, A., Rosinski, B., Durduran, T., Lo Presti, G., Pagliuzzi, M., Contini, D., Mora, A. D., Pifferi, A., Konugolu Venkata Sekar, S., Spinelli, L., Taroni, P., Zanoletti, M., Weigel, U. M., de Fraguier, S., Nguyen-Dihn, A., Rosinski, B., and Durduran, T., "Liquid phantoms for near-infrared and diffuse correlation spectroscopies with tunable optical and dynamic properties," *Biomed. Opt. Express* 9, 2068 (2018), <http://dx.doi.org/10.1364/boe.9.002068>.
- [162] Tomita, M. and Ikari, H., "Influence of finite coherence length of incoming light on enhanced backscattering," *Phys. Rev. B* (1991), <http://dx.doi.org/10.1103/PhysRevB.43.3716>.
- [163] Qiu, L., Cheng, H., Torricelli, A., and Li, J., "Using a simulation approach to optimize time-domain diffuse correlation spectroscopy measurement on human head," *Neurophotonics* 5, 1 (2018), <http://dx.doi.org/10.1117/1.nph.5.2.025007>.
- [164] Mazumder, D., Wu, M. M., Ozana, N., Tamborini, D., Franceschini, M. A., and Carp, S. A., "Optimization of time domain diffuse correlation spectroscopy parameters for measuring brain blood flow," *Neurophotonics* 8, (2021), <http://dx.doi.org/10.1117/1.nph.8.3.035005>.
- [165] Qiu, L., Zhang, T., Huang, W., Sun, W., Wu, X., Sun, H., Lin, F., and Li, J., "Time Domain Diffuse Correlation Spectroscopy for Detecting Human Brain Function: Optimize System on Real Experimental Conditions by Simulation Method," *IEEE Photonics J.* 13, (2021), <http://dx.doi.org/10.1109/JPHOT.2021.3089635>.
- [166] Samaei, S., Colombo, L., Borycki, D., Pagliuzzi, M., Durduran, T., Sawosz, P., Wojtkiewicz, S., Contini, D., Torricelli, A., Pifferi, A., and Liebert, A., "Performance assessment of laser sources for time-domain diffuse correlation spectroscopy," *Biomed. Opt. Express* 12, (2021), <http://dx.doi.org/10.1364/boe.432363>.
- [167] Akcay, C., Parrein, P., and Rolland, J. P., "Estimation of longitudinal resolution in optical coherence imaging," *Appl. Opt.* 41, (2002), <http://dx.doi.org/10.1364/ao.41.005256>.
- [168] Enderlein, J. and Gregor, I., "Using fluorescence lifetime for discriminating

- detector afterpulsing in fluorescence-correlation spectroscopy," *Rev. Sci. Instrum.* **76**, (2005), <http://dx.doi.org/10.1063/1.1863399>.
- [169] Carp, S. A., Tamborini, D., Mazumder, D., Wu, K.-C. (Tony), Robinson, M. R., Stephens, K. A., Shatrovov, O., Lue, N., Ozana, N., Blackwell, M. H., and Franceschini, M. A., "Diffuse correlation spectroscopy measurements of blood flow using 1064 nm light," *J. Biomed. Opt.* **25**, 97003–97004 (2020), <http://dx.doi.org/10.1117/1.JBO.25.9.097003>.
- [170] Colombo, L., Pagliazzi, M., Konugolu Venkata Sekar, S., Contini, D., Durduran, T., and Pifferi, A., "In vivo time-domain diffuse correlation spectroscopy above the water absorption peak," *Opt. Lett.* (2020), <http://dx.doi.org/10.1364/ol.392355>.
- [171] Fang, Q. and Boas, D. A., "Monte Carlo Simulation of Photon Migration in 3D Turbid Media Accelerated by Graphics Processing Units," *Opt. Express* **17**, (2009), <http://dx.doi.org/10.1364/oe.17.020178>.
- [172] Pifferi, A., Torricelli, A., Bassi, A., Taroni, P., Cubeddu, R., Wabnitz, H., Grosenick, D., Möller, M., Macdonald, R., Swartling, J., Svensson, T., Andersson-Engels, S., Van Veen, R. L. P., Sterenborg, H. J. C. M., Tualle, J. M., Nghiem, H. L., Avrillier, S., Whelan, M., and Stamm, H., "Performance assessment of photon migration instruments: The MEDPHOT protocol," *Appl. Opt.* **44**, 2104–2114 (2005), <http://dx.doi.org/10.1364/AO.44.002104>.
- [173] Snieder, R., Grêt, A., Douma, H., and Scales, J., "Coda wave interferometry for estimating nonlinear behavior in seismic velocity," *Science* (**80-**). (2002), <http://dx.doi.org/10.1126/science.1070015>.
- [174] Larose, E., Margerin, L., Van Tiggelen, B. A., and Campillo, M., "Weak localization of seismic waves," *Phys. Rev. Lett.* (2004), <http://dx.doi.org/10.1103/PhysRevLett.93.048501>.
- [175] Pacheco, C. and Snieder, R., "Time-lapse travel time change of multiply scattered acoustic waves," *J. Acoust. Soc. Am.* (2005), <http://dx.doi.org/10.1121/1.2000827>.
- [176] Aubry, J.-F., Tanter, M., Gerber, J., Thomas, J.-L., and Fink, M., "Optimal focusing by spatio-temporal inverse filter. II. Experiments. Application to focusing through absorbing and reverberating media," *J. Acoust. Soc. Am.* (2001), <http://dx.doi.org/10.1121/1.1377052>.
- [177] Cowan, M. L., Jones, I. P., Page, J. H., and Weitz, D. A., "Diffusing acoustic

Bibliography

- wave spectroscopy," *Phys. Rev. E - Stat. Physics, Plasmas, Fluids, Relat. Interdiscip. Top.* (2002), <http://dx.doi.org/10.1103/PhysRevE.65.066605>.
- [178] Langbein, W., Hvam, J. M., and Zimmermann, R., "Time-resolved speckle analysis: A new approach to coherence and dephasing of optical excitations in solids," *Phys. Rev. Lett.* (1999), <http://dx.doi.org/10.1103/PhysRevLett.82.1040>.
- [179] Jian, Z., Pearce, J., and Mittleman, D. M., "Characterizing Individual Scattering Events by Measuring the Amplitude and Phase of the Electric Field Diffusing through a Random Medium," *Phys. Rev. Lett.* (2003), <http://dx.doi.org/10.1103/PhysRevLett.91.033903>.
- [180] Gardner, C. S., "Target signatures for laser altimeters: an analysis," *Appl. Opt.* 21, 448 (1982), <http://dx.doi.org/10.1364/ao.21.000448>.
- [181] Tsai, B. and Gardner, C. S., "Remote sensing of sea state by laser altimeters.," (1981).
- [182] Webster, M. A., Gerke, T. D., Weiner, A. M., and Webb, K. J., "Spectral and temporal speckle field measurements of a random medium," *Opt. Lett.* (2004), <http://dx.doi.org/10.1364/ol.29.001491>.
- [183] Katz, O., Small, E., Bromberg, Y., and Silberberg, Y., "Focusing and compression of ultrashort pulses through scattering media," *Nat. Photonics* 5, (2011), <http://dx.doi.org/10.1038/nphoton.2011.72>.
- [184] Aulbach, J., Gjonaj, B., Johnson, P. M., Mosk, A. P., and Lagendijk, A., "Control of light transmission through opaque scattering media in space and time," *Phys. Rev. Lett.* 106, (2011), <http://dx.doi.org/10.1103/PhysRevLett.106.103901>.
- [185] McCabe, D. J., Tajalli, A., Austin, D. R., Bondareff, P., Walmsley, I. A., Gigan, S., and Chatel, B., "Spatio-temporal focusing of an ultrafast pulse through a multiply scattering medium," *Nat. Commun.* 2, (2011), <http://dx.doi.org/10.1038/ncomms1434>.
- [186] Tajalli, A., McCabe, D. J., Austin, D. R., Walmsley, I. A., and Chatel, B., "Characterization of the femtosecond speckle field of a multiply scattering medium via spatio-spectral interferometry," *J. Opt. Soc. Am. B* (2012), <http://dx.doi.org/10.1364/josab.29.001146>.
- [187] Bi, R., Dong, J., and Lee, K., "Multi-channel deep tissue flowmetry based on

Bibliography

temporal diffuse speckle contrast analysis," *Opt. Express* 21, 22854 (2013),
<http://dx.doi.org/10.1364/oe.21.022854>.